

Characterizing Batteries by In Situ Electrochemical Atomic Force Microscopy: A Critical Review

Zhenyu Zhang, Samia Said, Keenan Smith, Rhodri Jervis, Christopher A. Howard, Paul R. Shearing, Dan J. L. Brett,* and Thomas S. Miller*

Although lithium, and other alkali ion, batteries are widely utilized and studied, many of the chemical and mechanical processes that underpin the materials within, and drive their degradation/failure, are not fully understood. Hence, to enhance the understanding of these processes various *ex situ*, *in situ* and *operando* characterization methods are being explored. Recently, electrochemical atomic force microscopy (EC-AFM), and related techniques, have emerged as crucial platforms for the versatile characterization of battery material surfaces. They have revealed insights into the morphological, mechanical, chemical, and physical properties of battery materials when they evolve under electrochemical control. This critical review will appraise the progress made in the understanding batteries using EC-AFM, covering both traditional and new electrode–electrolyte material junctions. This progress will be juxtaposed against the ability, or inability, of the system adopted to embody a truly representative battery environment. By contrasting key EC-AFM literature with conclusions drawn from alternative characterization tools, the unique power of EC-AFM to elucidate processes at battery interfaces is highlighted. Simultaneously opportunities for complementing EC-AFM data with a range of spectroscopic, microscopic, and diffraction techniques to overcome its limitations are described, thus facilitating improved battery performance.

Numerous important processes occur at/through the solid/liquid interface of battery electrodes and hence understanding processes at these interfaces is pivotal when looking to improve the performance of LIBs or related alkali ion batteries.^[3] For example, the chemical, morphological, and mechanical properties of the solid–electrolyte interphase (SEI) at the graphite anode are key factors in defining LIB efficiency.^[4–6] Similarly, particle expansion, strain evolution, film cracking, dendrite growth, phase transitions, and changes in the ionic/electronic properties of electrode materials all have important interfacial components that can all be probed during electrochemical processes.^[7]

Enormous efforts by the battery research community have been put into the study of these issues, with *in situ/operando* spectroscopic, microscopic and diffraction characterization methods proving to be vital for the investigation of the operation, degradation, and failure of batteries.^[8,9] Diffraction


1. Introduction

With the advantages of high energy density and long cycle life, Li ion batteries (LIBs) have become one of the most widely investigated and most successfully commercialized electrochemical energy storage system of modern times, with applications in electronic devices, electric vehicles, and beyond.^[1] However, an ever-increasing demand for higher energy and power densities, higher charging rates, higher Coulombic efficiencies, longer cycle life, and better safety are driving the need for a greater understanding of battery materials on the microscopic-to-atomistic scale.^[2]

and spectroscopic techniques, including *in situ* X-ray diffraction (XRD),^[10] *in situ* Raman spectroscopy, and Fourier-transform infrared spectroscopy (FTIR), have been used to study interfacial layers;^[11] whereas the morphology and structure of electrode materials have been studied via microscopy techniques such as *in situ* scanning electron microscopy (SEM),^[12] *in situ* transmission electron microscopy (TEM),^[13] and *operando* X-ray computed tomography (X-ray CT).^[14]

Similarly, atomic force microscopy (AFM) and other advanced scanning probe microscopy (SPM) techniques are becoming crucial platforms for the study of batteries, enabling

Z. Zhang, S. Said, K. Smith, R. Jervis, P. R. Shearing, D. J. L. Brett, T. S. Miller
Electrochemical Innovation Lab
Department of Chemical Engineering
University College London
Torrington Place, London WC1E 7JE, UK
E-mail: d.brett@ucl.ac.uk; t.miller@ucl.ac.uk

 The ORCID identification number(s) for the author(s) of this article can be found under <https://doi.org/10.1002/aenm.202101518>.

© 2021 The Authors. Advanced Energy Materials published by Wiley-VCH GmbH. This is an open access article under the terms of the Creative Commons Attribution License, which permits use, distribution and reproduction in any medium, provided the original work is properly cited.

DOI: 10.1002/aenm.202101518

Z. Zhang, R. Jervis, P. R. Shearing, D. J. L. Brett, T. S. Miller
The Faraday Institution
Quad One
Becquerel Avenue
Harwell Campus, Didcot OX11 0RA, UK
C. A. Howard
Department of Physics and Astronomy
University College London
Gower Street, London WC1E 6BT, UK

the versatile characterization of the morphological, mechanical, local-electrochemical, and other physical properties of battery materials as they undergo charge and discharge processes.^[15,16] This allows for the investigation of nanoscale processes at the electrode–electrolyte interface.^[17–19]

Unfortunately, the choice of nonrepresentative electrode architectures, overly idealized electrode materials and unrealistic electrochemical cell designs often raise questions regarding the degree to which in situ/operando findings can be relied upon for understanding commercially-relevant (i.e., realistic) battery systems.^[20] This is particularly the case for SPM studies as they usually rely on flat homogeneous substrates for imaging. To date, reviews detailing AFM^[21,22] and SPM^[23–25] approaches in battery research have not fully considered the degree to which the limitations of the systems being studied impact our ability to translate the findings onto our understanding of real batteries.^[26]

This critical review will appraise progress in the study of LIB (and other relevant alkali-ion) interfaces via electrochemical AFM (EC-AFM) and select alternative SPM techniques, covering both traditional and new electrode–electrolyte material interfaces. This progress will be contrasted against that made in the use of other tools for battery characterization, comparing the information the different techniques can provide as well as their relative ability to represent practical batteries.

2. Technical Background: EC-AFM and LIBs

2.1. Working Principles of EC-AFM

In contrast to microscopies that produce images by the interaction of light or electron beams with a sample, SPM techniques harness local physical and electromagnetic interactions taking place between a probe with a sharp tip and the surface of a specimen, providing nanoscale, or below, resolution imaging.^[27,28]

In its most common form, AFM provides topographical information about a sample by measuring the displacement of a laser reflected from the back of cantilever attached to the probe, which is moved across the sample surface, as shown in **Figure 1a**.^[29] The process can operate in contact, noncontact and intermittent contact (tapping) modes, providing high-resolution surface topography data (typically \approx 1–20 nm lateral and $<$ 0.025 nm height resolution), alongside a diverse range of information on compositional properties, including stiffness, elasticity, adhesion, magnetic and electrostatic fields, spreading resistance, and conductivity, under the appropriate experimental setup.^[30] Importantly, this can be achieved for a large variety of materials (metals, insulators, organic, inorganic, biological) in many different environments (atmospheric, liquid, thermal).^[31] This is key for the in situ study of LIBs, as a solid sample must be evaluated in a liquid electrolyte^[32] and, due to the air sensitivity of most electrode/electrolyte materials, these studies must often be conducted in an inert environment.^[33,34]

To avoid confusion it is necessary to explicitly define the difference between ex situ, in situ and in operando AFM characterization methods at this point. Ex situ experiments are those where the material characterization (i.e., AFM image capture) and electrochemical measurements (e.g., cyclic voltammetry) are

conducted separately, with the sample commonly being moved between experimental environments (e.g., moving an electrode from a coin cell to the AFM). These measurements can therefore often replicate the electrochemical environment of a battery well, but suffer from many disadvantages associated with sample damage, degradation and inconsistent measurement location. They also only provide ‘snapshots’ of electrode processes, meaning subtleties can be missed. There is a more subtle difference between in situ and operando EC-AFM techniques. In situ EC-AFM entails the imaging of the sample within the electrochemical cell (i.e., within the ‘battery’), but it does not explicitly need to be under electrochemical control, for example, imaging an electrode in liquid electrolyte, but only before and after charge/discharge. This is common in the study of battery materials as AFM imaging is often slow, meaning imaging is undertaken while potential control is ‘paused’ to avoid missing fast-changing reactions. However, this can still result in phenomena being missed. In contrast operando EC-AFM involves the simultaneous imaging and electrochemical measurement, revealing details in real time and providing directly correlated electrochemical and morphological data.^[35]

In an in situ or operando EC-AFM experiment the AFM scan head is usually placed inside a glovebox filled with Ar gas, to isolate the battery materials from the oxygen and moisture in ambient air. Furthermore, the sample under evaluation must be electrically connected to allow a potential to be applied and coupled with a reference and counter electrode (or single counter-reference), forming the electrochemical cell that is the key defining feature of EC-AFM (**Figure 1b**).^[36] As the AFM probe is usually submerged in the liquid electrolyte within an open cell while scanning (with a cover surround to prevent electrolyte evaporation), the laser must be focused onto the cantilever via an optical window, meaning angle compensation must be applied to mitigate refraction between the gas/solid/liquid interfaces. For all-solid-state batteries no liquid cell is needed but the scanning probe is configured to image a cross-section of the battery, or the electrode (electrolyte free) or electrolyte surface.^[23] In these forms, a battery electrode can be cycled in a galvanostatic or potentiostatic manner, for example, enabling the evolution and degradation of anodes, cathodes and other relevant interfaces to be studied as a function of time, applied voltage and current.

Although similar in principle to EC-AFM, conductive AFM (C-AFM) utilizes a probe with highly wear-resistant electrically conductive coating, to simultaneously provide topographic imaging and measurement of the conductivity in contact mode (**Figure 1c**). A typical current resolution is \approx 10 pA.^[37,38] Current–voltage (I – V) spectroscopy allows the recording of the bias dependent resistivity by ramping the voltage bias over a sample location of interest, even in a liquid environment under some experimental conditions. However, liquid imaging is significantly less common than with EC-AFM. Nonetheless, C-AFM can be applied to perform advanced in situ measurements, for instance, localized AFM-based impedance spectroscopy under controlled environments.^[39] Closely related techniques have utilized various input/detection arrangements to provide high-resolution contrast in the electronic properties (resistivity mapping) of electrode components which, for example, can enable different materials to be distinguished.^[40]

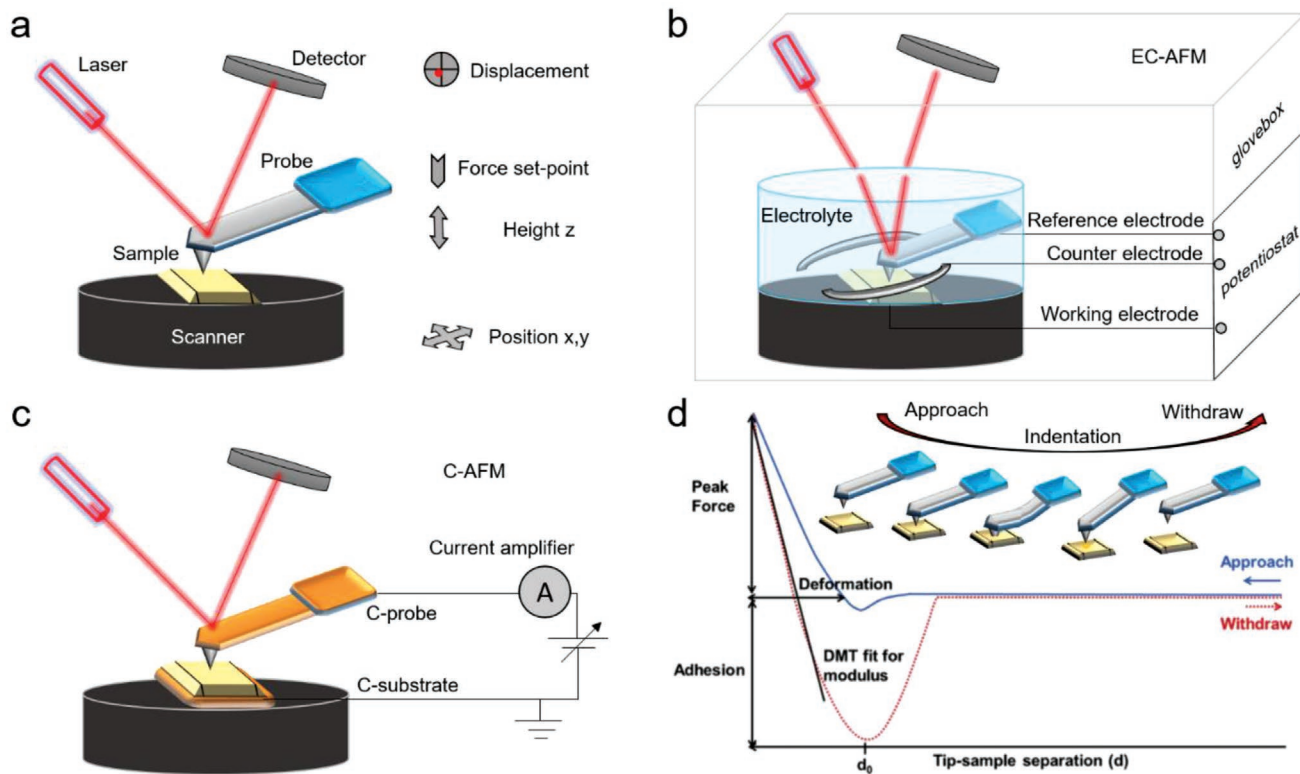


Figure 1. Schematic of a) AFM, b) EC-AFM, c) C-AFM. d) Schematic diagram of a force versus separation curve in the PeakForce tapping mode. Reproduced with permission.^[42] Copyright 2015, Elsevier.

AFM also provides the opportunity to evaluate the mechanical properties of a sample.^[41–43] The deflection of the cantilever as it approaches, interacts with and retracts from the surface is a direct manifestation of the interaction force (both attractive and repulsive), producing force–distance curves. As shown in Figure 1d, this force curve provides access to several key micro-mechanical parameters: maximum indentation (the indentation depth depends on the stiffness of the probed area when a constant force is applied), adhesion between the cantilever and the sample, and elastic/plastic deformation energy. The Young’s modulus can also be extracted by fitting the retraction curves. For a sample with hard surface, the retracting force–distance curve usually overlaps with the approaching curve, as the most significant force is repulsive contact (indentation) between tip and sample. However, for most cases that involve solid–liquid interfaces, the adhesion force between the tip and sample surface during the retracting becomes more significant. Hence, the retracting curve is selected for Young’s modulus calculations, to ensure the adhesion force between the tip and sample is considered. Generally, the reduced modulus E^* is obtained by fitting the retraction curve to the Derjaguin–Muller–Toporov (DMT) model:

$$F - F_{\text{adh}} = \frac{4}{3} E^* \sqrt{R(d - d_0)^3} \quad (1)$$

where $F - F_{\text{adh}}$ is the force on the cantilever relative to the adhesion force, R is the tip end radius, and $(d - d_0)$ is the deformation of the sample. When the Poisson’s ratio is known, sample Young’s modulus E_s can be related to E^* by the equation:

$$E^* = \left[\frac{1 - \nu_s^2}{E_s} + \frac{1 - \nu_{\text{tip}}^2}{E_{\text{tip}}} \right]^{-1} \quad (2)$$

assuming that the tip modulus (E_{tip}) is infinite; where ν_{tip} is the tip Poisson ratio and ν_s the sample Poisson ratio. This model is suitable for testing materials with moduli in the range of ≈ 700 kPa to ≈ 70 GPa (which includes most battery electrode materials and interfacial species formed), provided an appropriate probe is selected and calibrated.^[42]

If force curves are performed at every point across a surface, as is the case with ‘peak force’ imaging modes, real-time mechanical maps can be simultaneously gathered alongside topographical data. When combined with EC-AFM, this allows both changes in topography and mechanical properties to be visualized with relation to the applied potential. This capability is particularly important for battery electrodes as it can provide extensive interfacial understanding, allowing examination of important process such as the evolution of the SEI, an area where there is still significant debate within the battery research community.^[44]

2.2. LIBs: Structures and Materials

Since their development in the 1980s, LIBs have become the preeminent portable energy storage technology and they have revolutionized modern life. In recognition of this, the 2019 Nobel Prize in Chemistry was awarded to John B. Goodenough, M. Stanley Whittingham and Akira Yoshino.^[45]

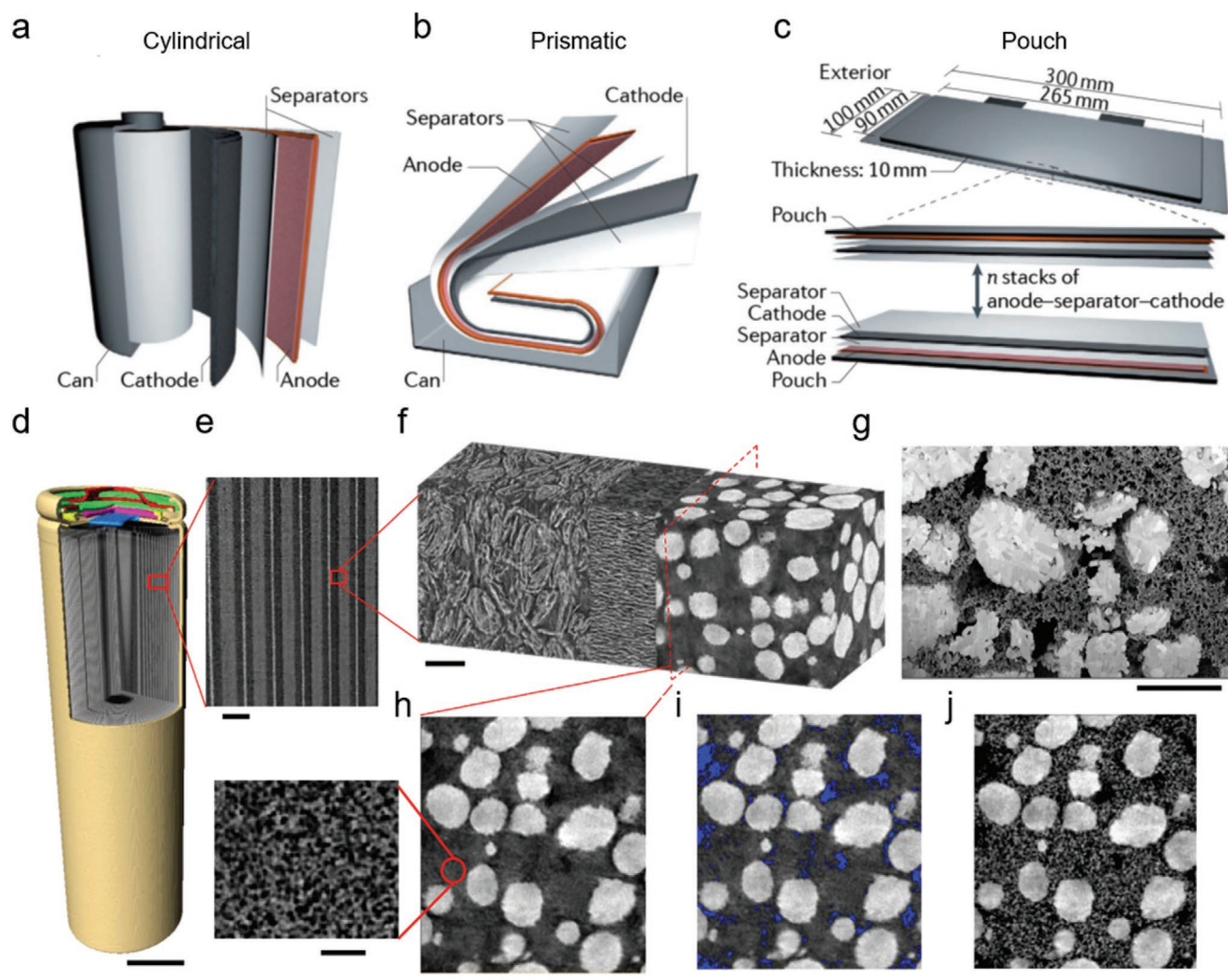


Figure 2. Three representative commercial cell structures, a) cylindrical-type, b) prismatic-type, and c) pouch-type. Reproduced with permission.^[46] Copyright 2016, Nature Publication Group. d) Volume rendering of a reconstructed cylindrical battery scanned by X-ray micro-CT. Magnified virtual slice showing e) periodic layered structure of the cell, f) configuration of the graphite anode, polyolefin separator, and lithium nickel manganese cobalt oxides (NMC) cathode (from left to right), g) SEM image of CBD surrounding NMC secondary particles, h) virtual slice of the 3D electrodes with an enlarged image of CBD phase, i) macro-pores indicated in blue, j) the resultant full microstructure of the NMC cathode. The scale bars in (d, e) are 10 mm and 240 μm respectively, 10 μm in (f–j) and 2 μm in the inset of (h). Reproduced with permission.^[48] Copyright 2020, Nature Publication Group.

Commercial LIBs commonly consist of a graphite anode, layered metal oxide cathode, and organic liquid electrolyte with polymer separator between the electrodes. They usually adopt one of three cell format types: cylindrical, prismatic, and pouch, as shown in **Figure 2a–c**.^[46]

Despite their commercial success, to meet the growing demands of the energy storage market there is a need to improve the energy and power densities of LIBs, as well as minimizing their performance degradation.^[47] Investigations of the fundamental processes in LIBs in representative environments and under electrochemical control are required to achieve these goals. This will allow us to develop a deeper understanding of the chemical, mechanical, and electrical stability of LIB electrodes, their morphological evolution and structural transitions, and the quantification of the reaction kinetics of important interfacial processes. However, the

electrochemical environment inside a battery is complex. For example, **Figure 2d–j** shows the configuration of a typical 18650 cell, revealed via X-ray CT. Double-side coated current collectors, cathode, separator and anode materials, electronic connections, safety devices and cell casing structures can all be seen. The electrodes themselves are composed of active materials that are mixed with conductive additives and a binder (carbon-binder domain, CBD). These components are usually mixed to form an ‘ink’ which is deposited as a film on a metallic current collector; these electrodes are compressed to increase density.^[48] Only a small excess of liquid electrolyte is used in most commercial LIBs. The electrodes therefore possess a compositional and structural heterogeneity over a wide range of length scales.^[49] However, in a majority of the in situ investigations undertaken to date, individual micro/nano-structured materials are targeted because of the

technical complexity required to ‘observe’ the buried interfaces inside batteries.

Many developments are needed to further improve battery technologies. Continued materials discovery, including those for both electrodes and electrolytes, is certainly required to provide batteries with significantly reduced cost, enhanced power and energy densities, and improved safety. For instance, silicon-containing anodes, nickel-rich layered cathodes, sulfur and oxygen cathodes, as well as Li-metal anodes with solid-state electrolytes (SSEs) are all exciting areas of development. However, advancing and optimizing new materials can be highly inefficient unless an understanding of their functional properties and degradation mechanisms are simultaneously progressed, both within their bulk and at the solid-liquid interface.

Although a tremendous amount of work has been carried out over the last three decades, the characterization at the electrode–electrolyte interface, in particular, is still a difficult, complex and disputed area of research. The deeper mechanisms of degradation are still somewhat ambiguous in most cases. Key open issues include SEI layer characterization, volume change of electrodes, dendrite formation, thin-film electrode evolution, intercalation/deintercalation processes, surface degradation and ion diffusion, detection of intermediates, electrical double-layer structure, and more.^[50] This is, in part, due to the complicated chemical, mechanical and geometric environment within batteries, meaning most imaging methods are unable to immediately and locally reveal the real interfacial properties and changes. In addition, the ‘cross-talk’ in full cells (reactions at the cathode affecting the anode and vice versa) is more complicated than in half-cell configurations.^[51] Compared to many other microscopies, EC-AFM provides the possibility to monitor the interface between an electrode and electrolyte with nanoscale resolution, revealing morphological and mechanical changes that can be linked to electrochemical phenomena. Nonetheless, EC-AFM and related SPM techniques still commonly rely on electrochemical environments that substantially differ from those in a real battery.

In EC-AFM and related SPM techniques the structure of the battery being studied is, in the vast majority of cases, much simpler than that of a real battery, discarding the closely and multiply stacked/wound parallel anode, separator/electrolyte, cathode layers found in cylindrical, prismatic, or pouch cells for a single working electrode that is well geometrically separated from any others, making enough space for the scanning probe. It is also common to utilize a three electrode system, introducing both a simple counter and reference electrode, as opposed to a second complex ‘active’ (e.g., a metal oxide based cathode) electrode, despite the fact that this will exclude any influence of the redox processes at this electrode on the electrochemical environment. The complex working electrode itself is also commonly replaced with a relatively flat analogue, highly unrepresentative of most battery electrodes, but often deemed necessary due to the perceived vertical height limitations with AFM. Finally, although many other differences exist on a case-by-case basis, it is usual to utilize a vast excess of electrolyte in these studies, in comparison to the ‘lean’ electrolyte conditions in many modern batteries, necessary to fully submerge all the electrodes and the probe. These simplified conditions are beneficial for expanding our understanding of the basic mechanisms occurring during battery electrochemical processes, in particular at the electrode/electrolyte interface (pseudo 2D). However, it excludes

contributions from more complex phenomena in 3D, such as electrode strain, electric field distribution, the nature of the conductive network and ionic transportation and more, all of which we must understand to help improve batteries. Hence it is essential that the data collected to date is critically appraised, considering the degree to which it can truly be used to expand our understanding of processes within real batteries.

3. EC-AFM for the Understanding of LIBs and Their Materials

In situ EC-AFM has been widely used to visualize the formation and evolution of SEI films, reveal particle expansion, strain, cracking and isolation, as well as measure mechanical and electrical properties of electrode and electrolyte materials.^[52] Below, progress made in the use of EC-AFM for analyzing the morphological, mechanical, and electrical changes in anodes, cathodes, and electrolytes using EC-AFM is reviewed and compared to that made using other prominent characterization tools. In each case, the unique capabilities of state-of-the-art EC-AFM analysis is discussed.

3.1. Anode Materials

3.1.1. Graphite Anode: SEI Characterization

Graphite is the most extensively used anode material in LIBs due to the reversible intercalation of Li ions between its layers at low potentials, leading to a theoretical capacity of 372 mAh g⁻¹.^[11] During the first cycle, an SEI passivation layer is formed on the graphite anode, driven by electrolyte decomposition that deposits inorganic and organic species. According to chemical composition analysis, such as X-ray photoelectron spectroscopy (XPS) and FTIR, the SEI layer generally contains a lower inorganic layer and an upper organic layer, which are mainly comprised of Li₂CO₃ and alkyl carbonates, respectively, depending on the type of electrolytes and additives.^[53–55] The formation of the SEI causes an initial irreversible capacity loss in the cell, but it is vital for its long-term cyclability, rate capability, self-discharge characteristics, and safety.^[56] Therefore, understanding and ultimately controlling the properties of the SEI layer at the graphite anode/liquid electrolyte boundary are of great importance for maximizing the performance and lifetime of LIBs. However, the structural features of the SEI are not easily observed by common microscopies, such as SEM and TEM, due to its fragility and sensitivity to atmosphere, electron beam damage and vacuum, as well as its amorphous nature. However, with the unique advantages described above, in situ EC-AFM has been proven to be a powerful tool to visualize and investigate the SEI.

Highly oriented pyrolytic graphite (HOPG) is the most commonly-adopted type of graphite used for AFM studies, instead of less ordered graphite materials (more typical of those used in real battery systems), because it can be cleaved to leave flat surfaces of relatively large areas. Early AFM studies of SEI formation on HOPG confirmed that SEI layer deposition occurs below 0.9 V (all potentials in this review are referenced vs.

Li/Li⁺, unless otherwise specified), followed by lithium intercalation below 0.2 V.^[57,58] Other similar investigations have been conducted with a particular focus on the effect of electrolyte composition on the SEI morphology.^[59,60] Through the use of in situ AFM, the following conclusions have been drawn: The electrolyte solvent (e.g., ethylene carbonate (EC), diethyl carbonate (DEC), propylene carbonate (PC)), or electrolyte salt (e.g., LiPF₆, LiClO₄), has a significant influence on the nature and quality of the SEI layer, and therefore battery performance.^[61–64] Using additives (e.g., vinylene carbonate (VC), fluoroethylene carbonate (FEC), and ethylene sulfite (ES)) is one of the most effective and economical ways to improve SEI morphology and stability.^[65–68] Factors such as operating temperature and electrolyte concentration have a great influence on the structure and properties of the SEI layer formed.^[69–72]

In general in situ EC-AFM imaging on HOPG in LIB electrolytes shows that an SEI with a thickness of 1–200 nm is usually observed on the first cycle,^[73–75] although many studies show continued growth during subsequent cycles,^[76] which is somewhat at odds with the general perception that a stable and consistent SEI forms in commercial cells on the first cycle.^[56] These studies also observe a very inhomogeneous SEI structure, with an accumulation of SEI at the well-defined step edges.^[77,78] This is expected as lithium ions only intercalate into graphite via the edge plane, rather than through the basal plane,^[79] meaning step edges experience a higher Li⁺ flux and faster electron transfer kinetics.^[80] Combined with effects from the higher step edge density of functional groups and defects,^[81] it is therefore unsurprising that a thicker SEI and higher local current density results.^[82] These edge effects may be exacerbated as in situ AFM studies have also indicated that the electrochemical reactions between cations/anions at graphite edges induce exfoliation, causing anode degradation.^[83] This exfoliation has been attributed to 1) the mechanical stress induced from the co-intercalation species, and 2) subsurface gas evolution resulting from the electrochemical reduction of co-intercalated solvent molecules at lower voltage (<0.6 V).^[84]

While beyond the scope of this review, it is interesting to note that although anion intercalation into the graphite layers is undesired in LIBs, intercalation of anions such as PF₆⁻ between carbon layers contributes to the energy capability of dual-ion batteries (DIB) at high potential when it is used as a cathode.^[85] In situ AFM has been employed to observe this intercalation above 4.8 V,^[86] demonstrating that PF₆⁻ intercalates in one of every three graphite layers with an intercalation speed of 2 μm min⁻¹. It was shown that the graphite wrinkled and suffered structural damage at high voltages, along with severe electrolyte decomposition on the surface, both of which account for the degradation of the cycling performance of DIBs.

Alongside in situ analysis of the morphological and chemical properties of the SEI as it forms, it is also important to understand its mechanical properties; a mechanically unstable SEI can be a driver for increased rates of degradation. The Young's modulus of a LIB anode surface is known to change as electrochemical processes proceed and SEI forms, resulting in inhomogeneity over the anode surface.^[87] To uncover the mechanisms behind this, Deng et al. used EC-AFM on HOPG (in an electrolyte of lithium bis(trifluoromethane sulfonyl) imide (LiTFSI)/EC/DEC) to show that the initial SEI formed had insufficient electron blocking ability to hinder further growth, meaning

the thickness of the SEI increased as cycling proceed;^[87] the Young's modulus of the SEI was measured to vary between 23 and 67 MPa across the surface. It was later shown by Shen et al. using EC-AFM that FEC-based electrolytes enable the formation of an LiF-rich SEI that is harder and denser (average 1498 MPa) than that formed in equivalent EC electrolytes (average 916 MPa).^[88] This system can also suppress Li-dendrite growth, which was attributed to a higher mechanical strength and larger resistance of the SEI layer, preventing reduction and deposition of Li⁺ ions on the anode surface. This shows that an SEI layer with a uniformly high modulus is important for maintaining the cycling stability of electrodes. The impact of electrolyte composition on SEI stability is supported by the wide variation in measured Young's modulus of the SEI by EC-AFM in different reports. For instance, it has been shown that the presence of imide-based Li salts (e.g., LiTFSI) induces a thinner and less thermally stable SEI layer than using VC additive,^[89] which might lead to smaller Young's modulus (45 MPa) of the SEI.^[87] This is contrasted with an aqueous electrolyte with LiTFSI, which led to a Young's modulus of 30 ± 10 GPa for a 4–6 nm thick SEI layer.^[90] Work which combined AFM and atomistic simulations indicated that the Young's modulus of SEI layers (1 M LiPF₆ in EC/dimethyl carbonate (DMC) 1:1) can have a wide variation that ranges from 2.4 GPa to 58.1 GPa, depending on polymeric, organic, and amorphous inorganic components.^[42]

Recent measurements have compared the morphological and mechanical SEI changes at both HOPG and industry-relevant graphite anode materials through operando EC-AFM.^[91] It was found, via continuous imaging, that on HOPG the SEI forms simultaneously in two distinct morphologies at the edge and basal planes of graphite (**Figure 3**). The SEI at edge sites is much thicker and softer than that at the basal plane. In addition, VC/FEC additives in an EC/EMC (ethyl methyl carbonate) electrolyte were shown to induce reduced SEI thickness and roughness and increase Young's modulus, which would lead to enhanced battery performance. When compared with operando EC-AFM of individual, commercial-battery-relevant graphite particles, it was clear that the same basic processes occur at HOPG and the graphite particles, but the significantly different starting material structure (density of step edges, size/consistency of particle, mixed-size particles, strain behavior) leads to different behavior; the graphite particles displayed more SEI covering and a lower SEI modulus due to their high edge-to-basal ratio. This difference would have a significant impact on device performance, correlating with the differences observed between HOPG investigations and coin cell measurements.

Combining in situ EC-AFM with other analytical methods has allowed a more detailed picture of the SEI formation, composition and structure to be revealed. For example, comparative analysis of SEI composition has been undertaken with combined surface averaged neutron reflectometry (NR)^[92] and in situ EC-AFM. The information on SEI composition, thickness and roughness, provided by NR at ≈Å height resolution complemented the high lateral resolution provided by EC-AFM. Similarly, combining ex situ XPS with in situ EC-AFM on HOPG has revealed a two-layer SEI structure (**Figure 4a–d**). The SEI layer was found to be composed of a soft upper layer which could be easily scratched away with the AFM probe and a hard lower layer that remained after scratching, covering both

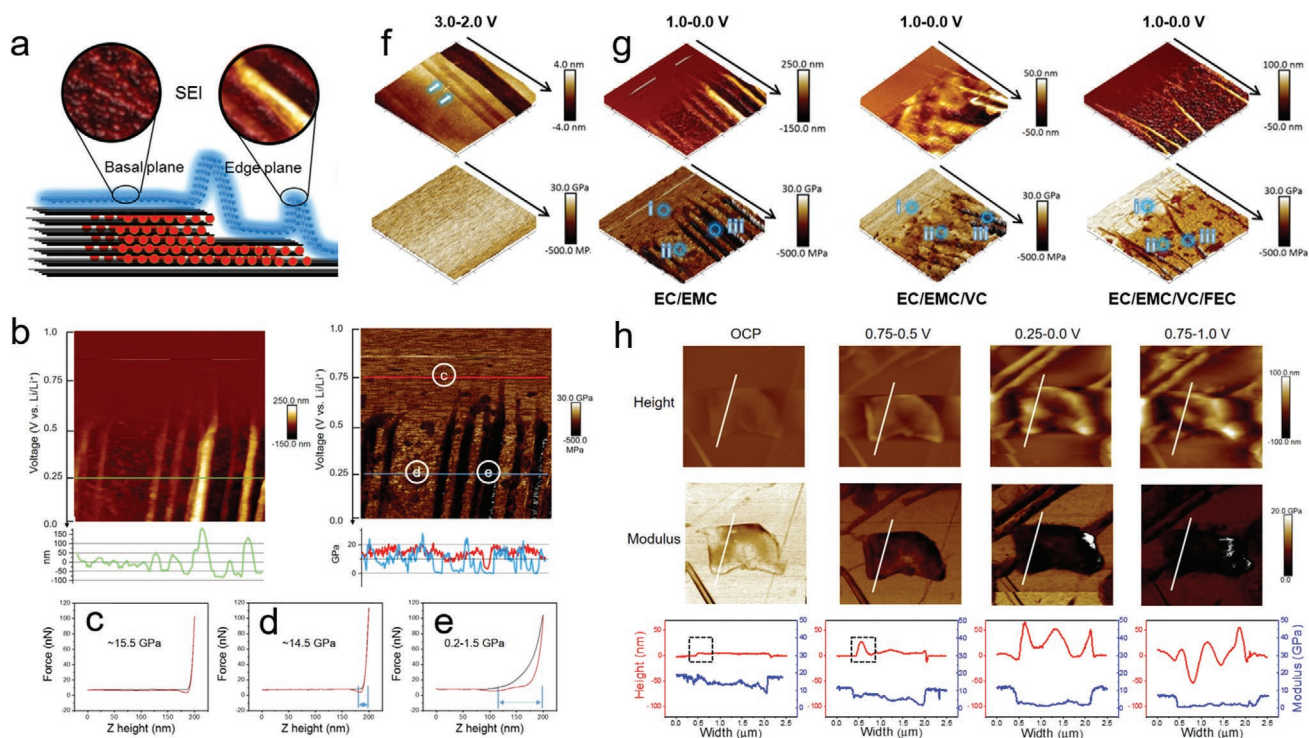


Figure 3. a) Schematic of the different SEI morphology at the edge and basal planes of a graphite anode. b) Enlarged images of height (left) and modulus (right) mapping of a HOPG surface in an EC/EMC electrolyte between 1.0 and 0.0 V. In c–e) force–distance curves of the three selected spots in (b) are shown. f) and g) show 3D images of height (upper rows) and modulus (lower rows) obtained in EC/EMC between (3.0–2.0 V) (f), and 1.0–0.0 V in EC/EMC, EC/EMC/VC, EC/EMC/VC/FEC (g) during the first discharge process, depicting the SEI formation. h) Similar height increase and modulus reductions observed on an individual graphite sheet. All images are in an area of $10 \times 10 \mu\text{m}$. Reproduced with permission.^[91] Copyright 2020, American Chemical Society.

edges and basal planes of graphite.^[93,94] The XPS results of the two different SEI sublayers confirmed the organic nature of the soft upper layer and the salt-like nature of the hard under layer. The SEI was later revealed to have an even more complex structure by combining electrochemical quartz crystal microbalance (EQCM) data with morphological change information indicated by EC-AFM of HOPG.^[95] Quantitative monitoring of the interphasial component mass change by EQCM confirmed the SEI formed in five distinct stages (Figure 4e–m): 1) LiF formation at 1.5 V (Figure 4h); 2) co-intercalation of $\text{Li}^+(\text{solvent})_x$ at 0.88 V (Figure 4i); 3) initial EC reduction at 0.74 V (Figure 4j); 4) major EC reduction at lower potentials (Figure 4k,l); 5) lithium alkylcarbonates produced by EC reduction were partially re-oxidized during anodic scan above 0.3 V (Figure 4m). While EQCM can provide electrode mass change information during electrochemical reactions, in situ EC-AFM images reveal how the HOPG interacts with Li^+ during the initial lithiation and delithiation processes, establishing an atomistic picture for the formation mechanism of the SEI.

It is clear from these studies that EC-AFM can reveal interesting processes at graphite anodes, including a complex and evolving SEI. However, on the whole, these findings have been shown at the surface of highly ordered, flat electrodes (i.e., HOPG). This structure contrasts to that found in ‘real’ LIB anodes, as described above. It has been shown that there are changes in SEI behavior when simply moving from HOPG to a single graphite particle,^[91] so it could be reasonably assumed

that there would be a greater difference at a full and complex battery anode, particularly when natural graphites are used that have a highly roughened surface.

Like EC-AFM, neutron scattering techniques are well suited to SEI investigations due to their ability to provide atomic resolution and sensitivity to light elements, including lithium. As a probing species, neutrons have the benefit of a high penetration depth allowing investigation of layered samples buried within other solid components, and thus unlike most other characterization techniques allows investigation in full cell configuration (with current collectors, separators and casings, etc.). Atomic-scale structural and compositional insight into the mechanism of SEI formation and evolution are critical parameters that can be observed with NR,^[96,97] alongside insight into the evolution of the underlying electrode materials, including Li intercalation and volume expansion.

The main drawback of NR is the requirement for extremely thin and smooth samples, such as Cu ^[96] or carbon deposited on silicon.^[97] These are highly unrepresentative of true LIB anodes. In comparison, small-angle neutron scattering (SANS) is a powerful method for determining the average morphologies of nanostructures, based on the difference in scattering length density between components, on the order of 1–100 nm.^[98] Collected data is representative of the entire cm-scale sample, thus allowing investigation of commercially relevant battery electrodes within full cells, but it must be acknowledged that these data provide an average structure weighted toward the

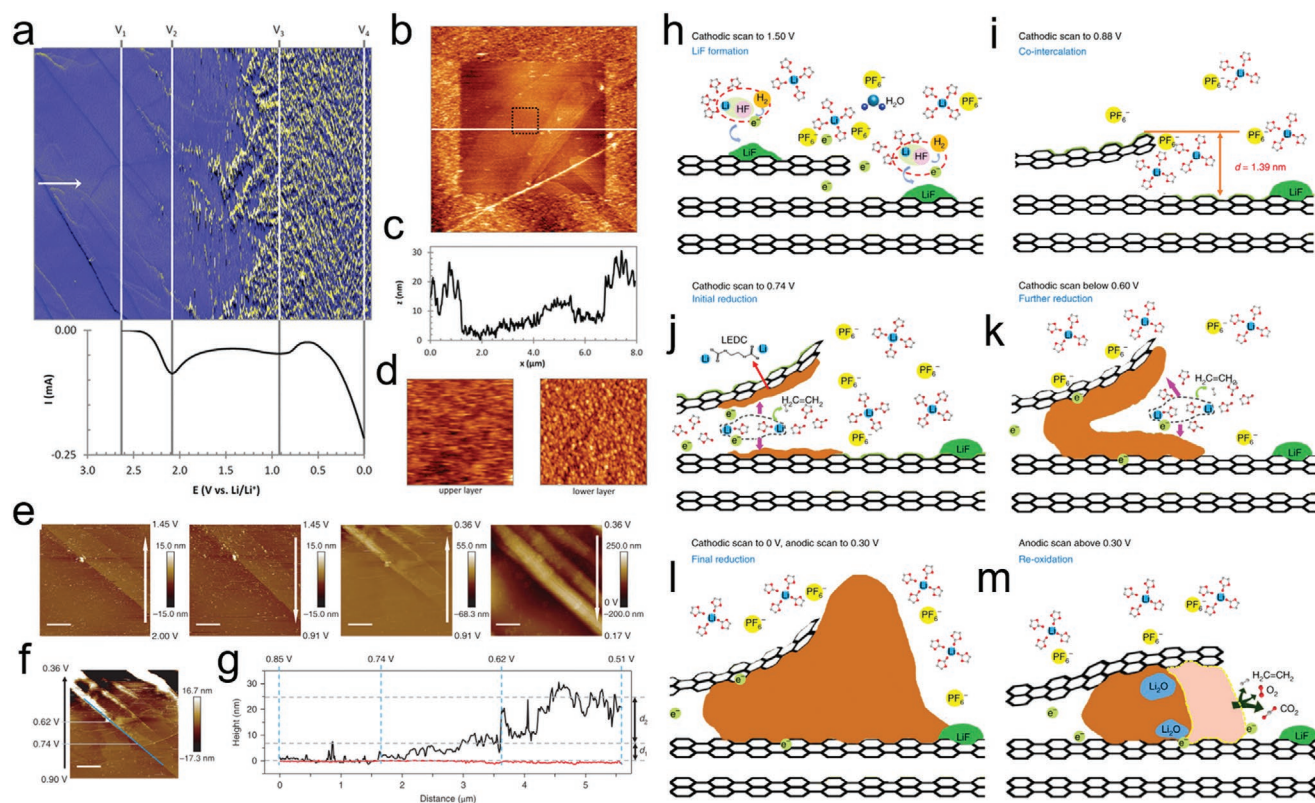


Figure 4. a) Formation of SEI on a HOPG surface in 1.5 M LiTFSI dissolved in EC during a cyclic voltammetry (CV) scan (5 mV s^{-1}) over an area of $3.5 \times 4.5 \text{ }\mu\text{m}$. b) Topographic AFM image ($8 \times 8 \text{ }\mu\text{m}$) at 0 V after repeated scanning of the inner $5 \times 5 \text{ }\mu\text{m}$ region. c) Line profile of the white line in (b). d) The features of the upper and lower SEI layer in the black dotted ($1 \times 1 \text{ }\mu\text{m}$) region. Reproduced with permission.^[93] Copyright 2014, American Chemical Society. e) Morphological observation of the SEI via in situ and operando EC-AFM measurements during the first lithiation of HOPG. f) Correlation of morphology and potential during the cathodic scan. Scale bars are $1 \text{ }\mu\text{m}$. g) Height distribution along the blue line in (f). h–m) Schematic illustration of the interphasial formation chemistry during the first lithiation. Reproduced with permission.^[95] Copyright 2019, Nature Publishing Group.

strongest comprising scatterers. This means localized or site specific processes are difficult to uncover. Therefore, although neutron scattering techniques can provide insight into the evolution of SEI chemical and morphological properties, there is a trade-off between site specific knowledge and the level to which the electrochemical environment represents commercial batteries. EC-AFM, in comparison, can be seen to provide direct observations of localized morphological and mechanical properties at very small lateral scales (1–20 nm), as electrochemical cells operate. However, to date investigations using EC-AFM to study graphite anodes have relied overly on model electrodes, limiting the degree to which the data collected can apply to industry-relevant battery systems. Although coupling these EC-AFM measurements with data from neutron techniques is an exciting route to support the proposed models,^[92] there also would be enormous value in improving the industry relevance of the anode structures and electrochemical environments utilized in EC-AFM tests.

Another commonly-employed experimental technique to investigate graphitic battery materials is microbeam Raman scattering. The relative intensity of G- and D-peaks is commonly used to infer information about the nature and concentration of defects within the graphitic materials, predominantly to characterize the graphitic anodes before cycling or as part of ex situ, post cycling studies.^[99] For graphite anodes in LIBs,

analysis of the G-peak has been used during operando and in situ charging studies to reveal that the intercalation occurs in distinct steps forming high stage graphite intercalation compounds (where ‘stage’ refers to the number of graphite layers between each of intercalant) eventually forming stage 1 LiC_6 at full charging.^[100–102] For hard carbon-based electrodes, by fitting the G-peak position and width with doping, it has been shown that Na-ion intercalation is incremental (and associated with the sloping part of the voltage profile),^[103,104] similar to the incremental charging found in single to few layer graphene.^[105] However, the lateral resolution limit of Raman scattering is far larger than for AFM, being limited by the diffraction limit of light, thus blind to the detailed atomic-scale changes that can occur. Similarly, while Raman scattering can provide information of chemical changes that are occurring in a particular sample, it is very much material specific and features from one material can completely obscure those of another. Nonetheless, Raman and EC-AFM have great potential for complementarity, pairing nanoscale morphological and chemical characterization.

3.1.2. Si and Other Alloy-Type Anodes: Volume Change

Alloying anodes (e.g., Si, Sn, Ge, Al, SiO) hold great promise for LIBs due to their high theoretical specific capacity (e.g.,

4200 mAh g⁻¹ for Si).^[106] With these materials an SEI layer forms on the anode surface at a potential of ≈0.68 V (for Si) during the initial cycle, as with a graphite anode, but this is followed an alloying reaction with lithium below 0.25 V.^[107] The lithiated amorphous alloy phase (e.g., Li₁₅Si₄) enables these materials to possess large specific capacity, but is accompanied by significant volume expansion, which causes particle fracture and pulverization. This leads to particle isolation and failed electrical contacts, leading to capacity loss.^[108] The SEI is also damaged during this expansion/contraction, leading to it reforming on subsequent cycles, increasing irreversible capacity losses and lowering the Coulombic efficiency.^[4] Many approaches have been attempted to solve these problems, such as carbon coating,^[109] structure engineering,^[110] and electrolyte optimization,^[111] but alongside device performance more evidence is needed to confirm the mechanisms behind the success of these strategies; this is possible with EC-AFM.

Silicon is the most widely studied alloying material for LIB anodes to date. Due to the anisotropic lithiation and volume expansion, polycrystalline Si-particle-based anodes show a dramatic increase in surface roughness.^[112] By contrast, amorphous Si (or indeed Sn) has been found to effectively alleviate the negative effects of volume expansion and contraction.^[113] This differing behavior in volume change between crystalline and amorphous Si has been evaluated using patterned electrodes via in situ EC-AFM. Although the amorphous phases also suffered from large volume expansions, their shape and volume changes have been shown to be reversible due to the homogeneity in expansion and contraction, which resulted in better stability than crystalline Si materials. This led to thin films of amorphous Si, and a Si_{0.64}Sn_{0.36} alloy, showing good capacity retention after long-term cycling.^[113] Later, the relative degree of volume change of amorphous ‘Si pillars’ was shown to depend on their initial size, such as diameter and height of the pillars.^[114] The theoretically expected volume expansion of ≈300 % was only achieved for Si pillars with diameters larger than 200 nm, whereas the volume expansion of the 100 nm pillars was limited to below 200 %.

Interestingly, a volume expansion ratio of ≈420% has been found for Sn particles during sodiation.^[115,116] To alleviate the expansion of Sn anodes, Sn_{1-x}Co_xC_y alloys with different compositions were proposed, and using in situ EC-AFM it

was confirmed that the volume expansion could be lowered to 142–204%, depending on the composition.^[117]

To withstand the large volume expansion of Si anodes, a robust and stable SEI layer is important to maintain battery performance. As with graphite anodes, SEI layer degradation at alloying anodes may be evaluated using EC-AFM.^[118] SEI thickness, mechanical strength, electrochemical stability, and resistance have all been studied, exploring the effect of factors such as electrolyte composition,^[119–121] additives,^[122] temperature,^[123] crystal plane orientation,^[124] binder materials,^[125] and more. Similarly, it has been shown that the battery operating conditions may also influence the properties of alloying anode SEIs.^[118] A combination study of electrochemical impedance spectroscopy (EIS) and the potentiostatic intermittent titration technique (PITT) with in situ EC-AFM found that a longer duration at higher potentials (i.e., at full charge) produced a softer SEI with mesoporous structure and lower ionic conductivity; by contrast, lower potentials led to more inorganic phases with higher elastic moduli, as shown in **Figure 5a**.^[126] In fact, it has been shown that SEI layers continuously change during electrochemical cycling of Si anodes. During the first lithiation, the modulus of the SEI layer has been found to decrease with the increased degree of lithiation, only partially recovering upon delithiation.^[127,128] In subsequent cycles, the thickness of inorganic constituents grows slowly, resulting in reduced SEI resistance and increased SEI mechanical strength.^[129] Surface coatings on the electrode have been shown to improve the quality of SEI layers. For instance, an atomic layer deposited 3 nm-thick Al₂O₃ layer was demonstrated to induce thinner and more stable SEI layers, thus improving capacity retention.^[130]

The use of ‘model’ alloying anode systems has enabled direct observations of mechanical degradation of SEI layers. For example, a patterned Si film (**Figure 5b**) was studied by in situ EC-AFM showing the crack formation on the Si film during the first lithiation.^[131] In the following cycles, the crack repeatedly opened and was filled with new SEI layer at lithiation and delithiation stages, respectively. Integrated ex situ focused ion beam (FIB) measurements, EC-AFM and finite element modelling later provided more detailed information about the SEI layer.^[132] As shown in **Figure 5c**, a bilayer structure of the SEI was observed, and tensile stresses in the SEI layer resulted in through-thickness cracks that appear at the rim of the outer SEI.

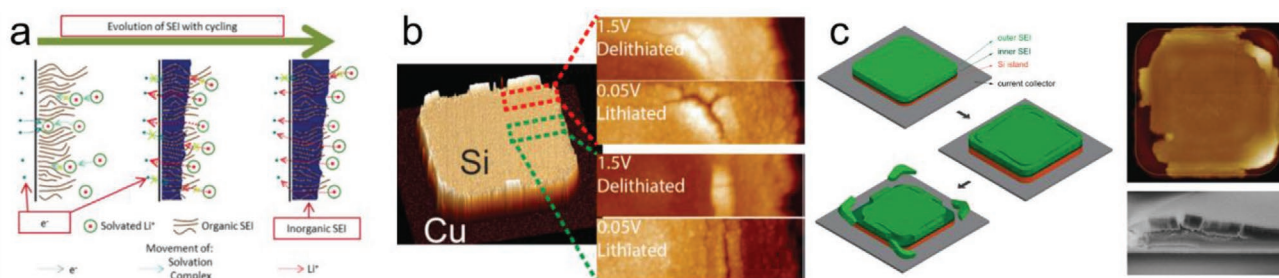


Figure 5. a) Model for the SEI growth showing that initially mesoporous organic material forms at higher potentials, then an inorganic SEI forms at lower potentials and continues to fill the pore space during subsequent cycles. Reproduced with permission.^[126] Copyright 2016, Wiley-VCH. b) AFM images (7 × 2 μm) showing the cracking of a patterned Si film (≈15 × 15 μm) due to volume change during electrochemical cycling. Reproduced with permission.^[131] Copyright 2016, American Chemical Society. c) Sketch figure, AFM image, and diagonal FIB cross-section of the Si anode (≈15 × 15 μm) with a double-layer SEI structure. Reproduced with permission.^[132] Copyright 2020, Elsevier.

These continue to delaminate and crack with subsequent cycles. The inner layer, on the contrary, had a high fracture toughness and was well adhered to the underlying Si. Delamination at the rim from loosely attached SEI was therefore thought to be a result of interfacial instabilities from the repeated expansion and contraction of Si. This multi-layered SEI layer was confirmed in another study, and 3D Young's modulus mapping was obtained using the scanning force curve method.^[133]

It can be seen that studies of alloying anodes with EC-AFM rely, possibly to an even greater degree than for graphite, on greatly idealized anode material analogues. In the cases where Si has been utilized in real battery systems, it typically consists of a low fraction of a nanoparticle additive held within a carbon (conductive and graphitic) framework with a binder.^[134,135] This differs greatly from, for example, lithographically patterned Si thin films, which may mean the real physical phenomena that define the challenges of alloying anodes diverge from those observed on these model systems.

Detrimental pulverization of alloying materials has also been studied by using various other characterization methods. Among them, in situ TEM has the ability to directly observe volume change, phase transformations, elemental mapping, and the development of crystalline defects during electrochemical processes through in situ experiments.^[136] The new understanding of material change that this technique has provided has greatly enhanced the development of alloy-type electrodes, by informing improvements in the electrode stability via surface and nanoscale engineering.^[137] In addition, due to the high spatial resolution and capability to produce elemental maps, the structure of the SEI layers on alloying electrodes can be analyzed by cryogenic-electron microscopy (Cryo-EM).^[138]

The use of EMs for battery analysis does, however, also have drawbacks: 1) The energy of the incident electron beam is high, which may cause side reactions in sensitive materials, adversely affecting the imaging process and giving misleading information; 2) electrolyte-free experiments are common, where lithium metal with a significant surface oxide is used as the counter electrode, the Li₂O acting as a solid electrolyte,^[139] a geometry that is enormously divergent from that in real batteries; 3) thin-film liquid cells also differ greatly from realistic batteries due to their highly unrepresentative mass transport regimes; 4) complex specimen preparation is needed, as very thin films are commonly required.^[140] Comparatively, the visualization of structural and property changes provided by EC-AFM can be achieved in more representative electrochemical environments compared to 'real' batteries. Similarly, more realistic battery materials can be studied, although further efforts are needed to improve this. Hence, with the advantages of in situ imaging in a commercial liquid electrolyte and electrode surface mechanical measurements, AFM offers distinct advantages for detecting material structural evolution and SEI properties. When combined with multi-modal analytical techniques, for example dilatometry,^[141] chemical composition and electrochemical tests, in situ EC-AFM can provide a deep understanding of electrode expansion and capacity fading.

3.1.3. Li Metal Anode: Dendrite Formation

The demand for high-energy-density next-generation batteries requires using electrode materials with higher theoretical

capacity. Li metal anodes, with a specific capacity of 3860 mAh g⁻¹ and electrochemical reduction potential of -3.04 V versus the standard hydrogen electrode (SHE), may be the ideal candidate.^[142] However, non-uniform metal stripping and deposition upon cycling, partly originating from the presence of discontinuous SEI layers, leads to dendrite formation. This not only reduces the Coulombic efficiency, results in lost lithium inventory and consumes electrolyte, but can also cause internal shorting, potentially leading to thermal runaway, cell fires and explosion.^[143] Studying the interfacial processes at Li metal anodes during Li plating and stripping is crucial for understanding this mode of battery failure and for improving the design of future LIBs.

The earliest lithium deposition study by in situ EC-AFM was achieved in 1996, an early demonstration of the applicability of this non-destructive characterization method.^[144] It has been shown that the structure of the Li surface consists of grain boundaries, ridge-lines, and terraces, which induce an uneven SEI layer in electrolytes.^[145] In addition, 3D AFM morphology images have revealed the swelling and shrinking of the Li surface during the deposition and stripping processes.^[146] This means the SEI layer must accommodate significant morphological changes; otherwise, breakages, cracks or any heterogeneous conditions of the Li metal surface can drive lithium dendrite growth.^[147] Therefore, it is generally believed that a SEI with a high modulus must be formed if the growth of Li dendrites is to be suppressed or prevented.^[148-150]

To date, various methods aiming to engineer the electrode—electrolyte interface have been shown to be effective in optimizing the SEI layer and suppressing lithium dendrite growth. Strategies include optimizing electrolyte composition,^[151] using additives,^[152] constructing an artificial SEI,^[153,154] use of graphene,^[155,156] or covalent organic framework protection layers,^[157] and lowering anode roughness and stress.^[158,159]

A smooth and flexible SEI on an Li metal anode, which appears to be mainly determined by electrolyte composition, is thought to mitigate dendrite nucleation and growth in the electrolyte.^[160,161] For example, the concentration of lithium bis(fluorosulfonyl)imide (LiFSI) in the electrolyte was demonstrated by in situ EC-AFM to significantly influence the thickness, roughness and modulus of the SEI layer on a Li metal anode.^[162] A moderate concentration of LiFSI generates a rigid LiF-rich SEI with a modulus of 10.7 GPa, which is much higher than the threshold value for Li dendrite penetration, providing sufficient protection to the anode. A LiF-rich SEI has high chemical stability, low solubility in carbonate-based electrolytes, and high shear modulus.^[163] In addition, a mixed multi-layered SEI structure has been shown to offer coupled rigidity and elasticity.^[164] For example, Gu et al. developed an electrochemical polishing method that produced an inorganic-rich and organic-rich multi-layered SEI on a lithium metal anode (precisely probed by force curve analysis via AFM), which effectively suppressed dendrite growth.^[165] Alternatively, according to a study comparing the Li plating at different operation temperatures, it was suggested that it is not necessary to construct a high modulus SEI layer, rather it is essential to decrease the surface tension and increase the elasticity of SEI to achieve a stable and dendrite-free Li anode. It was also shown that a lower temperature (-15 °C) induced a higher modulus SEI layer than that obtained at higher temperature (60 °C).^[166]

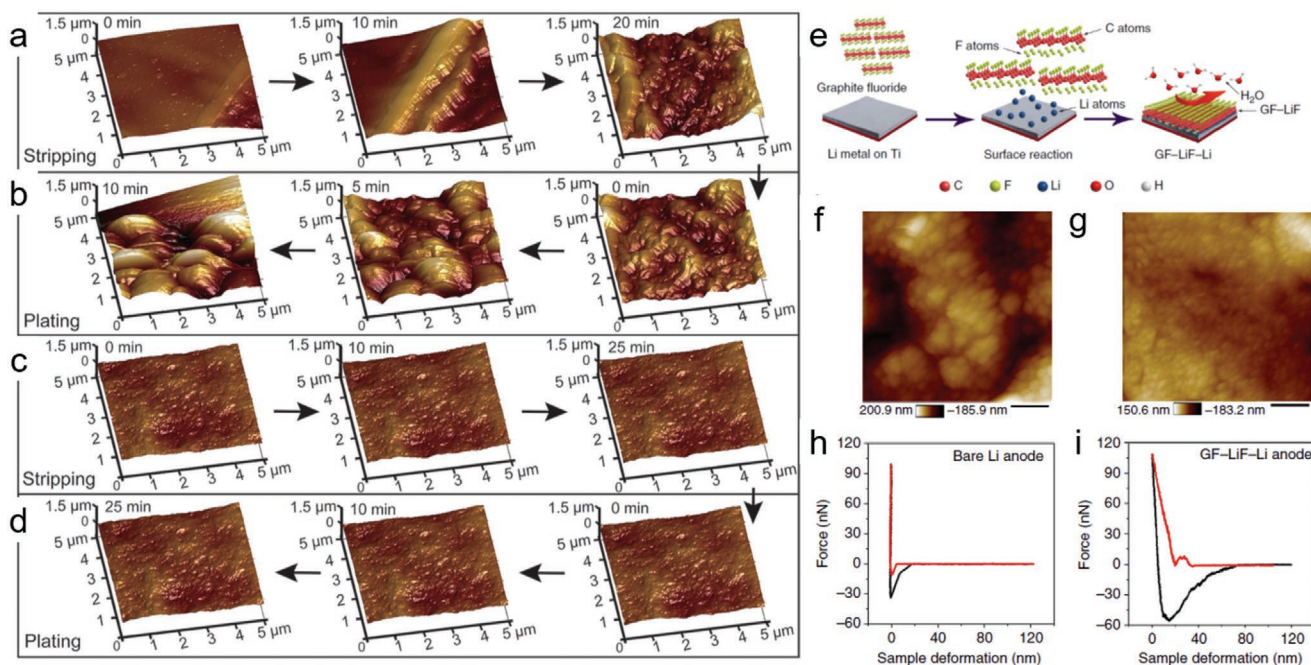


Figure 6. AFM images of a pristine Li anode during a) stripping and b) plating processes, and LiPAA modified Li anode during c) stripping and d) plating processes. Reproduced with permission.^[169] Copyright 2018, Wiley-VCH. e) Schematic illustration of graphite fluoride - lithium fluoride protected Li (GF-LiF-Li) preparation and its protective effect for Li metal anodes. f–g) topography images (scale bars are 400 nm), h,i) indentation curves of SEI layer on bare Li (f, h) and GF-LiF layer (g, i). Reproduced with permission.^[171] Copyright 2019, Nature Publication Group.

Rational design of a stable artificial SEI with a controlled structure and stability is an exciting route to controllably suppress a constantly reforming SEI, preventing dendrite growth.^[167,168] Li et al. have shown that a Li polyacrylic acid (LiPAA) SEI layer could mediate the dynamic Li plating/stripping processes by self-adapting interface regulation.^[169] Using in situ EC-AFM it was demonstrated that the LiPAA polymer SEI could accommodate the deformation of Li and restrain the dendrite structure (Figure 6a–d), leading to a much smoother anode morphology after plating/stripping. Similarly, Gao et al. utilized a reactive polymer composite as the SEI precursor, introduced on the surface of Li metal, which formed an SEI layer with excellent passivation properties, homogeneity, and mechanical strength. It consisted of a polymeric lithium salt, lithium fluoride nanoparticles, and graphene oxide sheets.^[170] Shen et al. used graphite fluoride (GF), enabling a more elastic and flexible protective layer (confirmed by AFM indentation tests) for preventing dendrite growth during the electrochemical cycling (Figure 6e–i).^[171]

Unlike graphite or alloying anodes, where model anode analogues are widely used, studies of Li metal anodes utilize electrodes that do truly represent those found in full cells. This means it may appear more straightforward to transpose these findings to the understanding of commercially relevant battery systems. However, these studies are still commonly undertaken in cells with a significant excess of electrolyte, an unrepresentative cell geometry (non-parallel electrodes, large electrode separation) and without a separator in physical contact with the Li metal surface. Hence, comparison of any data collected with that from techniques that can study more representative cells would be of great benefit.

Continuous monitoring of metal dendrite growth during electrochemical plating/stripping cycles has been conducted by various microscopies.^[172] However, in most cases, lithium dendrites grow large and fast, so monitoring the microstructural evolution of lithium morphologies in real-time is important. One time-resolved characterization technique, successfully adopted for elucidating changes of dendrites at the micron-scale, is in situ optical microscopy (OM). OM requires transparent view-of-field on the target area, which means no separator and excess electrolyte is generally used in the in situ cells, hence experiments are unrepresentative of a real battery configuration. Nonetheless, this flexible technique can be easily utilized for in situ experiments, allowing it to be adopted to compare the effects of various conditions on the suppression of dendrite growth by directly measuring the uniformity and kinetics of plating reactions.^[173–175] For example, when used to validate the effectiveness of modifying electrolyte composition on dendrite growth, in situ OM has clearly shown growth was smoothed in tailored electrolytes, compared to the mossy structures grown in standard carbonate-based electrolytes.^[176] It has also been possible to identify similarities and differences of lithium penetration mechanisms through pre-existing defects of various SSEs during galvanostatic lithium plating.^[177] However, despite having the resolution to visualize lithium dendrite growth, OM techniques lack the spatial resolution to study the initial stages of metal plating, which are key to control electrode morphology, as well as being blind to driving factors including SEI build-up.^[178,179]

The difficulty in controlling the position and speed of dendrite growth, along with their complicated and rapidly changing structure, means they can often be highly challenging to image

beyond their nucleation using AFM. Because of this OM is often better suited to capturing the progress of Li dendrite growth. However, by carefully controlling the electrode current density it is possible to utilize EC-AFM to reveal nanoscale changes at Li, or other metal, surfaces under electrochemical control. For instance, in situ EC-AFM imaging of Zn dendrite growth at low current density has been achieved, revealing the initial nucleation crystal morphology.^[180–182] The initial roughness of the Zn electrode surface was shown to be highly important in determining dendrite growth, a flatter Zn produced less dendrites.^[183] This was only possible by complimenting AFM data with that from OM. Hence, although EC-AFM can enable the versatile and realistic in situ/operando characterization of the morphological and mechanical properties of metal electrode–electrolyte interfaces with high spatial resolution, it is better applied to the study to the early stage of dendrite growth, such as the nucleation of Li metal, or for studying the fine structure of the SEI at metal interfaces. Nonetheless, these processes are of great significance to prevent dendrite growth and optimize the interface materials, and due to their instantaneous and nanoscale nature, they are less well understood.

3.1.4. Conversion Type Metal Oxide Anodes: Thin-Film Electrode Evolution

Metal oxides are widely investigated as substitutes for graphite anodes because of their much higher specific capacity, based on the conversion reactions with lithium, and their low cost.^[184] However, they experience large volume expansion upon lithiation, as the active material oxide reduces to form metal nanoparticles in a Li_xO_y matrix. As with alloying materials, this leads to not only pulverization and breaking of electrical contacts to conducting supports, but also repeated SEI formation, driving low Coulombic efficiency. Although engineering of nanostructured metal oxide nanoparticles is a common approach to mitigate these issues, using a thin-film electrode is a promising alternative. This architecture is advantageous because it provides shorter diffusion pathways for ions and electrons, although it is restricted in terms of volumetric and gravimetric capacities.^[185] As these metal oxide thin films are flat and require no binders/conducting additive materials, they are well suited for in situ EC-AFM studies.

Once again, EC-AFM studies of conversion materials have largely focused on observations of the structural evolution of the active material upon cycling and SEI formation/degradation. For example, in studies exploring the lithiation of CuO thin films prepared by sputtering, a “breathing” process involving the opening of cracks during charge (volume contraction) and their closure during discharge (volume expansion) has been observed by EC-AFM.^[185,186]

Alternatively, AFM topographical imaging and force spectroscopy measurements have been employed to examine the morphology, structure and mechanical properties, as well as the evolution of SEI, on MnO thin film anodes.^[17] Similar to other anode materials, the formation of SEI in EC-based electrolytes was observed to start at ≈ 0.8 V. Below 0.3 V the conversion of MnO into $\text{Li}_2\text{O}/\text{Mn}$ was observed, alongside excess SEI generation and the accumulation of lithium at grain boundary regions. Quantitative indentation tests of the SEI by AFM confirmed it

comprised of an inner inorganic layer and a soft outer organic layer, consistent with that found at carbon anodes.^[93] It was also shown via AFM and force spectroscopy that electrolyte additives affected the mechanical properties of the SEI layer on MnO.^[187] VC additives promoted a thick and soft SEI, which partially decomposed upon charging. This is again consistent with the findings at graphite.^[91] Bis(oxalate)borate (LiBOB) additives, alternatively, led to a thin, stiff and electrochemically stable SEI layer. However, although these properties are sought after for graphite, they were found to be unfavorable for accommodating the volume change of conversion anodes. Eventually, a combination of both VC and LiBOB was found to produce a stable SEI with moderate thickness and stiffness.

For investigating the electrode–electrolyte interfacial properties of thin-film electrodes, in situ EC-AFM is advantageous because of its ability to image surfaces at high resolution. However, although in thin films the surface constitutes a significant percentage of the material present, simply looking at an electrode interface can mean key processes that occur in the bulk are missed. This problem becomes more significant at bulk electrodes. In situ XRD measurements allow the study of buried crystalline materials, showing processes, including non-equilibrium phase transitions, with high precision and reliability.^[188] To achieve this, specialist electrochemical cells are needed to facilitate the entry of the incident, and exit of the diffracted, beam, which penetrates the electrodes and the electrolyte.^[189] This can cause issues in the case of thick film electrodes, and the cells can lead to non-uniform pressure on the electrodes within the cell and background diffraction features from the transparent window. Nonetheless, cells can provide an environment that is relatively similar to that in a coin cell.^[10] In one example study, Kim et al.^[190] studied a RuO_2 conversion anode in situ using a synchrotron XRD, showing the initial phase change from RuO_2 to LiRuO_2 , and the consequent conversion to Ru metal and Li_2O . However, inhomogeneity of electrochemical process are hard to understand as the data is averaged across a significant electrode area. XRD is also blind to amorphous materials, which are important in batteries. In situ EC-AFM and XRD experiments are, however, extremely complimentary; EC-AFM can be used to reveal local surface phenomena, while XRD probes the bulk. For example, these tools have been combined to provide detailed insights into the reaction pathways associated with the ZnO conversion and Zn alloying reactions using a pseudo-solid-state cell.^[191]

Similar to Si systems, most of the metal oxide anodes suffer from serious volume change during lithiation/delithiation, causing an unstable electrode structure, extra side reactions, and unsatisfactory cycling stability. Thin-film electrodes have been shown to alleviate many of these problems, and hence it may be suggested that the flat films utilized in EC-AFM studies might represent a real practical solution. However, outside of niche applications,^[192] thin film electrodes are unlikely to attract substantial commercial interest due to their highly limited energy density. Instead, if conversion materials are to find a widespread use in future batteries it is most likely to be as an active component held with in a bulk electrode matrix, much like the current use of Si and related alloying materials. Many reports on metal oxide anodes focus on improving the electrode structural stability using novel structures such as 3D hollow

spheres or with surface coatings.^[193] If EC-AFM experiments are to better reflect 'real' batteries, users should develop experiments to better investigate electrodes within this 3D geometry.

3.1.5. Insertion Type Metal Oxide Anodes: Conductive Phases

Metal oxide based insertion-type anodes are typically based on Ti, Nb, or V as the redox-active center (such as titanium oxides, niobium oxides, vanadium oxides).^[194] Titanium oxide, for example, uses the simple redox reaction between Ti^{3+} and Ti^{4+} during lithiation/delithiation, which does only provides relatively limited lithium storage capacity, but offers excellent cycling stability and the ability to cycle at high rates. These materials are therefore favorable for long cycle life, high power density applications.^[184]

$Li_4Ti_5O_{12}$ (LTO), the most widely studied metal oxide insertion anode material, has a relatively low capacity (175 mAh g^{-1}) and high redox voltage (1.55 V) compared with other anode types, meaning it has limited practical usefulness. However, it only experiences a 0.2% volume change of the spinel lattice, hence LTO has the merits of excellent mechanical stability and safety as an anode material.^[195] The nature of the surface layers on LTO has been a subject of controversy, with discussions of SEI layer formation,^[196,197] absence^[198] or continual dissolution^[199] being complicated by the delicacy of any layers formed and the limited ability of characterization methods to visualize their properties. Consensus was only achieved through the use of in situ EC-AFM imaging of the surface of LTO electrodes under controlled potential.^[200] It was demonstrated that rather than SEI formation in the common potential range of 2.5–1.0 V, an SEI layer formed on an LTO anode surface at a reduction potential of near 0 V. As a result, by controlling the SEI formation down to 0 V in the first cycle, improved LTO battery performance was achieved in the subsequent cycles in the normal range of 2.5–1.0 V.

Understanding exactly how the phase transformations occur within LTO is important for the design of anode materials and optimization of electrode performance. Unfortunately, the direct observation of the structural change between $Li_4Ti_5O_{12}$ and $Li_7Ti_5O_{12}$ crystals is difficult to characterize during lithiation/delithiation due to the zero-strain transition, unless employing in situ diffraction techniques such as neutron powder diffraction (NPD).^[201] However, due to the difference in electronic conductivity (i.e., $Li_4Ti_5O_{12}$ is electronically conductive and $Li_7Ti_5O_{12}$ is insulating), C-AFM provides the ability to locally monitor the phase transition.^[202] **Figure 7** presents the ex situ C-AFM characterization of an LTO film during a discharge/charge cycle. At various states-of-charge (SoC), current and topography maps of the LTO are shown to demonstrate the transition between the two phases by measuring their electronic conductivity. When combined with XPS results, C-AFM provides a more detailed understanding of the lithiation/delithiation mechanisms for insulated electrodes. It was determined that the transition of the two phases was via percolation channels in grains where the lateral propagation is forbidden across grain boundaries.

C-AFM is a very attractive method to investigate the conductance characteristics of electrodes at the nanoscale, a unique advantage over all other techniques. Moreover, by optimizing

C-AFM (with a linear current amplifier), scanning spreading resistance microscopy (SSRM) enables image acquisition of both electrical properties and topography images.^[203] However, the successful application of in situ/operando C-AFM in liquid electrolytes is only reported in a small number of cases. Which may be attributed to experimental difficulties such as rapid wearing of tips, degradation of image resolution, and low signal-to-noise ratio.

3.1.6. Layered Sulfide and Carbide Anode Materials: Mixed Storage Mechanisms

Layered materials beyond graphite, such as transition metal dichalcogenides and carbides, are a group of promising electrode materials for alkali metal ion batteries due to their theoretically high specific capacity. MoS_2 , the most widely studied transition metal dichalcogenide, has a graphite-like lamellar structure with a van der Waals gap that can accommodate the intercalation of Li/Na ions above 1.1 V. An irreversible conversion reaction to Mo and Li_2S occurs below this potential.^[204] The investigation of the reaction pathway of these insertion-conversion steps has attracted extensive research interest.^[205]

In situ EC-AFM investigation of the evolution of MoS_2 sheet anodes in a Na-ion electrolytes has demonstrated that SEI formation is initiated below 1.5 V, followed by the intercalation of Na ions around 1.1 V. The material was then found to 'wrinkle' at 0.4 V, which corresponded to the irreversible conversion from MoS_2 to Mo and Na_2S species.^[206] In another study, the interfacial processes of SEI formation and lithiation/delithiation on ultra-flat monolayer MoS_2 were monitored by in situ EC-AFM. Here, a chemical vapor deposition grown monolayer MoS_2 material was supported on, and electrically connected via, a Si substrate.^[207] The growth of ultra-thin SEI was quantitatively elucidated, as shown in **Figure 8**. The SEI film was found to initially nucleate in isolated areas before spreading across the entire electrode with a thickness of $0.7 \pm 0.1 \text{ nm}$, accumulating to a final thickness of $1.5 \pm 0.7 \text{ nm}$. The LiF-rich SEI film in an FEC-containing electrolyte was demonstrated to show a more sparse and stable wrinkling network after delithiation than that seen in an FEC-free system, leading to better performance. It must be noted, however, that although the authors show background data for the charging of the Si support between 1.23 and 1.0 V (their chosen cut-off voltage), Si is a non-ideal support material in most cases as it is itself capable of becoming lithiated (see section 3.2). In fact, these experiments were likely only possible as the authors did not cycle below 1 V. This did, however, mean they did not investigate the conversion aspect of the mechanism at all.

Titanium carbide ($Ti_3C_2T_x$, where T_x stands for surface terminations such as OH, = O and F), is an MXene, another class of layered materials that can be employed as anodes in LIBs due to their good electrical conductivity and the ability to host alkaline ions via intercalation into their layered structures.^[208] In situ EC-AFM has been used to monitor the macroscopic deformation in a delaminated Ti_3C_2 paper electrode in aqueous electrolytes containing Li^+ , Na^+ , K^+ , and Mg^{2+} .^[209] The electrode was found to undergo a large contraction during cation intercalation (except for K^+), differing from conventional electrodes that suffer

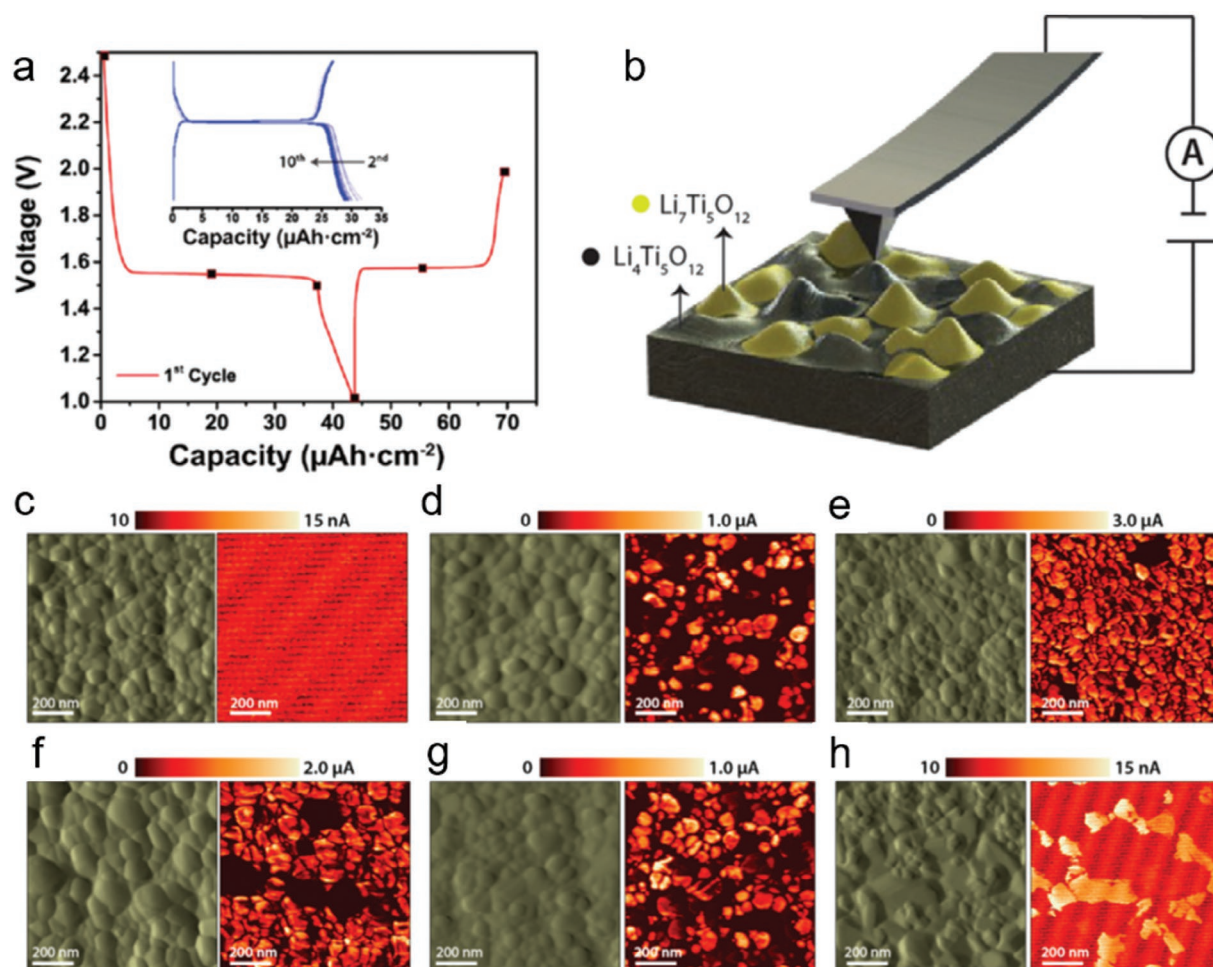


Figure 7. a) Electrochemical profile of the first charge/discharge cycle of a LTO film, with squares indicating points where samples were characterized. The first 10 cycles are inset. b) Illustration of capability of C-AFM to detect the presence of each phase due to their unique conductivities. AFM deflection (left) and current (right) images of LTO thin-films cycled to various SoC, corresponding to c) pristine, d) discharged 50%, e) discharged to 1.5 V, f) discharged to 1.0 V, g) charged 50%, h) charged to 2.0 V. Reproduced with permission.^[202] Copyright 2016, American Chemical Society.

from volumetric expansion, indicating that the deformation is strongly dependent on the charge/ionic radius ratio.

Although flat, planar material anodes beyond graphite are well suited to evaluation via AFM in liquid electrolytes, many of these materials are highly unlikely to ever be utilized in this format in commercial batteries, due to the problems of large initial capacity loss and high voltage plateau of the anode. If used, they are most likely to be held within a carbon and binder matrix, where they could suffer from issues relating to layer restacking and agglomeration.^[210] This once again raises questions of the relationship between the fundamental discoveries made by EC-AFM and real-world phenomena, but work to date undoubtedly shows EC-AFM can provide insight into how these layered materials should be incorporated into an electrode matrix for optimal performance.

AFM has limitations in its ability to observe intercalation/deintercalation of alkali metal ions into layered materials, such as long acquisition time, small observable scan areas, and depending on the probe selection, possible perturbation or damage of the thin layered materials. Specialist optical techniques are an alternative that are convenient for observing changes in layered materials with a larger field-of-vision during

electrochemical reactions. For instance, laser confocal microscopy combined with a differential interference contrast microscope uses a narrow laser beam to control depth-of-field and a pinhole to eliminate out-of-plane images, thereby increasing optical resolution and image contrast (revealing single atomic steps of $\approx 0.2\text{--}0.3\text{ nm}$).^[211] By capturing images at each plane slice, a 3D reconstruction image of the sample can be made. Atomic height resolution has been achieved in the study of the dynamic intercalation of Li ions into MoS_2 large single-crystal sheets, allowing visual contrast between lithiated and delithiated areas to be captured. In addition, optical transmittance microscopy is able to detect electronic transitions in active materials upon lithiation, which again is not possible with AFM. Within a planar microbattery, changes in optical transmittance, electrical resistance, and the nanoscale structure of MoS_2 during electrochemical lithium insertion have been observed in situ.^[212] This type of in situ observation at the single MoS_2 crystal scale offers strategies for enhancing the performance of layered electrode batteries, even though the situations (structures and surrounding environment) of layered materials in a ‘real’ battery are much more complicated.

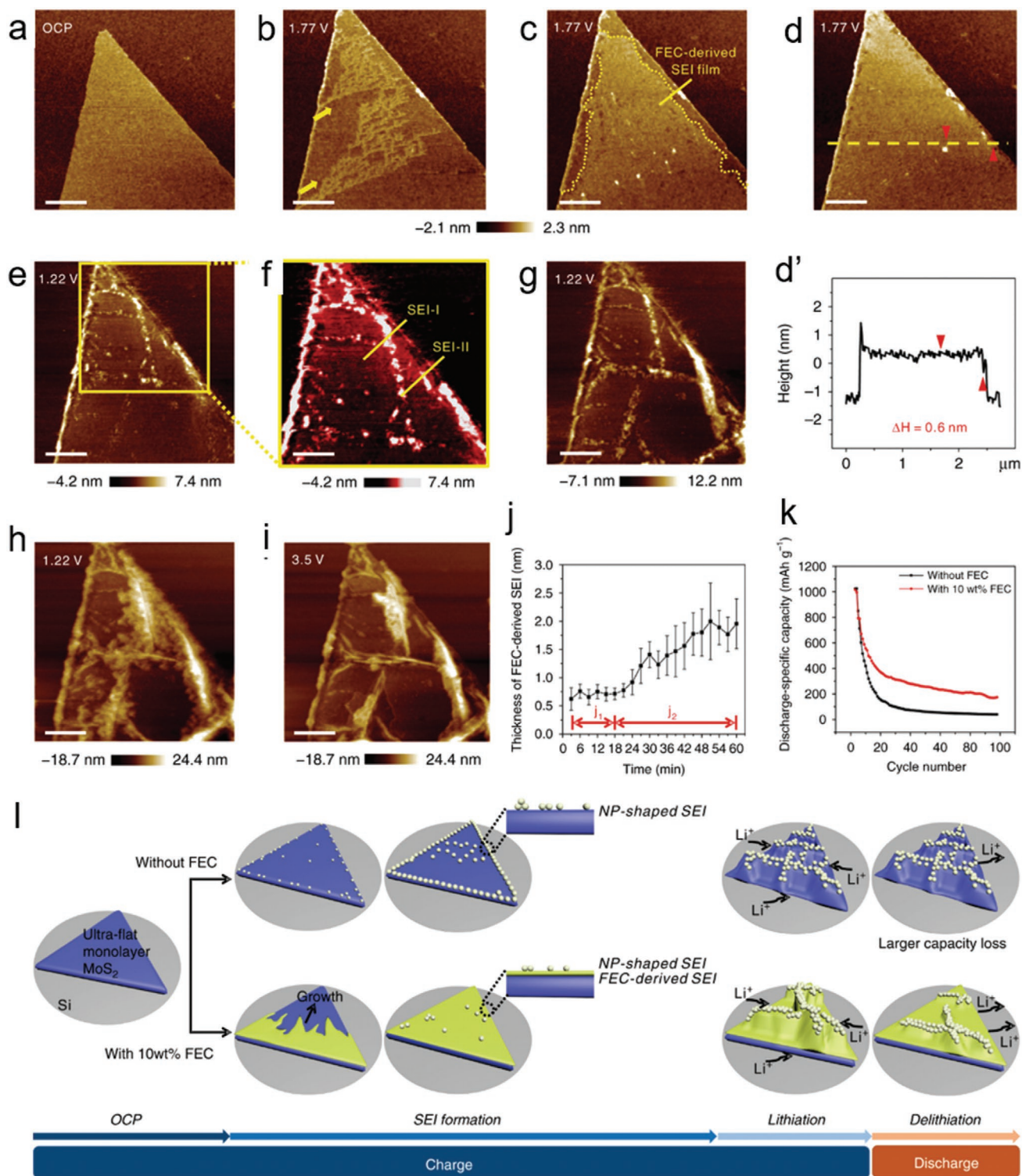


Figure 8. a–i) Quantitative insights of the in situ formation of ultra-thin FEC-derived SEI films on monolayer MoS₂ in [BMP]⁺[FSI]⁻ containing 0.5 M LiFSI electrolyte with 10 wt% FEC additive at different potentials. All scale bars are 600 nm. d') Line profile showing SEI film of 0.6 nm. j) Quantitatively measured thickness of FEC-derived SEI film upon charging. k) Cycling performance of Li/MoS₂ coin cells in FEC-free and FEC-containing electrolytes. l) Schematic illustration of the structural evolution and reaction mechanism of the monolayer MoS₂ electrode. Interphasial formation and lithiation/delithiation at the interface in FEC-free and FEC-containing systems. Reproduced with permission.^[207] Copyright 2019, Nature Publication Group.

Comparatively, these optical techniques provide in situ observation of the thickness (contrast) change of layered materials during reaction in a nondestructive way, while EC-AFM is

superior for in its ability to reveal detailed SEI layer characterization (including thickness changes), something that optical microscopy is blind to.

3.2. Cathode Materials

3.2.1. Li Transition Metal Oxide Cathodes: CEI, Surface Degradation, and Ion Diffusion

Transition metal oxides with a layered structure that allow Li ions to intercalate into the host network reversibly are the most common cathode types. LiFePO_4 , LiCoO_2 , $\text{LiNi}_x\text{Co}_y\text{Al}_z\text{O}_2$ (NCA) and $\text{LiNi}_x\text{Co}_y\text{Mn}_z\text{O}_2$ (NMC) are all widely studied and commercially available.^[213] Although the majority of EC-AFM battery papers to date focus on anode systems, the fast degradation of cathode materials is, in fact, a much more significant problem limiting the performance of LIBs.^[214] Hence, a wide variety of characterization techniques have been developed for investigating the degradation mechanisms of cathodes.

AFM has shown particular promise for the analysis of the structure and properties of cathode interfaces due to its ability to reveal nanoscale changes at a high resolution.^[215–218] For example, AFM has been utilized to reveal the coarsening and agglomeration of LiFePO_4 nanoparticles during aging in an electrolyte, which induces hardening and increased internal stress.^[219] The grain size change due to phase transformation during charge and discharge of LiFePO_4 particles has also been observed by EC-AFM.^[220]

Although most intercalation-type cathodes show only minor structural changes during intercalation/deintercalation of ions,^[221] Liu et al. have visualized the dimensional evolution of LiMn_2O_4 in aqueous electrolytes by in situ high-speed EC-AFM.^[222] Furthermore, they suggest that constructing ‘surface area-potential hysteresis loops’ (i.e., analysis of nanoparticle surface area as a function of potential) of individual LiMn_2O_4 nanoparticles at different sweep rates enables a quantitative method to study Li-ion diffusion kinetics within the materials.

LiCoO_2 cathode materials also only exhibit small dimensional changes upon cycling (<2%); nonetheless, they experience heavy mechanical damage after a small number of electrochemical cycles.^[223] Measurements of the Young’s modulus of LiCoO_2 particles before and after charging by an AFM nanoindentation technique have shown the modulus decreases from $\approx 70\text{--}80$ GPa to ≈ 40 GPa after delithiation, indicative of incomplete, or conversely, over-delithiation of the crystals, which may drive the fast degradation.^[224] Through the use of C-AFM to study the local Li-ion diffusion induced conductance change behavior (spatial resolution of ≈ 10 nm), it was found that the area near grain boundaries is more conductive than grain interiors under a certain bias voltage (Figure 9a–e).^[225] This is in agreement with first-principles calculations that suggest the LiCoO_2 grain boundary area has a lower Li-ion diffusion energy barrier and higher Li-ion diffusion rate. This inconsistent lithiation may also drive degradation. Nonetheless, this suggests that smaller LiCoO_2 grains have a lower threshold voltage to switch the grain to a conductive state, indicating that high-rate LIBs can be achieved by using nanostructured LiCoO_2 .

LiCoO_2 , like many other cathode materials, can form a cathode SEI, otherwise known as a cathode electrolyte interphase (CEI). This occurs at high potentials as electrolyte decomposition products deposit on the cathode surface. Understanding the structure and properties of this CEI is crucial for

high voltage performance of cathode materials. The morphological evolution of the CEI film at a LiCoO_2 surface, as studied via EC-AFM during electrochemical cycling, is presented in Figure 9g–i.^[226] The CEI film was found to only form at the edge plane of LiCoO_2 microcrystals, with no interfacial reactions appearing to occur at the basal plane due to the Li^+ intercalation/extraction activity in LiCoO_2 being highly dependent on crystal facet orientation. This CEI was found to exhibit a loose fibril structure under high voltage, whilst decomposing at lower voltages. This unstable CEI is incapable of limiting competing interfacial reactions. A thin layer of Al_2O_3 was demonstrated to completely suppress the formation of CEI at the edge plane, and significantly improve coin cell high voltage cycling stability. Facet-dependent CEI formation during charge-discharge processes has also been shown on $\text{LiNi}_{0.5}\text{Mn}_{1.5}\text{O}_4$ particle electrodes.^[227] A surface film with a thickness of 4–5 nm was formed on the (111) surface at ≈ 4.78 V which then stayed stable. No detectable CEI film growth was observed on the (100) surface during the first cycle.

Ni-rich NMC cathodes with a specific capacity of >200 mAh g^{-1} and high working potential of >3.8 V are attracting increasing attention.^[228] Their poor structural and interfacial stability, however, still hampers their large-scale application. While extensive investigations have been conducted by a variety of analysis methods, EC-AFM has been used to make important contributions to this area of study. In situ EC-AFM was employed to observe the dynamic evolution process of the CEI layer at the surface of $\text{LiNi}_{0.5}\text{Co}_{0.2}\text{Mn}_{0.3}\text{O}_2$ cathode particles in a solid-state LIB (poly(ether-acrylate) solid electrolyte).^[229] Combined with DMT modulus measurements, XPS, time-of-flight secondary ion mass spectrometry and EIS analysis, it was discovered that LiF-rich species first form at 4.08 V on charge, followed by the formation of organic species such as ROLi and ROCO_2Li ; subsequently, inorganic components of Li_2CO_3 and LiF formed at 3.4 V on discharge, which was confirmed by the real-time DMT modulus change (Figure 10a–i). In addition, in situ EC-AFM was also capable of observing the planar gliding and microcracking of a single-crystal $\text{LiNi}_{0.76}\text{Mn}_{0.14}\text{Co}_{0.1}\text{O}_2$ cathode.^[230] As shown in Figure 10j–m, the different regions, as marked by B and C, of a ≈ 3 μm -sized single crystal display nanosized crack domains and lattice-invariant shear (planar gliding) during charging to 4.50 V, respectively. These deformations of the NMC crystal were demonstrated to be reversible during discharging. The in situ EC-AFM observation using micron-sized single crystals provides a clear platform for the investigation of mechanical degradation of NMC materials, which correlates well with data from scanning transmission electron microscopy (STEM).^[230]

SSRM with a logarithmic current amplifier was utilized to study the evolution of electrical conductivity of NMC cathodes.^[231] A remarkable reduction in electronic conductivity in the core region, rather than on the surface of secondary particles, was detected, causing capacity fading. Li intercalation-deintercalation was not achievable in the electronically insulated primary particles at the core region of NMC particles. After 300 charge/discharge cycles, the overall electrical resistance of the secondary particles substantially increased, accompanied by the formation of microcracks.^[232] These results suggested that grain boundary engineering in secondary particles should be

effective in improving the electrochemical properties of NMC cathodes.

EC-AFM has also been utilized to study promising next-generation layered metal oxide cathodes. Vanadium oxides are one such group due to a high theoretical capacity of 450 mAh g^{-1} in the 3.5–1.5 V potential range.^[233] However, like other cathodes, they suffer from capacity fading during electrochemical cycling; this has been studied by in situ EC-AFM, showing both morphological and interphase layer change. Swiatowska-Mrowiecka et al. have shown a reversible grain size variation during Li-ion insertion/de-insertion into V_2O_5 thin films, enabling distinction of the $\epsilon\text{-Li}_{0.5}\text{V}_2\text{O}_5$ and the $\delta\text{-Li}_1\text{V}_2\text{O}_5$ phases via the degree of volume expansion observed.^[234] It has also

been shown ex situ via AFM and XPS that an SEI-like thin film forms on the surface of a V_2O_5 cathode after the first discharge, which thickens in the following cycles.^[235] In situ AFM has shown that LiClO_4 salt in the electrolyte suppressed the excessive formation of the surface film, when compared to LiPF_6 .^[236] These works highlight the fact that EC-AFM can be a powerful tool to understand and inform the development of new battery electrode materials and their electrolyte systems.

EC-AFM shows advantages for the in situ characterization of the cathode/electrolyte interface, providing high resolution morphological, mechanical, and electrical images, in a large range of length scales, from nanometers (primary particle) to tens of micrometers (secondary particle). Unfortunately,

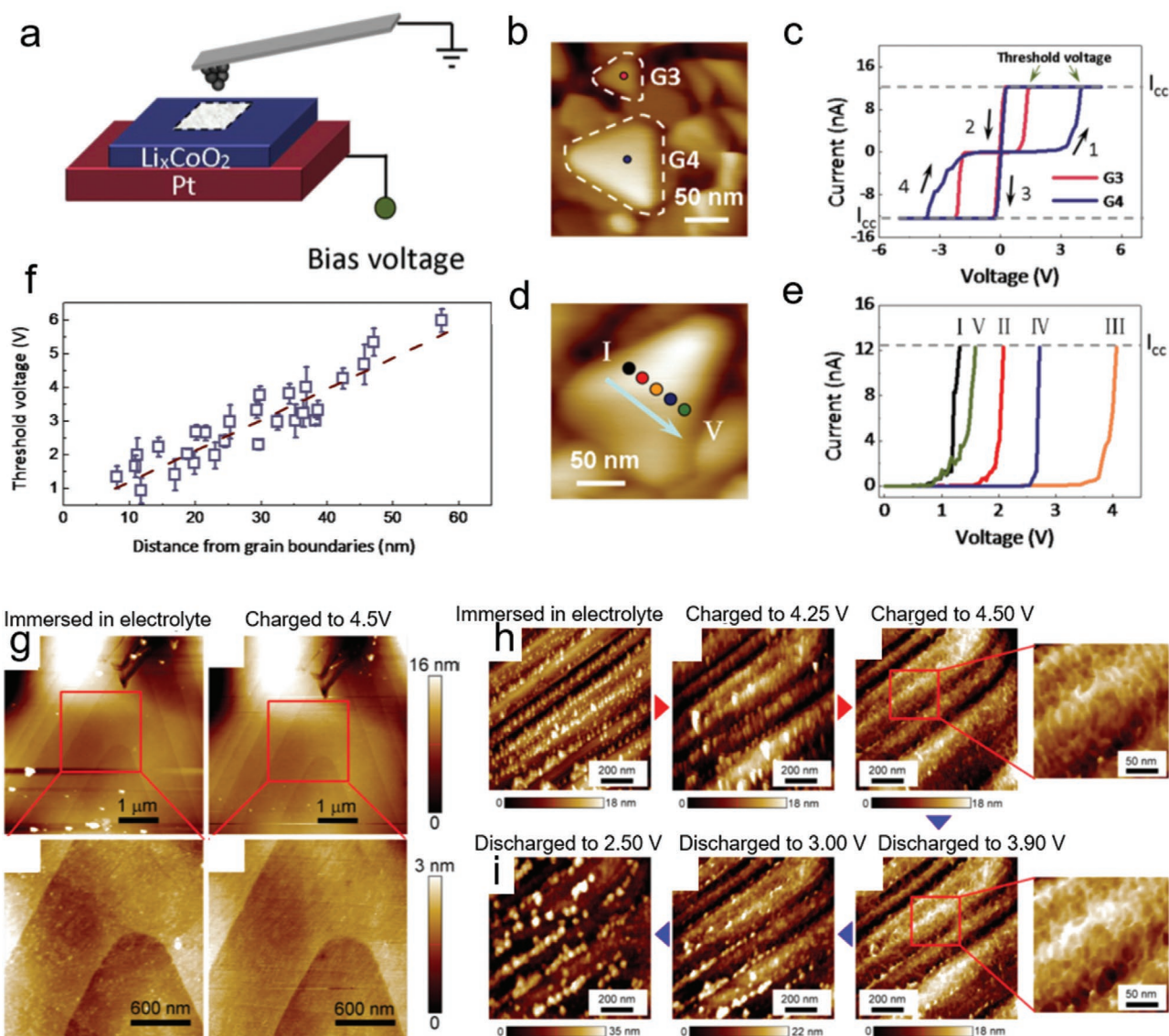


Figure 9. a) Schematic of the experimental setup for C-AFM measurements of LiCoO_2 films. b) Small area morphology of the LiCoO_2 and c) corresponding I - V curves showing different conductance change behaviors of two grains with different size. d) Morphology of an LiCoO_2 grain and e) corresponding I - V curves at different positions away from its grain boundaries. f) Location dependence of the threshold voltage obtained from various grains. Reproduced with permission.^[225] Copyright 2013, Nature Publication Group. g) Morphology of the basal plane: before and after charging to 4.5 V. h) In situ AFM imaging of the CEI film formation and decomposition on the edge plane of LiCoO_2 crystal: immersed in electrolyte, charged to 4.25 and 4.5 V. i) Discharged to 3.9, 3.0, and 2.5 V. Reproduced with permission.^[226] Copyright 2017, American Chemical Society.

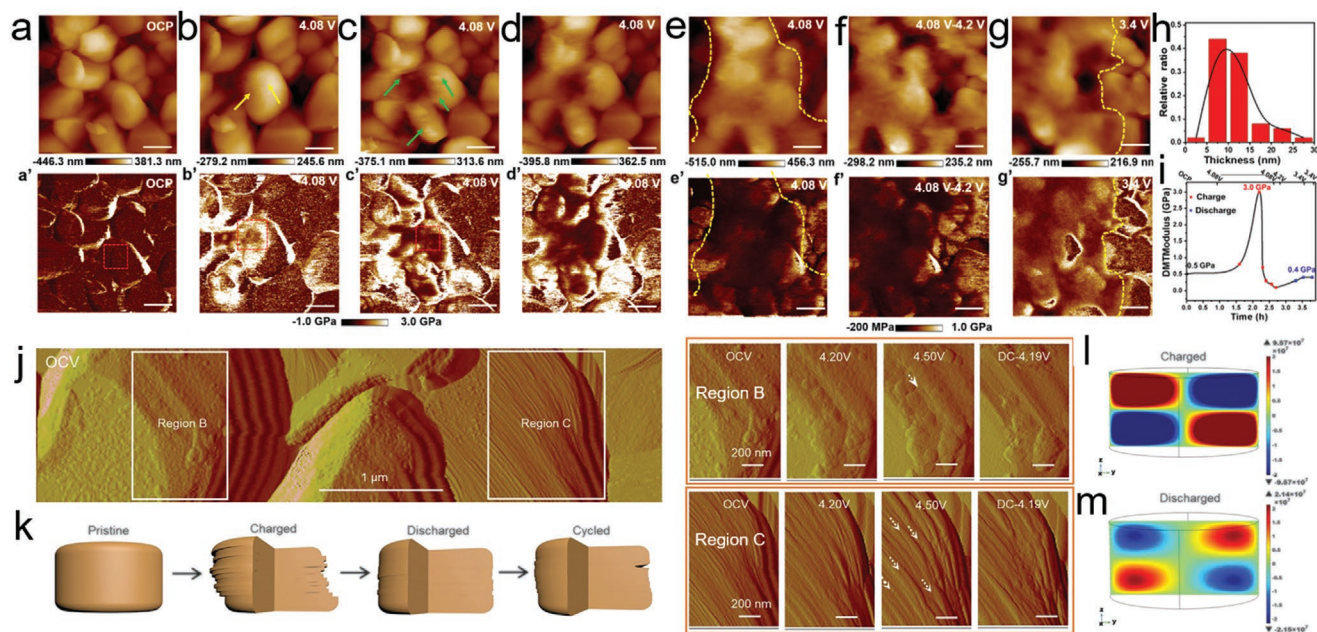


Figure 10. In situ EC-AFM images showing the topography a–g) and DMT modulus mapping a’–g’) of NMC electrode surfaces during charge and discharge. The scale bars are 500 nm. h) The Gauss statistic distribution histograms of film thickness. i) Quantitatively measured average DMT modulus of the red frame during charge/discharge. Reproduced with permission.^[229] Copyright 2020, American Chemical Society. j) AFM images at the OCV state of NMC single crystal surface, and the morphology evolution during charge/discharge in the selected regions B and C. k) Schematic illustration of the structural evolution of the single crystal NMC upon cycling. l,m) COMSOL-simulated shear stress along the yz direction during charge (delithiation) and discharge (lithiation) at scale time of 0.1T, respectively. Reproduced with permission.^[230] Copyright 2020, the American Association for the Advancement of Science.

EC-AFM is unable to detect the bulk structure degradation and chemical property evolution in a buried battery environment.

Although it is clear that interfacial processes at layered metal oxide cathodes are important in defining their electrochemical performance, commercial active cathode materials commonly consist of $\approx 5\text{--}10\ \mu\text{m}$ particles held within a carbon matrix.^[237] With particles of this size and morphology, their bulk properties are also a major factor in defining their behavior, such as irreversible capacity fade (decreased Coulombic efficiency) and voltage loss (increased cell impedance). The causes of bulk degradation of cathode materials include micro-cracking, structural disordering, dissolution and migration of soluble species, gas evolution, loss of contact, and more. For characterizing these phenomena, synchrotron or laboratory ex situ/in situ/operando X-ray CT has been developed, providing 3D or 4D imaging of electrode particles and tracking relevant degradation mechanisms.^[238,239] With resolution capabilities spanning tens of microns to tens of nanometers, X-ray CT is excellent for characterizing micro-cracking and structural disordering of secondary particles.^[240,241] The multiple modes of absorption, phase-contrast, diffraction, and fluorescence, offering unique information capable of building a more complete description of the structure, composition, strain, and stress of electrode materials.^[242] Moreover, Bragg coherent diffraction imaging (BCDI) is an advanced X-ray imaging technique, which provides the crystal morphology and phase information (spatial resolution of down to 10–20 nm), corresponding to the projection of the lattice distortions within the crystal (picometer level resolution);^[243] though for the high resolution studies synchrotron

X-rays are necessary. X-ray CT importantly, and rarely, provides an opportunity to study battery materials in a ‘real’ environment, as they can stay within commercial or home-made cells during in situ characterization. However, the spatial resolution is significantly lower than that achievable with EC-AFM and low Z materials, for example, Li, C, and interfacial structures are very difficult or impossible to visualize, especially when information of the fine structure of materials is required (e.g., CEI layer).

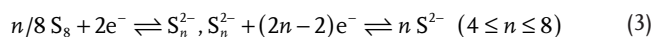
⁷Li nuclear magnetic resonance (NMR) is another non-invasive, non-destructive technique that can provide information on Li-ion local environment and dynamics in layered oxide cathodes due to its sensitivity to the Li chemical shift, especially in the presence of surrounding paramagnetic transition metal ions. Thus, redox changes to the surrounding coordinated transition metal ions lead to observable chemical shifts. NMR is well suited to the study of full (although specially designed) cells, revealing the different environments and dynamics in both the graphite anode and metal oxide cathode within a full cell in operando.^[244] For example, the dynamics at different SoCs of NMC cathodes have been studied by solid-state NMR and XRD, which provides insight into the evolution of crystal lattice and lattice strain during battery charge/discharge.^[245,246] In addition, combined with magnetic resonance imaging, NMR is very effective in monitoring the in situ structural and quantitative changes under realistic cell conditions. However, it is a challenge to separate the resonance from different battery components (electrode, electrolyte, interface) as ⁷Li is used as the probe nucleus.^[8] NMR therefore is another technique that

provides information that is averaged over the whole sample. Nonetheless, if combined with in situ SPM techniques that can reveal specific localized detail, such as AFM, extensive mechanistic detail can be revealed.

3.2.2. Lithium–Sulfur and Lithium–Air Battery

Cathodes: Detection of Intermediates

Sulfur offers exciting possibilities as a cathode in lithium-based batteries due to its significantly greater theoretical specific capacity compared to metal oxides (1675 mAh g⁻¹ vs 280 mAh g⁻¹ for LiNi_{0.33}Mn_{0.33}Co_{0.33}O₂).^[247] However, lithium-sulfur batteries are hindered by problems related to the low conductivity of sulfur, cathode volume expansion, and capacity loss due to the ‘shuttle effect’ originating from soluble lithium polysulfides (LiPS). The electrochemical reaction:



is a multistep redox process which produces these LiPS intermediates. They are soluble in most useful battery electrolytes, which allows them to diffuse to the anode where they can be oxidized, leading to irreversible capacity loss and hampering battery performance.^[248] Direct characterization of the deposition and dissolution of intermediate lithium sulfides at the nanoscale is important for an in-depth understanding of the electrochemical mechanisms. However, this is very difficult to achieve due to the delicate structure and properties of these intermediate species. EC-AFM can provide in situ/operando observation of the products at the electrode–electrolyte interface with a high spatial resolution.

The dynamic nucleation, growth, deposition, and dissolution processes of insoluble Li₂S₂ and Li₂S on HOPG substrate were observed by Lang et al. (Figure 11).^[249] The carbon elec-

trode was cycled in a catholyte containing Li₂S₈ with LiTFSI in 1,3-dioxolane/ 1,2-dimethoxyethane (DOL/DME). Once a reduction potential was reached, Li₂S₂ nanoparticles were observed to deposit first, before sediments of lamellar Li₂S appeared. During oxidation, Li₂S decomposed while the Li₂S₂ is oxidized incompletely, accumulating over the following cycles. The irreversible deposition of Li₂S₂ was suggested to indicate a mechanism for capacity fading in Li-S batteries, which was confirmed by EIS. It was also demonstrated that the insulating Li₂S lamellar structures undergo preferred deposition at higher current densities, which inhibits subsequent reactions at the interface. Later, these authors showed that electrolytes containing LiFSI help form an LiF-containing film that can both physically confine and chemically anchor the LiPS intermediates, which facilitates Li₂S and Li₂S₂ redox reactions.^[250] By comparing the same process at room temperature and 60 °C, it was verified that elevated temperatures help maintain a better functional film that retards side reactions and facilitates interfacial reversible LiPS redox reactions.

C-AFM can also be used to measure the evolution of sulfur cathodes. A PtIr coated Si cantilever was designed to acquire conductivity maps corresponding to the topography of a composite sulfur cathode.^[251] It was demonstrated that as charge/discharge cycles progress, battery capacity reduces, surface morphology becomes smoother, and the average surface conductive area decreases due to the formation and dissolution of LiPS. These studies provide direct information on the nanoscopic structure and support for the modification and optimization of Li–S batteries.

As previously discussed EC-AFM can directly reveal the formation of LiPS species and reversible dissolution of Li₂S. However, although they play a role, other intermediates are soluble in the electrolyte and therefore undetectable by this method. By employing advanced AFM-scanning electrochemical microscopy (AFM-SECM), Li-S interfacial redox reactions have been revealed in real-time at a nanoscale spatial resolution. This

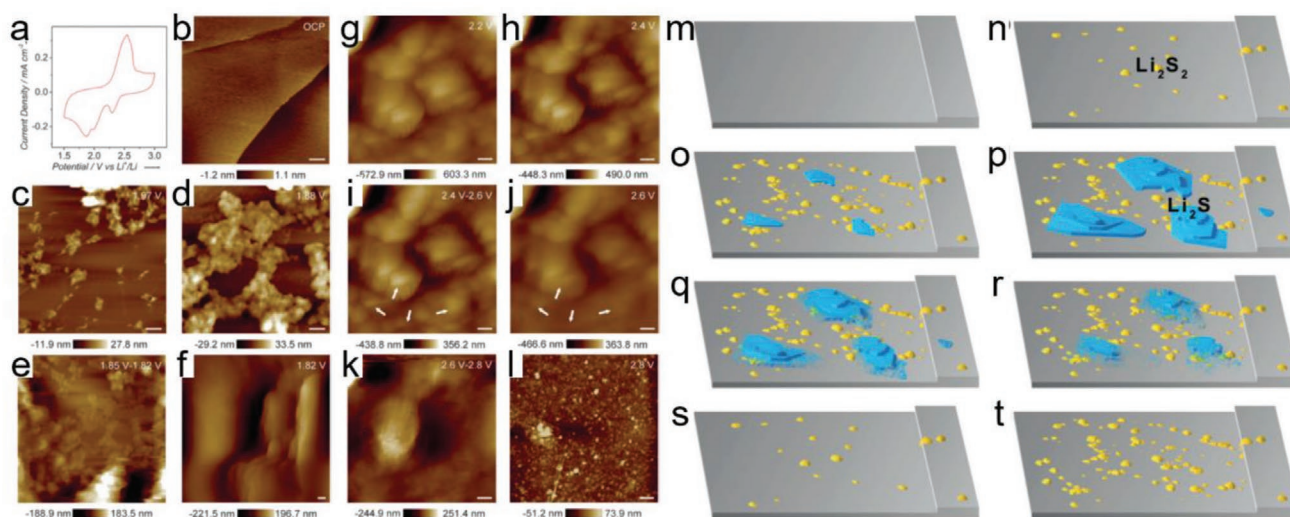
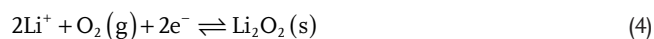


Figure 11. a) Representative CV curve of the first cycle in a Li/LiPS cell, and AFM topography images of Li polysulfides LiPS deposition at different potentials, b–f) show reduction (scale bars are 100 nm) and g–l) oxidation (scale bars are 1 μm). m–t) Schematic of interfacial processes upon the discharge/charge cycling. Reproduced with permission.^[249] Copyright 2016, Wiley-VCH.

shows the potential ability of advanced AFM techniques.^[252] AFM-SECM images of $\text{Li}_2\text{S}/\text{Li}_2\text{S}_2$ particles revealed both electrochemically active (conducting) and inactive (insulating) features within the species. During charging, the conducting phase is reversible and undergoes further conversion reactions, while the insulating part (Li_2S) is irreversible and tends to react with intermediate LiPS. At higher oxidation potentials, an increased quantity of insulating Li_2S products accumulated, leading to capacity fade. This agrees with the results obtained using in situ EC-AFM, revealing the practical chemical reactions that occur in a realistic battery, despite the different cell configuration.

The true nature of LiPS at the electrode—electrolyte interface is difficult to explore due to the complicated phase transformations taking place during charge/discharge and the limitations associated with the interfacial nature of AFM characterization.^[253] Designing optimal conditions for Li–S battery commercialization is not possible without a nanoscale understanding of the parasitic reactions and SEI layer evolution. A variety of in situ X-ray related spectroscopy and microscopy techniques have been developed to reveal the existence of LiPS intermediates and structural change of sulfur particles. For instance; 1) in situ XPS has been combined with ab initio molecular dynamics (AIMD) computational modelling, which was capable of spatially resolving chemical species. This has revealed the distinct roles of SEI evolution during cycling, giving insight that is not possible by EC-AFM alone.^[254] 2) X-ray absorption spectroscopy (XAS) can reveal the existence of Li_2S_2 and Li_2S intermediates, and spatially resolved SoC of LiS.^[255,256] 3) In situ and operando XRD is able to detect some of the intermediate sulfur phases during the redox process.^[257] However, these methods are unable to detect all species and morphological changes associated with the SEI, thereby significantly limiting the field of view with respect to all parasitic reactions taking place. 4) In situ transmission X-ray microscopy^[258] and 5) X-ray fluorescence microscopy (XRF)^[259] have also been used to observe the spatial changes of sulfur particles. However, these hypotheses only give indirect evidence of lithiation and dissolution of LiPS species. In addition, these techniques require specially designed cells, which often diverge greatly from ‘real’ battery conditions.

Like the Li–S system, non-aqueous Li– O_2 batteries offer great advantages over the current generation of batteries, including a theoretical specific energy density ($\approx 3 \text{ kWh kg}^{-1}$). Unfortunately, another similarity is that they still need to overcome significant obstacles, including poor cycling stability and huge cathodic polarization, before they can be widely deployed.^[260] Key to the function of Li– O_2 batteries is the electrochemical reaction:



But this is not usually the only reaction occurring in the Li– O_2 cell, as it is accompanied by parasitic side reactions resulting from the instability of the non-aqueous electrolytes and lithium salt. Visualization of the oxygen reduction reaction (ORR)/oxygen evolution reaction (OER) activation process at the triple-phase boundary (catalyst/electrolyte/gas molecules) enables the investigation of the correlation between product morphology and chemical species during the Li– O_2 reaction.^[261,262] In situ EC-AFM has been employed to observe the morphology of Li_2O_2 films on HOPG, glassy carbon and nanoporous gold

substrates during the ORR and OER.^[263–265] The ORR products were directly observed by in situ EC-AFM to be fully decomposed at a high potential of 4.4 V (vs Li^+/Li) in the subsequent OER process.^[266] Moreover, accurate potentials of the electrochemical reactions were confirmed by combining the results of in situ microscopy (EC-AFM) and spectroscopy (such as infrared absorption and surface-enhanced Raman spectroscopy (SERS) measurements). In addition, the nanostructure of the gold electrode was found to impact the morphology of the Li_2O_2 produced.^[267] In situ EC-AFM is therefore ideal for directly observing the electrochemically induced reaction intermediates with a nanoscale resolution, which is of great significance for a deep understanding of the catalytic mechanism of electrodes in this case.

3.3. Electrolyte Materials

Commonly used liquid electrolytes in commercial LIBs are a mixture of cyclic and linear carbonates with a lithium salt, for example, EC/DMC/LiPF₆. Although these organic electrolytes have some advantages, such as high ionic conductivities and a good SEI forming ability, they suffer from significant drawbacks, particularly in terms of chemical stability, overall safety, and environmental friendliness. To address these issues, alternative electrolytes such as ionic liquids, inorganic, polymer, and hybrid composition electrolytes have been developed. The following section provides a survey of the AFM-based research on these novel electrolyte materials.

3.3.1. Ionic Liquid Electrolytes: Electrical Double-Layer Structure

Ionic liquids, pure salts in a liquid state at ambient temperature, are attractive electrolyte solvents for LIBs due to their large electrochemical windows, high thermal and chemical stability, low vapor pressure and flammability, and inherently high ionic conductivity.^[268] However, understanding the performance of these electrolytes has challenges, including the fact that the standard electrical double-layer (EDL) models of liquid electrolyte–electrode interfaces are not suitable for explaining their behavior.^[269–271] Hence, it is necessary to investigate the interfacial morphology and electrode surface properties of electrodes in ionic liquid-based LIBs. AFM is well suited to this task, enabling the determination of the nanostructure of the ionic liquid EDL with molecular resolution and the study of the interfacial dynamics between the electrode surface and ionic liquid.^[272,273]

In situ amplitude-modulated AFM, measuring the tip-sample distance by the actual value of the oscillation amplitude in a non-contact mode, has shown the interfacial nanostructure of an ionic liquid electrolyte on a HOPG electrode at different potentials.^[274] A well-formed Stern layer (the compact inner structure of the EDL) is thought to be produced on the solid surface in ionic liquids due to increased ordering of ions. Applying a surface potential induces a reordering of the normal Stern layer structure to compensate for the interfacial charge. This Stern layer structure was observed by AFM between $\pm 1 \text{ V}$ in a 1-ethyl-3-methylimidazolium bis(trifluoromethylsulfonyl)imide

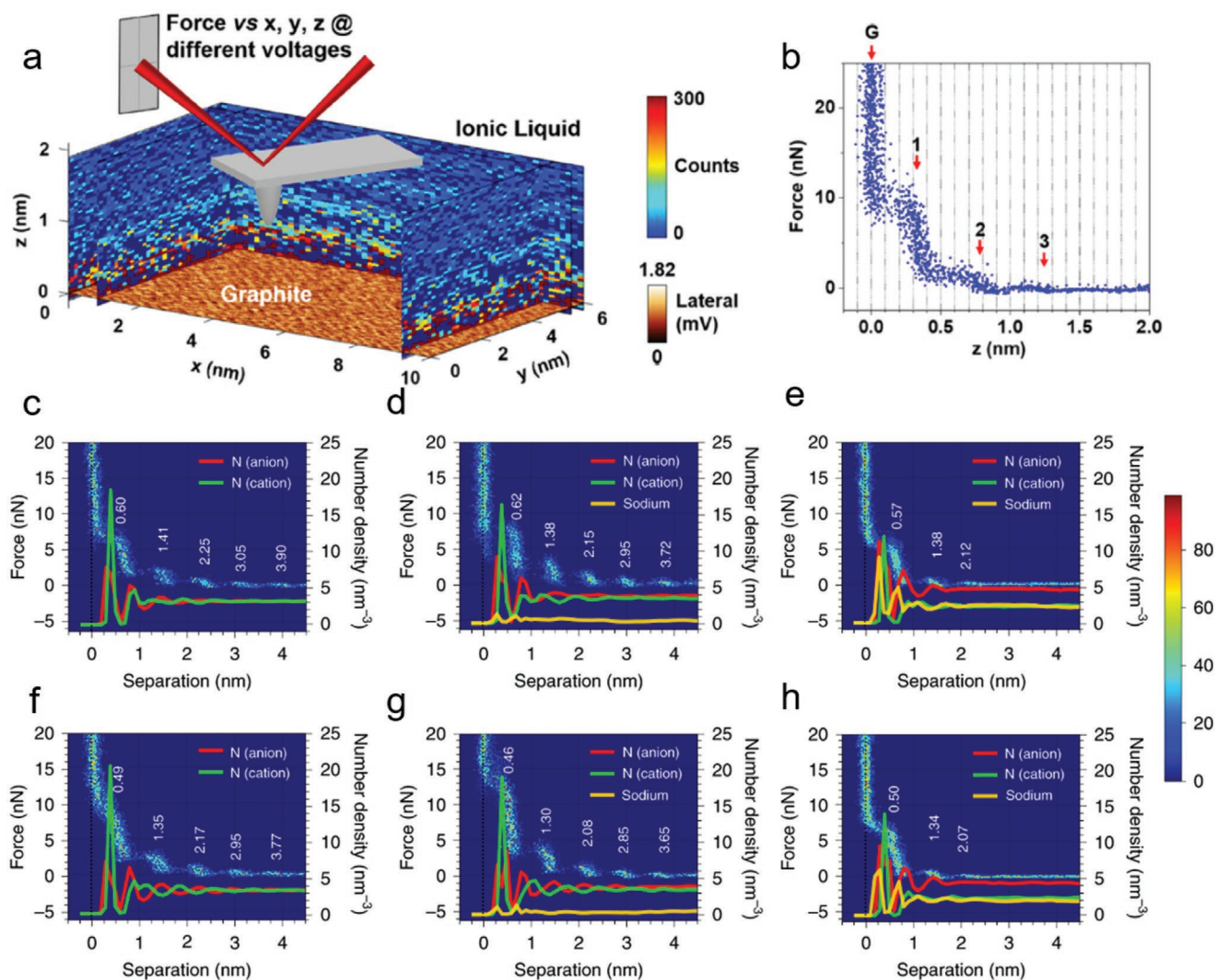


Figure 12. a) 3D image of the electrode-electrolyte interface of HOPG surface revealing the EDL in an ionic liquid electrolyte. b) Series of 50 force-distance curves, red arrows mark the position of the three EDL layers. Reproduced with permission.^[275] Copyright 2020, American Chemical Society. c–h) AFM force-distance 2D histograms with probability color bar on the right-hand side and ion number density profiles of $[FSI]^-$ (red curve), $[C3mpyr]^+$ (green curve), and Na^+ (yellow curve) from MD simulations. AFM histograms, (c–e) are obtained at OCP, and (f–h) at OCP-0.5V. MD profiles, (c–e) are obtained at the PZC while (f–h) at -0.5V versus PZC. C3mpyrFSI ionic liquid with different NaFSI salt concentrations of 0 mol% (c, f), 10 mol% (d, g), and 50 mol% (e, h) are also compared. Reproduced with permission.^[277] Copyright 2020, Nature Publication Group.

$([EMIm]^+ [TFSI]^-)$ ionic liquid, with $Li[TFSI]^-$ or $Li[EMIm]^+ Cl$ additives.

Based on sensitive force detection, EC-AFM can be used to measure the 3D EDL structures by performing force–distance curves (Figure 12a,b).^[275] In ionic liquids this technique has been used to demonstrate that the EDL contains multiple discrete ionic layers with a quasi-periodic molecular density distribution, which is dependent on the potential of the graphite electrode in the electrochemical cell. The dimension of the steps in the force–distance profiles provides an indication of the composition of the solvent layers. This unique feature of AFM experiments enables the analysis of the layered electrolyte structure in ionic liquids near the surface of the electrode.^[276] The force–distance spectroscopy obtained by the AFM probe shows a series of steps at discrete separations within 4.5 nm

of the electrode, with each step corresponding to an interfacial ion or ion pair layer (Figure 12c–h). The peaks observed qualitatively correlate with those predicted using molecular dynamics (MD) simulations, although direct comparison is complicated by the fact that the calculations were based on potentials from the point of zero charge (PZC), whereas the experimental data was collected at potentials based on the open circuit potential (OCP). Alternatively, due to the special structure of the EDL on electrode surface, super concentrated (e.g., 1:1 ionic liquid: alkali ion) ionic liquid electrolytes were demonstrated to enable uniform metal deposition and prevent Li/Na dendrite growth for Li/Na metal anodes, when combined with anode preconditioning at more negative potentials.^[277]

The EDL at the electrode–electrolyte interface is thin and delicate, hence the interaction between tip and EDL must be

considered. Generally, AFM force curves can be obtained while imaging, providing both mechanical properties and topography imaging. However, for a precise measurement of the EDL structure, the force—distance curves in these papers are acquired by ramping the AFM tip slowly onto a relatively small area (smaller than that shown in topography images), for example Begic et al. used a 2 Hz ramp rate in a 30–50 nm² area,^[276] whereas Zhou et al. used a smaller 10 × 10 nm zone.^[275] Therefore, the slow data generation is compensated for by the small image size, meaning they can be collected in reasonable timeframes. Intermittent contact modes are used to minimize surface disruption/damage and since alignment of the anions and cations near the surface is driven by the applied potential,^[274] forming a 3D EDL structure at the electrode surface, any disruption caused by the tip is restored immediately after the retraction of the probe.

An SEI layer can still form in ionic liquids, as shown by combined AFM and MD simulations which have revealed the SEI layer on a Na metal anode surface. In a C3mpyrFSI ionic liquid electrolyte with different concentrations of NaFSI salt, the steps of AFM force—distance profiles on electrodes at different potentials were used to determine the mechanical strength of the layering structure of the SEI. Similar to that in standard organic electrolytes, SEI film formation was also observed in the ionic liquid-based electrolytes with LiFSI + [BMP]⁺ [FSI]⁻, LiFSI + [BMP]⁺ [TFSI]⁻, and LiTFSI + [BMP]⁺ [TFSI]⁻ with HOPG substrate by in situ AFM.^[278] The first lithiation process was shown to follow two steps of initial SEI formation and subsequent intercalation of Li ions, which exhibit different phenomena at the basal and edge planes. Topographic analysis by in situ AFM revealed that [FSI]⁻ anions beneficially formed a uniform and stable SEI film, which promoted Li-ion conductivity and prevented [BMP]⁺ cation intercalation.

For the in situ investigation of electrode—electrolyte interface, EC-AFM has shown the ability to investigate the EDL structure of the ionic liquid electrolyte, which cannot be achieved with other techniques. Whilst this is a relatively novel area of research, many more related investigations by the use of EC-AFM will likely fill the gaps in our understanding soon, such as analyzing the chemical composition and mechanical properties of SEI layer formed in an ionic liquid electrolyte, which will provide a deeper understanding of the mechanisms and improve the battery design of this type of electrolyte.

3.3.2. Solid-State Electrolyte: Solid–Solid Interfacial Characterization

LIBs with SSEs possess the merits of safety (as they can be dendrite-suppressing and non-flammable), environmental benignity and suitability for high energy density devices (in ultrathin batteries).^[279] To date, two major types of SSEs have been developed, namely, inorganic ceramic or glass materials (such as garnet type, thio-LISICON type) and organic polymer materials (polymer with dissolved lithium salt). Both exhibit a wide electrochemical stability window and excellent lithium metal compatibility.^[280,281] Generally, inorganic ceramic SSEs have higher ionic conductivity but an unstable interface and weak contact with electrodes, while polymer electrolytes

show good stability and better electrode—electrolyte contact, but lower conductivity and mechanical strength.^[282] This is important as it is commonly accepted that a high mechanical strength electrolyte can physically suppress the Li dendrite growth in solid-state LIBs.^[283,284] However, research also suggests that dendrite formation still happens inside SSE materials due to high local electronic conductivity (derived from impurities, defects, grain boundaries, or electrochemical reductions).^[285] The formation and growth of dendrites is also considered to originate directly from non-equilibrium or uneven ion transport, together with electronic transport to balance the charge or reduce the Li ions.^[286] Therefore, studying the micro/nanoscale mechanisms including ionic diffusion, charge and vacancy trapping, local phase transformation, and electrode—electrolyte interfacial phenomena are important for developing commercially viable solid-state LIBs.

Engineering the interfacial structures and properties between electrode and electrolyte, for improved smoothness, mechanical strength, electrical contact, and compatibility, are the most extensively studied areas of research into SSEs. EC-AFM/C-AFM, with their ability to visualize mechanical and electrical/electrochemical phenomena, are valuable tools here.

Uniform lithium plating between the electrode and SSE is vital for the stable cycling of solid-state batteries. Liu et al. demonstrated that if a self-healing, flame retardant polymer electrolyte layer, which had high ionic conductivity and good interfacial compatibility, was introduced between a NASICON-type Li_{1.5}Al_{0.5}Ge_{1.5}P₃O₁₂ (LAGP) ceramic electrolyte and electrodes, it would improve cycling performance due to inhibited Li dendrite growth.^[287] Ex situ AFM mechanical measurements demonstrated that after ten stripping/plating cycles a smooth and robust SEI layer formed between the Li metal electrode and polymer-modified LAGP SSE (Figure 13a,b). The enhanced SEI layer induced more homogeneous Li stripping/plating than that of LAGP SSE without polymer coating. Similarly, AFM in PeakForce Tunnelling mode showed that an intermediary Mg₃N₂ layer between Li metal anode and PEO SSE enabled a smoother, more robust surface with a more homogeneous current distribution on the Li anode surface (Figure 13c–f).^[288] This facilitated homogeneous Li plating/stripping and promoted fast Li ion kinetics.

Apart from introducing a hetero interlayer, an alloy-type layer or anode material instead of pristine Li have demonstrated a more stable interface between the anode and SSE. For instance, an artificial interlayer (alloy metal layer of Au or Ag) has been introduced between a Li metal anode and a garnet-type Li₇La₃Zr₂O₁₂ (LLZO) for better lithium redistribution and precipitation.^[289] AFM images of the Ag and Au interlayers after plating and stripping at different charge/discharge current densities are compared in Figure 12g,h. The Ag interlayer showed lower roughness than Au, indicating better plating and stripping kinetics are achieved by Ag interlayer modification. Dynamic visualization of the Li deposition/dissolution was achieved by in situ EC-AFM, via monitoring of the lateral interface between Li–In alloy anode and Li₁₀GeP₂S₁₂ (LGPS) SSE.^[290] The Li–In alloy anode with a high ionic diffusion coefficient and low ionic migration barrier induces the homogeneous formation of an SEI and 2D uniform growth of Li_xIn lamellae upon lithiation. The on-site tracking of the morphological evolution

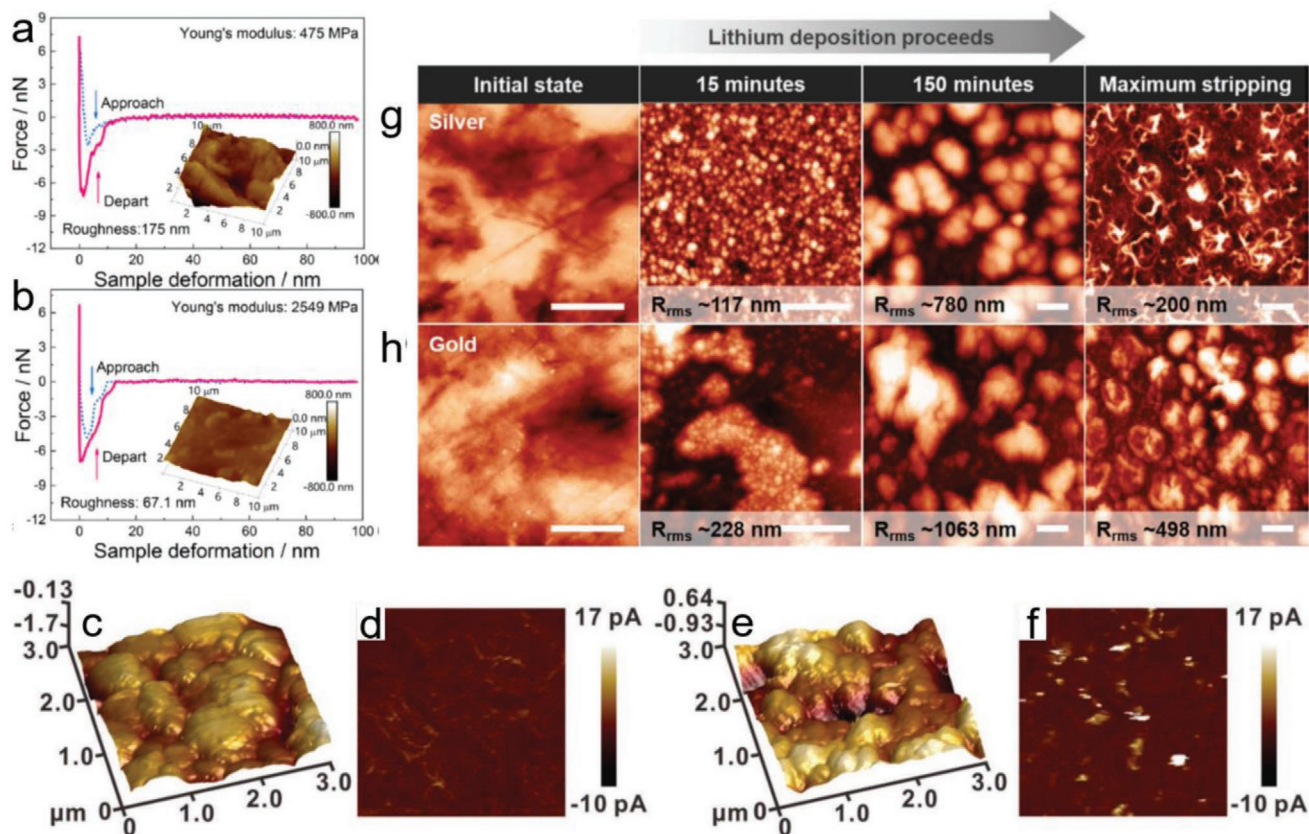


Figure 13. Force-displacement plots and 3D AFM images of a) LAGP-derived SEI and b) self-healing polymer electrolyte-derived SEI. Reproduced with permission.^[287] Copyright 2020, American Chemical Society. AFM 3D topography and current distribution images after five cycles with c,d) PEO-Mg₃N₂ and e,f) PEO electrolytes. Reproduced with permission.^[288] Copyright 2020, Wiley-VCH. AFM images of the surface of g) silver and h) gold interlayers at various charge/discharge states: pristine, after 0.2 mA cm⁻² galvanostatic deposition for 15 and 150 min, and 0.1 mA cm⁻² galvanostatic stripping of lithium. Scale bars are 10 μm. Reproduced with permission.^[289] Copyright 2020, Wiley-VCH.

and dynamic mechanism in these studies provides an in-depth understanding of the electrode/SSE interfaces.

Direct correlation of local conductivity and topographical features of SSEs are very helpful in designing more reliable high energy density batteries when utilizing SSEs.^[291] Intermittent contact alternating current scanning electrochemical microscopy (ic-ac-SECM) demonstrated its effectiveness in measuring the ionic conductivity while obtaining the local topographic images of SSE.^[292] **Figure 14a,b** show the topographic and impedance maps obtained at a large LLZO grain using ic-ac-SECM over 250 × 250 μm. The grain is surrounded by boundaries of higher impedance. However, after the cell was short-circuited a higher current was measured along the grain boundaries than grains in Ta-doped LLZO (LLZTO), as measured by ex situ C-AFM, indicating that Li metal propagates along grain boundaries.^[293] With a biased probe scanning the sample surface, AFM was also used to investigate the nanoscale inhomogeneity of ionic and electronic transport in Li₃PS₄ and its Li₃PS₄/polymer electrolytes.^[294] The local ionic conductivity was found to differ by one to two orders-of-magnitude across the Li₃PS₄ SSE. The ionic conductivity mapping indicated a sharp transition of ion transport at the boundary of polyimide/Li₃PS₄ grains due to different grain orientations in the polycrystalline and glass ceramic materials

(Figure 14c–e). However, the extension of polyimide into inter-particles between the Li₃PS₄ grains during the electrochemical cycling effectively mitigated dendrite growth.

In situ C-AFM has also been employed to induce Li-ion diffusion within an all-solid-state thin-film battery, while monitoring the cycling induced changes of topography, phase and volume of the anode thin film.^[295] The all-solid-state thin-film LIB consisted of a TiO₂ anode, LiPON (amorphous Li_xPO_yN_z, where $x = 2y + 3z - 5$) electrolyte, and an LiNi_{1/3}Co_{1/3}Mn_{1/3}O₂ cathode. As shown in Figure 14f–m, reversible changes of topography and phase of the polycrystalline TiO₂ anode surface were observed as the local bias-induced electric field was cycled. The cyclic expansion/contraction behavior from topography was attributed to the reversible movement of Li ions between electrode and electrolyte; the phase images indicated the cyclic chemical composition evolution, both providing new insight into the mechanisms of the ionic transport in all-solid-state LIBs.

One of the most important issues hampering the applications of SSEs is their poor solid–solid interface contact between electrodes and SSE compared to liquid electrolytes, leading to interfacial problems such as low mechanical strength, high resistance, and weak electrochemical compatibility and dendrite growth.^[296] However, the characterization of the solid–solid interface is difficult given its buried, sensitive,

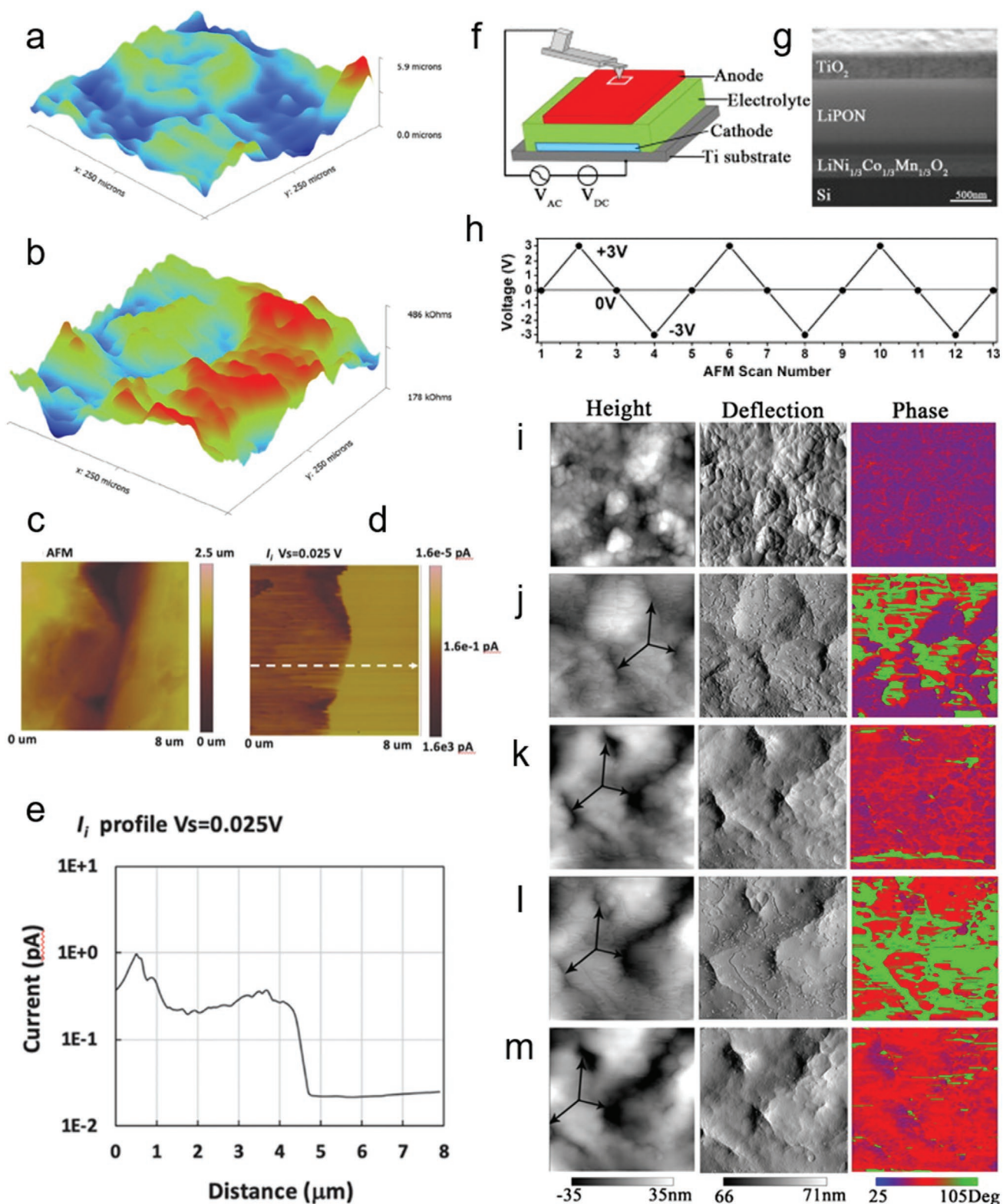


Figure 14. a) Topographic and b) impedance maps obtained on an LLZO pellet using ic-ac-SECM over a $250 \mu\text{m} \times 250 \mu\text{m}$ area. Reproduced with permission.^[292] Copyright 2016, Frontiers. c) AFM image and d) ion-current image on a polymer/ Li_3PS_4 SSE boundary. e) Current line profile along the dashed line in (d). Reproduced with permission.^[294] Copyright 2020, Wiley-VCH. f) Schematic of the in situ C-AFM measurement on the all-solid-state thin-film battery. g) FIB cross-sectional image of the thin-film battery. h) Cyclic electrical signal applied to the battery by the probe. i-m) The AFM images with height, deflection, and phase signals of the thin-film battery within $1 \mu\text{m} \times 1 \mu\text{m}$ area, at the stages of 1, 2, 4, 6, 8 scans. Reproduced with permission.^[295] Copyright 2012, Elsevier.

and heterogeneous nature.^[297] Although electrochemical methods such as EIS are used in analyzing the bulk/interface mechanism, they are limited only to the resistance information, being blind to the elemental or morphological information.^[298]

The characterization of all-solid-state batteries is less limited by the environmental conditions (no liquid electrolyte) during operation. However, for characterizing the solid–solid interface, a cross-section cut is needed, making true in situ analysis impossible. Equipped with cryo-FIB techniques, which can locate the observation area to the nanoscale, in situ SEM and TEM are available to provide cross-sectional images of thin-film batteries or 3D reconstructed solid–solid interfaces.^[299,300] This approach enables the preparation of the sensitive battery materials and realizes the precise detection of the solid–solid interface with elemental analysis at the nano scale. However, these results are obtained ex situ and do not offer real-time information. To gain in situ characterization of the solid–solid interface a microcell with ultra-thin layers of the battery components is essential, which leads to complicated sample preparation.^[301] For this case, X-ray CT with nanometer-scale resolution is highly desired for the inner interface characterization.

Nonetheless, AFM-based techniques do offer good opportunities for the study of realistic solid-state batteries. Although relatively little work has been done in this area, the ability to obtain a variety of in situ morphological, electrical and mechanical information of interfacial properties of all-solid-state batteries has been clearly established. Hence, compared to those used in EMs, the solid-state batteries used in EC-AFM are more easily prepared and more close to ‘real’ solid-state batteries, as the scan area of the AFM can be easily directed both on the cross-section and lateral surface.

4. Challenges and Outlook

The discussion above highlights the fact that EC-AFM and other closely related techniques have impacted research across alkali metal and related batteries, revealing interfacial, morphological, mechanical, electrical, and electrochemical properties of numerous industry-ready and next-generation electrodes in various electrolytes. Importantly, much of this work has shown these phenomena using in situ or operando techniques, meaning the progression of key processes in battery research including ion intercalation/deintercalation, SEI or CEI evolution, active material volume expansion/contraction, dendrite formation, thin-film electrode structural change, variations in electrical conductivity, surface degradation, formation of intermediates, and the development of the EDL structure have been revealed.

Unfortunately it has also been shown that, to date, a significant proportion of these processes have been investigated using electrode and cell architectures that are often substantially different from those that appear in industrial batteries. Thin film electrodes, highly designed nano- or micro-structures such as pillars or wires, or nanoparticles supported on atomically flat substrates are common electrode materials; the use of HOPG as an analogue for graphite battery anodes

is endemic. Although this does not denigrate the impact or significance of the research findings published, it does raise questions regarding the degree to which they can be used to explain processes at real battery electrodes. Commonly an electrode in a battery is a porous, 3D, multi-component structure, hence the mass transport, kinetic and interfacial properties are highly likely to differ greatly from those at ‘equivalent’ planar model electrodes.

Many other techniques have been developed to study batteries, including those utilizing X-rays, neutrons, visible light, or numerous other ‘probes’ and it can be seen from the comparisons made between these techniques and EC-AFM in the sections above that they succeed, or fail, to differing degrees to be representative of commercial batteries. Although techniques such as X-ray CT excel in enabling the testing of ‘real’ batteries in situ, they do suffer from significantly lower resolution than EC-AFM and are insensitive to many significant battery processes and materials, for example, SEI, Li, that EC-AFM is well suited to visualize. Neutron scattering techniques can provide nanoscale information regarding SEI, Li, and more, in a relatively realistic electrochemical environment, but they are less able to provide this information in a site-specific manner, due to the ‘averaged’ nature of the measurements. Similarly, the data from XPS and NMR is averaged over relatively large areas, compared to that available from EC-AFM, but they can reveal chemical changes that SPM techniques are commonly blind to. The ultra-high vacuum environment required for XPS does, however, mean realistic battery environments are near impossible, whereas NMR can achieve conditions that are much closer. XRD too can provide crystallographic data unavailable via EC-AFM, and allows characterization of buried, rather than interfacial, processes. But although relatively realistic electrodes can be used, the need for X-ray transparent windows can lead to unrepresentative cell geometries and internal electric fields. Hence, as yet, there is no one technique that can enable an all-encompassing, high-resolution, view of industry-relevant batteries and EC-AFM is therefore as, or more, representative as many of the alternatives.

Although the focus of this review is specifically EC-AFM and closely related techniques, it should be noted that there are numerous other SPM techniques that have been utilized for battery analysis. These broadly fall into two categories; those that rely on electrochemical processes or ionic transport, such as scanning electrochemical microscopy (SECM),^[302–305] scanning ion conductance microscopy (SICM),^[306] scanning electrochemical cell microscopy (SECCM)^[307] and electrochemical strain microscopy (ESM),^[308–311] and those that probe properties intrinsic to the electrode material, like Kelvin probe force microscopy (KPFM)^[312,313] and electrostatic force microscopy (EFM).^[314] These techniques, and their application to study battery materials, have been reviewed elsewhere,^[23–25,315–317] but the degree to which they are less, or more, able than EC-AFM to study realistic batteries in relevant environments has not and hence will briefly be discussed.

Traditional SECM, for example, has no, or very limited, in-built topography detection, and therefore requires very flat surfaces to avoid confusion between change in electrochemical activity and change in sample–probe distance.^[318] SECCM, on the other hand, has been developed to ensure a

consistent probe—sample distance,^[319] but the glass capillary-based probe is less able to move across rough surfaces, without becoming damaged or failing, than a solid AFM tip. Also it should be noted that while the highly localized nature of the electrochemical data SECCM enables it is extremely powerful for revealing localized phenomena,^[320] a microscopic electrolyte droplet on an electrode surface is certainly not representative of the environment in a commercial battery. This mode of imaging discounts any influence from any surrounding electrode materials, which are important in multi-component electrodes. In this regard, although SECM, SICM, and SECCM are all able to visualize localized electrochemical processes, including Li⁺ flux, that EC-AFM cannot, the electrochemical environments required for high-quality imaging are significantly more specialized. Complex and challenging results also arise when using ESM to study multi-component systems or low strain materials as it relies on the strain response,^[321,322] although as it has been primarily to study processes in solid-state batteries the electrochemical environments used can be somewhat representative.^[323–325] KPFM^[326] and EFM^[327] have similarly found application for the study of solid-state battery materials, but here too issues arise relating to representation of realistic battery environments due to a lack of consideration for factors such as cell compression, standard in high energy density solid-state batteries.^[328,329]

Hence, among the SPM techniques available, EC-AFM is arguably the most able to represent a real battery environment, in particular those with a liquid electrolyte, and also has the greatest potential for onward developments to improve this representation, while maintaining a breadth of possibilities for morphological and mechanical data collection.

The above analysis highlights that, alongside increased efforts to develop EC-AFM cells with more relevant electrochemical/electrode environments, it must be recognized that this technique, like all others, provides a limited view of battery processes. Hence, it is essential that EC-AFM experiments are coupled with tests that offset these limitations, in particular methods that reveal concurrent structural or chemical change in the electrode bulk rather than purely at the interface, those that probe chemical and crystallographic change, and finally techniques that enable the use of truly industry-relevant battery geometries. Only then will we be able to confidently use this data to explain the origin of the processes that define change and degradation as batteries operate.

Alongside these recommendations, we believe the research directions and methodological suggestions below offer great potential for advancement the field of EC-AFM analysis of batteries, especially as it grows and becomes more widely utilized:

- We acknowledge that moving to systems that are more representative of realistic batteries is going to be a challenge, especially with regard to reducing electrolyte volumes, replicating cell geometries or using porous electrodes. However, there are changes for the better that can be implemented quickly and easily. For example, when studying anode processes, the use of a more realistic cathode should be considered, for example, one based on NMC, as processes at this electrode may impact factors such as electrolyte composition. Similarly, unless specifically studying the impact of additives on electrode processes, the use of electrolytes with ‘standard’

additives such as VC or FEC should be considered to improve consistency with those in industrial cells. Finally, when choosing a flat ‘analogue’ material, one should be chosen that is more representative of materials within commercial cells, for example, using graphite particles rather than HOPG.

- Interfacial battery processes can occur at very high rates, meaning conventional low-speed AFM imaging (i.e., the order of minutes for an image) can miss important processes or fail to visualize ‘nucleation’ phenomena. Hence, moving toward high-speed AFM,^[330,331] without loss of resolution or ability to simultaneously measure mechanical and conductive properties, would be highly beneficial.
- Standard AFM techniques cannot determine site-specific chemical information, limiting the scope of interpretation of material evolution. It would be extremely beneficial to expand the exploration of local chemical and physical properties while under electrochemical control, with techniques such as AFM-Raman^[332–335] or AFM-IR.^[336] Similarly, wider application of ‘active tip’ tools such as AFM-SECM^[337,338] will enable greater understanding of localized electrochemical processes.
- Negative interactions between the tip and sample (e.g., tip shielding and tip sweeping effects) should be carefully considered when analyzing data obtained by AFM and related SPM techniques. For small samples and features, tip convolution, that is, imaging artefacts due to the tip radius being larger than the feature being imaged, can cause particular problems. This can also occur when the tip size/shape subtly changes during electrochemical cycling. As studies of nanoscale battery materials, materials with important nanoscale changes, or those examined during charge/discharge processes that produce detachable products become more common, it is important that authors carefully examine their data for these effects before drawing more complex conclusions.
- By its nature, EC-AFM requires a probe to be close to the electrode surface, but this can cause a significantly different flux within, and across, the area being imaged, in comparison to that far away from the probe.^[339] This can mean the interfacial process can vary significantly across the electrode. Hence, efforts should be made to design cells with a mass transport regime that is consistent both under and away from the tip, and to engage simulation tools to understand tip effects.
- In EC-AFM macroscale electrodes are commonly used, meaning the current response may be dominated by phenomena that are not occurring within the viewing ‘window’ provided by the AFM image. Researchers should work to utilize electrode designs that ensure a significant proportion of the current response derives from the area being imaged, to avoid building a disjointed picture of battery chemistry.

Acknowledgements

The present research was supported by the Faraday Institution (EP/S003053/1), degradation project (FIRG001), LISTAR project (FIRG014), and EPSRC (EP/R023581/1, EP/P009050/1, EP/N032888/1). T.S.M. thanks

the UK EPSRC for support via his Fellowship EP/P023851/1. P.R.S. acknowledges The Royal Academy of Engineering (CiET1718/59).

Conflict of Interest

The authors declare no conflict of interest.

Keywords

degradation, EC-AFM, electrode–electrolyte interface, in situ/operando characterization, lithium-ion batteries, real battery environment, scanning probe microscopy

Received: May 14, 2021

Revised: July 16, 2021

Published online:

- [1] M. Marinaro, D. Bresser, E. Beyer, P. Faguy, K. Hosoi, H. Li, J. Sakovica, K. Amine, M. Wohlfahrt-Mehrens, S. Passerini, *J. Power Sources* **2020**, 459, 228073.
- [2] N. Nitta, F. Wu, J. T. Lee, G. Yushin, *Mater. Today* **2015**, 18, 252.
- [3] J. P. Pender, G. Jha, D. H. Youn, J. M. Ziegler, I. Andoni, E. J. Choi, A. Heller, B. S. Dunn, P. S. Weiss, R. W. Penner, C. B. Mullins, *ACS Nano* **2020**, 14, 1243.
- [4] A. Wang, S. Kadam, H. Li, S. Shi, Y. Qi, *NPJ Comput. Mater.* **2018**, 4, 15.
- [5] E. Peled, S. Menkin, *J. Electrochem. Soc.* **2017**, 164, A1703.
- [6] Y. Zhou, M. Su, X. Yu, Y. Zhang, J. G. Wang, X. Ren, R. Cao, W. Xu, D. R. Baer, Y. Du, O. Borodin, Y. Wang, X. L. Wang, K. Xu, Z. Xu, C. Wang, Z. Zhu, *Nat. Nanotechnol.* **2020**, 15, 224.
- [7] Z. Qu, M. Zhu, H. Tang, L. Liu, Y. Li, O. G. Schmidt, *Energy Storage Mater.* **2020**, 29, 17.
- [8] A. M. Tripathi, W. N. Su, B. J. Hwang, *Chem. Soc. Rev.* **2018**, 47, 736.
- [9] D. Liu, Z. Shadike, R. Lin, K. Qian, H. Li, K. Li, S. Wang, Q. Yu, M. Liu, S. Ganapathy, X. Qin, Q. H. Yang, M. Wagemaker, F. Kang, X. Q. Yang, B. Li, *Adv. Mater.* **2019**, 31, 1806620.
- [10] A. V. Llewellyn, A. Matruglio, D. J. L. Brett, R. Jervis, P. S. Shearing, *Condens. Matter* **2020**, 5, 75.
- [11] K. Ni, X. Wang, Z. Tao, J. Yang, N. Shu, J. Ye, F. Pan, J. Xie, Z. Tan, X. Sun, J. Liu, Z. Qi, Y. Chen, X. Wu, Y. Zhu, *Adv. Mater.* **2019**, 31, 1808091.
- [12] G. Rong, X. Zhang, W. Zhao, Y. Qiu, M. Liu, F. Ye, Y. Xu, J. Chen, Y. Hou, W. Li, W. Duan, Y. Zhang, *Adv. Mater.* **2017**, 29, 1606187.
- [13] X. H. Liu, J. W. Wang, S. Huang, F. Fan, X. Huang, Y. Liu, S. Krylyuk, J. Yoo, S. A. Dayeh, A. V. Davydov, S. X. Mao, S. T. Picraux, S. Zhang, J. Li, T. Zhu, J. Y. Huang, *Nat. Nanotechnol.* **2012**, 7, 749.
- [14] D. P. Finegan, M. Scheel, J. B. Robinson, B. Tjaden, I. Hunt, T. J. Mason, J. Millichamp, M. D. Michiel, G. J. Offer, G. Hinds, D. J. L. Brett, P. R. Shearing, *Nat. Commun.* **2015**, 6, 6924.
- [15] E. M. Tennyson, C. Gong, M. S. Leite, *ACS Energy Lett.* **2017**, 2, 2761.
- [16] M. Krieg, G. Flaschner, D. Alsteens, B. M. Gaub, W. H. Roos, G. J. L. Wuite, H. E. Gaub, C. Gerber, Y. F. Dufrene, D. J. Muller, *Nat. Rev. Phys.* **2019**, 1, 41.
- [17] J. Zhang, R. Wang, X. Yang, W. Lu, X. Wu, X. Wang, H. Li, L. Chen, *Nano Lett.* **2012**, 12, 2153.
- [18] T. M. Arruda, M. Heon, V. Presser, P. C. Hillesheim, S. Dai, Y. Gogotsi, S. V. Kalinin, N. Balke, *Energy Environ. Sci.* **2013**, 6, 225.
- [19] Z. Deng, X. Lin, Z. Huang, J. Meng, Y. Zhong, G. Ma, Y. Zhou, Y. Shen, H. Ding, Y. Huang, *Adv. Energy Mater.* **2020**, 11, 2000806.
- [20] S. F. Amalraj, D. Aurbach, *J. Solid State Electrochem.* **2011**, 15, 877.
- [21] S. Wang, Q. Liu, C. Zhao, F. Lv, X. Qin, H. Du, F. Kang, B. Li, *Energy Environ. Mater.* **2018**, 1, 28.
- [22] W. Zhao, W. Song, L. Z. Cheong, D. Wang, H. Li, B. Flemming, F. Huang, C. Shen, *Ultramicroscopy* **2019**, 204, 34.
- [23] S. V. Kalinin, N. Balke, *Adv. Mater.* **2010**, 22, E193.
- [24] R. Kempaiah, G. Vasudevamurthy, A. Subramanian, *Nano Energy* **2019**, 65, 103925.
- [25] L. Danis, S. M. Gateman, C. Kuss, S. B. Schougaard, J. Mauzeroll, *ChemElectroChem* **2017**, 4, 6.
- [26] S. V. Kalinin, O. Dyck, N. Balke, S. Neumayer, W. Y. Tsai, R. Vasudevan, D. Lingerfelt, M. Ahmadi, M. Ziatdinov, M. T. McDowell, E. Strelcov, *ACS Nano* **2019**, 13, 9735.
- [27] Y. Liang, J. H. K. Pfisterer, D. McLaughlin, C. Csoklich, L. Seidl, A. S. Bandarenka, O. Schneider, *Small Methods* **2019**, 3, 1800387.
- [28] S. Zhang, J. Chen, J. Liu, H. Pyles, D. Baker, C. L. Chen, J. J. D. Yoreo, *Adv. Mater.* **2020**, 33, 1905784.
- [29] B. Voigtländer, *Atomic Force Microscopy*, Springer, Jülich, Germany **2019**.
- [30] Y. F. Dufrene, T. Ando, R. Garcia, D. Alsteens, D. Martinez-Martin, A. Engel, C. Gerber, D. J. Muller, *Nat. Nanotechnol.* **2017**, 12, 295.
- [31] N. Jalili, K. Laxminarayana, *Mechatronics* **2004**, 14, 907.
- [32] X. Teng, Y. Guo, D. Liu, G. Li, C. Yu, J. Dai, *J. Membr. Sci.* **2020**, 601, 117906.
- [33] L. Y. Beaulieu, V. K. Cumyn, K. W. Eberman, L. J. Krause, J. R. Dahn, *Rev. Sci. Instrum.* **2001**, 72, 3313.
- [34] D. Aurbach, Y. Cohen, *Electrochem. Solid-State Lett.* **1999**, 2, 16.
- [35] V. Palomares, N. Sharma, *Front. Energy Res.* **2019**, 7, 10.
- [36] H. Chen, Z. Qin, M. He, Y. Liu, Z. Wu, *Materials* **2020**, 13, 668.
- [37] H. Si, S. Zhang, S. Ma, Z. Xiong, A. Kausar, Q. Liao, Z. Zhang, A. Sattar, Z. Kang, Y. Zhang, *Adv. Energy Mater.* **2020**, 10, 1903922.
- [38] J. O. Beeck, N. Labyedh, A. Sepulveda, V. Spampinato, A. Franquet, T. Conard, P. M. Vereecken, W. Vandervorst, U. Celano, *Beilstein J. Nanotechnol.* **2018**, 9, 1623.
- [39] W. Lee, F. B. Prinz, X. Chen, S. Nonnenmann, *MRS Bull.* **2012**, 37, 659.
- [40] C. Stetson, Z. Huey, A. Downard, Z. Li, B. To, A. Zakutayev, C. S. Jiang, M. M. Al-Jassim, D. P. Finegan, S. D. Han, S. C. Decaluwe, *Nano Lett.* **2020**, 20, 8081.
- [41] R. Ferencz, J. Sanchez, B. Blumich, W. Herrmann, *Polym. Test.* **2012**, 31, 425.
- [42] H. Shin, J. Park, S. Han, A. M. Sastry, W. Lu, *J. Power Sources* **2015**, 277, 169.
- [43] K. Xu, W. Sun, Y. Shao, F. Wei, X. Zhang, W. Wang, P. Li, *Nanotechnol. Rev.* **2018**, 7, 605.
- [44] J. Come, Y. Xie, M. Naguib, S. Jesse, S. V. Kalinin, Y. Gogotsi, P. R. C. Kent, N. Balke, *Adv. Energy Mater.* **2016**, 6, 1502290.
- [45] D. Castelveccchi, E. Stoye, *Nature* **2019**, 574, 308.
- [46] J. W. Choi, D. Aurbach, *Nat. Rev. Mater.* **2016**, 1, 16013.
- [47] J. Xie, Y. C. Lu, *Nat. Commun.* **2020**, 11, 2499.
- [48] X. Lu, A. Bertei, D. P. Finegan, C. Tan, S. R. Daemi, J. S. Weaving, K. B. O'Regan, T. M. M. Heenan, G. Hinds, E. Kendrick, D. J. L. Brett, P. R. Shearing, *Nat. Commun.* **2020**, 11, 2079.
- [49] C. L. Bentley, M. Kang, P. R. Unwin, *J. Am. Chem. Soc.* **2019**, 141, 2179.
- [50] F. Wu, J. Maier, Y. Yu, *Chem. Soc. Rev.* **2020**, 49, 1569.
- [51] W. M. Dose, C. Xu, C. P. Grey, M. F. L. De Volder, *Cell Rep. Phys. Sci.* **2020**, 1, 100253.
- [52] S. C. Nagpure, B. Bhushan, *Applied Scanning Probe methods XIII, NanoScience and Technology*, Springer, Berlin, Heidelberg, **2009**, pp. 203–233.
- [53] L. Wang, A. Menakath, F. Han, Y. Wang, P. Y. Zavalij, K. J. Gaskell, O. Borodin, D. Iuga, S. P. Brown, C. Wang, K. Xu, B. W. Eichhorn, *Nat. Chem.* **2019**, 11, 789.
- [54] M. Nie, J. Demeaux, B. T. Young, D. R. Heskett, Y. Chen, A. Bose, J. C. Woicik, B. L. Lucht, *J. Electrochem. Soc.* **2015**, 162, A7008.

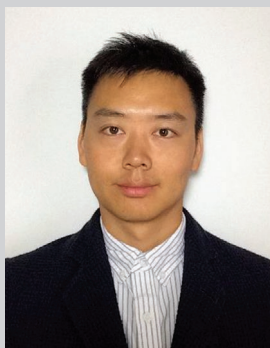
- [55] S. Tsubouchi, Y. Domi, T. Doi, M. Ochida, H. Nakagawa, T. Yamanaka, T. Abe, Z. Ogumi, *J. Electrochem. Soc.* **2012**, *159*, A1786.
- [56] S. J. An, J. Li, C. Daniel, D. Mohanty, S. Nagpure, D. L. Wood III, *Carbon* **2016**, *105*, 52.
- [57] S. Yamaguchi, H. Asahina, K. A. Hirasawa, T. Sato, S. Mori, *Mol. Cryst. Liq. Cryst.* **1998**, *322*, 239.
- [58] K. A. Hirasawa, T. Sato, H. Asahina, S. Yamaguchi, S. Mori, *J. Electrochem. Soc.* **1997**, *144*, L81.
- [59] C. Shen, S. Wang, Y. Jin, W. Q. Han, *ACS Appl. Mater. Interfaces* **2015**, *7*, 25441.
- [60] M. Ochida, Y. Domi, T. Doi, S. Tsubouchi, H. Nakagawa, T. Yamanaka, T. Abe, Z. Ogumi, *J. Electrochem. Soc.* **2012**, *159*, A961.
- [61] M. Koltypin, Y. S. Cohen, B. Markovsky, Y. Cohen, D. Aurbach, *Electrochem. Commun.* **2002**, *4*, 17.
- [62] S. K. Jeong, M. Inaba, Y. Iriyama, T. Abe, Z. Ogumi, *Electrochim. Acta* **2002**, *47*, 1975.
- [63] S. K. Jeong, M. Inaba, R. Mogi, Y. Iriyama, T. Abe, Z. Ogumi, *Langmuir* **2001**, *17*, 8281.
- [64] L. Lin, K. Yang, R. Tan, M. Li, S. Fu, T. Liu, H. Chen, F. Pan, *J. Mater. Chem. A* **2017**, *5*, 19364.
- [65] Y. S. Kim, S. K. Jeong, *J. Spectrosc.* **2015**, *2015*, 462140.
- [66] S. K. Jeong, M. Inaba, Y. Iriyama, T. Abe, Z. Ogumi, *J. Power Sources* **2003**, *119–121*, 555.
- [67] D. Aurbach, M. Koltypin, H. Teller, *Langmuir* **2002**, *18*, 9000.
- [68] G. Yang, J. Shi, C. Shen, S. Wang, L. Xia, H. Hu, H. Luo, Y. Xia, Z. Liu, *RSC Adv.* **2017**, *7*, 26052.
- [69] M. Inaba, H. Tomiyasu, A. Tasaka, S. K. Jeong, Z. Ogumi, *Langmuir* **2004**, *20*, 1348.
- [70] S. K. Jeong, M. Inaba, Y. Iriyama, T. Abe, Z. Ogumi, *J. Power Sources* **2008**, *175*, 540.
- [71] X. R. Liu, L. Wang, L. J. Wan, D. Wang, *ACS Appl. Mater. Interfaces* **2015**, *7*, 9573.
- [72] K. Edstrom, M. Herranen, *J. Electrochem. Soc.* **2000**, *147*, 3628.
- [73] F. P. Campana, H. Kotz, J. Vetter, P. Novak, H. Siegenthaler, *Electrochem. Commun.* **2005**, *7*, 107.
- [74] D. Alliata, R. Kotz, P. Novak, H. Siegenthaler, *Electrochem. Commun.* **2000**, *2*, 436.
- [75] Y. Domi, T. Doi, T. Yamanaka, T. Abe, Z. Ogumi, *J. Electrochem. Soc.* **2013**, *160*, A678.
- [76] L. Wang, D. Deng, L. C. Lev, S. Ng, *J. Power Sources* **2014**, *265*, 140.
- [77] Y. Domi, M. Ochida, S. Tsubouchi, H. Nakagawa, T. Yamanaka, T. Doi, T. Abe, Z. Ogumi, *J. Electrochem. Soc.* **2012**, *159*, A1292.
- [78] O. Matsuoka, A. Hiwara, T. Omi, M. Toriida, T. Hayashi, C. Tanaka, Y. Saito, T. Ishida, H. Tan, S. S. Ono, S. Yamamoto, *J. Power Sources* **2002**, *108*, 128.
- [79] J. Yan, J. Zhang, Y. C. Su, X. G. Zhang, B. J. Xia, *Electrochim. Acta* **2010**, *55*, 1785.
- [80] Y. Yamada, K. Miyazaki, T. Abe, *Langmuir* **2010**, *26*, 14990.
- [81] M. Velicky, P. S. Toth, C. R. Woods, K. S. Novoselov, R. A. W. Dryfe, *J. Phys. Chem. C* **2019**, *123*, 11677.
- [82] Y. Domi, M. Ochida, S. Tsubouchi, H. Nakagawa, T. Yamanaka, T. Doi, T. Abe, Z. Ogumi, *J. Phys. Chem. C* **2011**, *115*, 25484.
- [83] F. P. Campana, H. Buqa, P. Novak, R. Kotz, H. Siegenthaler, *Electrochem. Commun.* **2008**, *10*, 1590.
- [84] L. Seidl, S. Martens, J. Ma, U. Stimming, O. Schneider, *Nanoscale* **2016**, *8*, 14004.
- [85] D. Alliata, R. Kotz, O. Haas, *Langmuir* **1999**, *15*, 8483.
- [86] K. Yang, L. Jia, X. Liu, Z. Wang, Y. Wang, Y. Li, H. Chen, B. Wu, L. Yang, F. Pan, *Nano Res.* **2020**, *13*, 412.
- [87] X. Deng, X. Liu, H. Yan, D. Wang, L. Wan, *Sci. China Chem.* **2014**, *57*, 178.
- [88] C. Shen, G. Hu, L. Z. Cheong, S. Huang, J. G. Zhang, D. Wang, *Small Methods* **2018**, *2*, 1700298.
- [89] V. Sharova, A. Moretti, T. Diemant, A. Varzi, R. J. Behm, S. Passerini, *J. Power Sources* **2018**, *375*, 43.
- [90] H. Zhang, D. Wang, C. Shen, *Appl. Surf. Sci.* **2020**, *507*, 145059.
- [91] Z. Zhang, K. Smith, R. Jervis, P. R. Shearing, T. S. Miller, D. J. L. Brett, *ACS Appl. Mater. Interfaces* **2020**, *12*, 35132.
- [92] M. Steinhauer, M. Stich, M. Kurniawan, B. K. Seidlhofer, M. Trapp, A. Bund, N. Wagner, K. A. Friedrich, *ACS Appl. Mater. Interfaces* **2017**, *9*, 35794.
- [93] A. v. Cresce, S. M. Russell, D. R. Baker, K. J. Gaskell, K. Xu, *Nano Lett.* **2014**, *14*, 1405.
- [94] S. Leroy, F. Blanchard, R. Dedryvere, H. Martinez, B. Carre, D. Lemordant, D. Gonbeau, *Surf. Interface Anal.* **2005**, *37*, 773.
- [95] T. Liu, L. Lin, X. Bi, L. Tian, K. Yang, J. Liu, M. Li, Z. Chen, J. Lu, K. Amine, K. Xu, F. Pan, *Nat. Nanotechnol.* **2019**, *14*, 50.
- [96] H. Kawaura, M. Harada, Y. Kondo, H. Kondo, Y. Suganuma, N. Takahashi, J. Sugiyama, Y. Seno, N. L. Yamada, *ACS Appl. Mater. Interfaces* **2016**, *8*, 9540.
- [97] J. E. Owejan, J. P. Owejan, S. C. DeCaluwe, J. A. Dura, *Chem. Mater.* **2012**, *24*, 2133.
- [98] C. J. Jafta, X. G. Sun, G. M. Veith, G. V. Jensen, S. M. Mahurin, M. P. Paranthaman, S. Dai, C. A. Bridges, *Energy Environ. Sci.* **2019**, *12*, 1866.
- [99] R. Saito, M. Hofmann, G. Dresselhaus, A. Jorio, M. S. Dresselhaus, *Adv. Phys.* **2011**, *60*, 413.
- [100] C. Sole, N. E. Drewett, L. J. Hardwick, *Faraday Discuss.* **2014**, *172*, 223.
- [101] L. J. Hardwick, P. W. Ruch, M. Hahn, W. Scheifele, R. Kötz, P. Novák, *J. Phys. Chem. Solids* **2008**, *69*, 1232.
- [102] M. Inaba, H. Yoshida, Z. Ogumi, *J. Electrochem. Soc.* **1996**, *143*, 2572.
- [103] J. S. Weaving, A. Lim, J. Millichamp, T. P. Neville, D. Ledwoch, E. Kendrick, P. F. McMillan, P. S. Shearing, C. A. Howard, D. J. L. Brett, *ACS Appl. Energy Mater.* **2020**, *3*, 7474.
- [104] M. A. Reddy, M. Helen, A. Groß, M. Fichtner, H. Euchner, *ACS Energy Lett.* **2018**, *3*, 2851.
- [105] C. A. Howard, M. P. M. Dean, F. Withers, *Phys. Rev. B* **2011**, *84*, 241404.
- [106] H. Li, T. Yamaguchi, S. Matsumoto, H. Hoshikawa, T. Kumagai, N. L. Okamoto, T. Ichitsubo, *Nat. Commun.* **2020**, *11*, 1584.
- [107] H. Y. Song, S. S. Kim, P. M. Nogales, S. K. Jeong, *J. Nanosci. Nanotechnol.* **2020**, *20*, 4985.
- [108] B. Breitung, P. Baumann, H. Sommer, J. Janek, T. Brezesinski, *Nanoscale* **2016**, *8*, 14048.
- [109] A. Magasinski, P. Dixon, B. Hertzberg, A. Kvit, J. Ayala, G. Yushin, *Nat. Mater.* **2010**, *9*, 353.
- [110] Q. Xiao, M. Gu, H. Yang, B. Li, C. Zhang, Y. Liu, F. Liu, F. Dai, L. Yang, Z. Liu, X. Xiao, G. Liu, P. Zhao, S. Zhang, C. Wang, Y. Lu, M. Cai, *Nat. Commun.* **2015**, *6*, 8844.
- [111] L. Martin, H. Martinez, M. Ulldemolins, B. Pecquenard, F. L. Cras, *Solid State Ionics* **2012**, *215*, 36.
- [112] S. Benning, C. Chen, R. A. Eichel, P. H. L. Notten, F. Hausen, *ACS Appl. Energy Mater.* **2019**, *2*, 6761.
- [113] L. Y. Beaulieu, T. D. Hatchard, A. Bonakdarpour, M. D. Fleischauer, J. R. Dahn, *J. Electrochem. Soc.* **2003**, *111*, A1457.
- [114] C. R. Becker, K. E. Strawhecker, Q. P. McAllister, C. A. Lundgren, *ACS Nano* **2013**, *7*, 9173.
- [115] M. Han, C. Zhu, Q. Zhao, C. Chen, Z. Tao, W. Xie, F. Cheng, J. Chen, *ACS Appl. Mater. Interfaces* **2017**, *9*, 28620.
- [116] I. T. Lucas, E. Pollak, R. Kostecki, *Electrochem. Commun.* **2009**, *11*, 2157.
- [117] Y. Tian, A. Timmons, J. R. Dahn, *J. Electrochem. Soc.* **2009**, *156*, A187.
- [118] B. Moeremans, H. W. Cheng, C. Merola, Q. Hu, M. Oezaslam, M. Safari, M. K. V. Bael, A. Hardy, M. Valtiner, F. U. Renner, *Adv. Sci.* **2019**, *6*, 1900190.

- [119] I. Yoon, D. P. Abraham, B. L. Lucht, A. F. Bower, P. R. Guduru, *Adv. Energy Mater.* **2016**, *6*, 1600099.
- [120] A. Lahiri, G. Li, M. Olschewski, F. Endres, *ACS Appl. Mater. Interfaces* **2016**, *8*, 34143.
- [121] A. Lahiri, N. Borisenko, A. Borodin, M. Olschewski, F. Endres, *Phys. Chem. Chem. Phys.* **2016**, *18*, 5630.
- [122] J. Chen, X. Fan, Q. Li, H. Yang, M. R. Khoshi, Y. Xu, S. Hwang, L. Chen, X. Ji, C. Yang, H. He, C. Wang, E. Garfunkel, D. Su, O. Borodin, C. Wang, *Nat. Energy* **2020**, *5*, 386.
- [123] X. R. Liu, X. Deng, R. R. Liu, H. J. Yan, Y. G. Guo, D. Wang, L. J. Wan, *ACS Appl. Mater. Interfaces* **2014**, *6*, 20317.
- [124] Y. Shi, J. Wan, J. Y. Li, X. C. Hu, S. Y. Lang, Z. Z. Shen, G. Li, H. J. Yan, K. C. Jiang, Y. G. Guo, R. Wen, L. J. Wan, *Nano Energy* **2019**, *61*, 304.
- [125] M. Lee, R. K. R. Reddi, J. Choi, J. Liu, X. Huang, H. Cho, J. H. Kim, *ACS Appl. Energy Mater.* **2020**, *3*, 1899.
- [126] A. Tokranov, R. Kumar, C. Li, S. Minne, X. Xiao, B. W. Sheldon, *Adv. Energy Mater.* **2016**, *6*, 1502302.
- [127] V. Kuznetsov, A. H. Zinn, G. Zampardi, S. Borhani-Haghighi, F. L. Mantia, A. Ludwig, W. Schuhmann, E. Ventosa, *ACS Appl. Mater. Interfaces* **2015**, *7*, 23554.
- [128] Q. P. McAllister, K. E. Strawhecker, C. R. Becker, C. A. Lundgren, *J. Power Sources* **2014**, *257*, 380.
- [129] A. Tokranov, B. W. Sheldon, C. Li, S. Minne, X. Xiao, *ACS Appl. Mater. Interfaces* **2014**, *6*, 6672.
- [130] C. R. Becker, S. M. Prokes, C. T. Love, *ACS Appl. Mater. Interfaces* **2016**, *8*, 530.
- [131] R. Kumar, A. Tokranov, B. W. Sheldon, X. Xiao, Z. Huang, C. Li, T. Mueller, *ACS Energy Lett.* **2016**, *1*, 689.
- [132] K. Guo, R. Kumar, X. Xiao, B. W. Sheldon, H. Gao, *Nano Energy* **2018**, *49*, 1.
- [133] J. Zheng, H. Zheng, R. Wang, L. Ben, W. Lu, L. Chen, L. Chen, H. Li, *Phys. Chem. Chem. Phys.* **2014**, *16*, 13229.
- [134] T. M. M. Heenan, A. Jnawali, M. D. R. Kok, T. G. Tranter, C. Tan, A. Dimitrijevic, R. Jervis, D. J. L. Brett, P. R. Shearing, *J. Electrochem. Soc.* **2020**, *167*, 140530.
- [135] R. Zhao, S. Wang, D. Liu, Y. Liu, X. Lv, X. Zeng, B. Li, *ACS Appl. Energy Mater.* **2021**, *4*, 492.
- [136] Y. Yuan, K. Amine, J. Lu, R. Shahbazian-Yassar, *Nat. Commun.* **2017**, *8*, 15806.
- [137] M. T. McDowell, S. W. Lee, W. D. Nix, Y. Cui, *Adv. Mater.* **2013**, *25*, 4966.
- [138] M. J. Zachman, Z. Tu, S. Choudhury, L. A. Archer, L. F. Kourkoutis, *Nature* **2018**, *560*, 345.
- [139] M. G. Boebinger, O. Yarema, M. Yarema, K. A. Unocic, R. R. Unocic, V. Wood, M. T. McDowell, *Nat. Nanotechnol.* **2020**, *15*, 475.
- [140] Y. Cheng, L. Zhang, Q. Zhang, J. Li, Y. Tang, C. Delmas, T. Zhu, M. Winter, M. S. Wang, J. Huang, *Mater. Today* **2020**, *42*, 137.
- [141] S. Chae, M. Ko, K. Kim, K. Ahn, J. Cho, *Joule* **2017**, *1*, 47.
- [142] P. Biswal, S. Stalin, A. Kludze, S. Choudhry, L. A. Archer, *Nano Lett.* **2019**, *19*, 8191.
- [143] W. Xu, J. Wang, F. Ding, X. Chen, E. Nasybulin, Y. Zhang, J. G. Zhang, *Energy Environ. Sci.* **2014**, *7*, 513.
- [144] D. Aurbach, Y. Cohen, *J. Electrochem. Soc.* **1996**, *143*, 3525.
- [145] K. Morigaki, A. Ohta, *J. Power Sources* **1998**, *76*, 159.
- [146] K. Morigaki, *J. Power Sources* **2002**, *104*, 13.
- [147] M. Kitta, H. Sano, *Langmuir* **2017**, *33*, 1861.
- [148] N. Weadock, N. Varongchayakul, J. Wan, S. Lee, J. Seog, L. Hu, *Nano Energy* **2013**, *2*, 713.
- [149] N. W. Li, Y. X. Yin, C. P. Yang, Y. G. Guo, *Adv. Mater.* **2016**, *28*, 1853.
- [150] Y. Sun, M. Amirmaleki, Y. Zhao, C. Zhao, J. Liang, C. Wang, K. R. Adair, J. Li, T. Cui, G. Wang, R. Li, T. Filleter, M. Cai, T. K. Sham, X. Sun, *Adv. Energy Mater.* **2020**, *10*, 2001139.
- [151] S. J. Tan, J. Yue, X. C. Hu, Z. Z. Shen, W. P. Wang, J. Y. Li, T. T. Zuo, H. Duan, Y. Xiao, Y. X. Yin, R. Wen, Y. G. Guo, *Angew. Chem., Int. Ed.* **2019**, *58*, 7802.
- [152] Z. Hu, S. Zhang, S. Dong, Q. Li, G. Cui, L. Chen, *Chem. Mater.* **2018**, *30*, 4039.
- [153] B. Xu, Z. Liu, J. Li, X. Huang, B. Qie, T. Gong, L. Tan, X. Yang, D. Paley, M. Dontigny, K. Zaghbi, X. Liao, Q. Chen, H. Zhai, X. Chen, L. Q. Chen, C. W. Nan, Y. H. Lin, Y. Yang, *Nano Energy* **2020**, *67*, 104242.
- [154] X. Liu, J. Liu, T. Qian, H. Chen, C. Yan, *Adv. Mater.* **2019**, *32*, 1902724.
- [155] W. Liu, Y. Xia, W. Wang, Y. Wang, J. Jin, Y. Chen, E. Paek, D. Mitlin, *Adv. Energy Mater.* **2019**, *9*, 1802918.
- [156] Y. Zhou, X. Zhang, Y. Ding, L. Zhang, G. Yu, *Adv. Mater.* **2020**, *32*, 2005763.
- [157] D. Chen, S. Huang, L. Zhong, S. Wang, M. Xiao, D. Han, Y. Meng, *Adv. Funct. Mater.* **2019**, *30*, 1907717.
- [158] M. Zhang, L. Xiang, M. Galluzzi, C. Jiang, S. Zhang, J. Li, Y. Tang, *Adv. Mater.* **2019**, *31*, 1900826.
- [159] T. Jang, J. H. Kang, S. Kim, M. Shim, J. Lee, J. Song, W. Kim, K. Ryu, H. R. Byon, *ACS Appl. Energy Mater.* **2021**, *4*, 2644.
- [160] Y. S. Cohen, Y. Cohen, D. Aurbach, *J. Phys. Chem. B* **2000**, *2014*, 12282.
- [161] S. Y. Lang, Z. Z. Shen, X. C. Hu, Y. Shi, Y. G. Guo, F. F. Jia, F. Y. Wang, R. Wen, L. J. Wan, *Nano Energy* **2020**, *75*, 104967.
- [162] M. Wang, L. Huai, G. Hu, S. Yang, F. Ren, S. Wang, Z. Zhang, Z. Chen, Z. Peng, C. Shen, D. Wang, *J. Phys. Chem. C* **2018**, *122*, 9825.
- [163] J. Zhao, L. Liao, F. Shi, T. Lei, G. Chen, A. Pei, J. Sun, K. Yan, G. Zhou, J. Xie, C. Liu, Y. Li, Z. Liang, Z. Bao, Y. Cui, *J. Am. Chem. Soc.* **2017**, *139*, 11550.
- [164] J. Wang, J. Yang, Q. Xiao, J. Zhang, T. Li, L. Jia, Z. Wang, S. Cheng, L. Li, M. Liu, H. Liu, H. Lin, Y. Zhang, *Adv. Funct. Mater.* **2020**, *31*, 2007434.
- [165] Y. Gu, W. W. Wang, Y. J. Li, Q. H. Wu, S. Tang, J. W. Yan, M. S. Zheng, D. Y. Wu, C. H. Fan, W. Q. Hu, Z. B. Chen, Y. Fang, Q. H. Zhang, Q. F. Dong, B. W. Mao, *Nat. Commun.* **2018**, *9*, 1339.
- [166] Y. Han, Y. Jie, F. Huang, Y. Chen, Z. Lei, G. Zhang, X. Ren, L. Qin, R. Cao, S. Jiao, *Adv. Funct. Mater.* **2019**, *29*, 1904629.
- [167] W. Lu, L. Sun, Y. Zhao, T. Wu, L. Cong, J. Liu, Y. Liu, H. Xie, *Energy Storage Mater.* **2021**, *34*, 241.
- [168] C. F. Lin, A. C. Kozen, M. Noked, C. Liu, G. W. Rubloff, *Adv. Mater. Interfaces* **2016**, *3*, 1600426.
- [169] N. W. Li, Y. Shi, Y. X. Yin, X. X. Zeng, J. Y. Li, C. J. Li, L. J. Wan, R. Wen, Y. G. Guo, *Angew. Chem., Int. Ed.* **2018**, *57*, 1505.
- [170] Y. Gao, Z. Yan, J. L. Gray, X. He, D. Wang, T. Chen, Q. Huang, Y. C. Li, H. Wang, S. H. Kim, T. E. Mallouk, D. Wang, *Nat. Mater.* **2019**, *18*, 384.
- [171] X. Shen, Y. Li, T. Qian, J. Liu, J. Zhou, C. Yan, J. B. Goodenough, *Nat. Commun.* **2019**, *10*, 900.
- [172] Y. Wu, N. Liu, *Chem* **2018**, *4*, 438.
- [173] C. Yan, X. B. Cheng, Y. X. Yao, X. Shen, B. Q. Li, W. J. Li, R. Zhang, J. Q. Huang, H. Li, Q. Zhang, *Adv. Mater.* **2018**, *30*, 1804461.
- [174] P. Bai, J. Li, F. R. Brushett, M. Z. Bazant, *Energy Environ. Sci.* **2016**, *9*, 3221.
- [175] Y. Zhu, J. Xie, A. Pei, B. Liu, Y. Wu, D. Lin, J. Li, H. Wang, H. Chen, J. Xu, A. Yang, C. L. Wu, H. Wang, W. Chen, Y. Cui, *Nat. Commun.* **2019**, *10*, 2067.
- [176] X. Q. Zhang, X. Chen, X. B. Cheng, B. Q. Li, X. Shen, C. Yan, J. Q. Huang, Q. Zhang, *Angew. Chem., Int. Ed.* **2018**, *57*, 5301.
- [177] L. Porz, T. Swamy, B. W. Sheldon, D. Rettenwander, T. Frömling, H. L. Thaman, S. Berendts, R. Uecker, W. C. Carter, Y. M. Chiang, *Adv. Energy Mater.* **2017**, *7*, 1701003.
- [178] Y. Shi, J. Wan, G. X. Liu, T. T. Zuo, Y. X. Song, B. Liu, Y. G. Guo, R. Wen, L. J. Wan, *Angew. Chem., Int. Ed.* **2020**, *59*, 18120.

- [179] M. Han, C. Zhu, T. Ma, Z. Pan, Z. Tao, J. Chen, *Chem. Commun.* **2018**, 54, 2381.
- [180] X. Guo, Z. Zhang, J. Li, N. Luo, G. L. Chai, T. S. Miller, F. Lai, P. Shearing, D. J. L. Brett, D. Han, Z. Weng, G. He, I. P. Parkin, *ACS Energy Lett.* **2021**, 6, 395.
- [181] Q. Yang, G. Liang, Y. Guo, Z. Liu, B. Yan, D. Wang, Z. Huang, X. Li, J. Fan, C. Zhi, *Adv. Mater.* **2019**, 31, 1903778.
- [182] S. Wang, Z. Wang, Y. Yin, T. Li, N. Chang, F. Fan, H. Zhang, X. Li, *Energy Environ. Sci.* **2021**, 14, 4077.
- [183] Z. Zhang, S. Said, K. Smith, Y. S. Zhang, G. He, R. Jervis, P. R. Shearing, T. S. Miller, D. J. L. Brett, *J. Mater. Chem. A* **2021**, 9, 15355.
- [184] S. Fang, D. Bresser, S. Passerini, *Adv. Energy Mater.* **2020**, 10, 1902485.
- [185] Y. Chen, X. Peng, X. Fan, Q. Yu, G. Zhao, Y. Lin, J. Li, Z. Huang, *J. Solid State Electrochem.* **2019**, 23, 367.
- [186] L. Martin, H. Martinez, D. Poinot, B. Pecquenard, F. L. Cras, *J. Power Sources* **2014**, 248, 861.
- [187] J. Zhang, X. Yang, R. Wang, W. Dong, W. Lu, X. Wu, X. Wang, H. Li, L. Chen, *J. Phys. Chem. C* **2014**, 118, 20756.
- [188] G. Zhang, T. Xiong, L. He, M. Yan, K. Zhao, X. Xu, L. Mai, *J. Mater. Sci.* **2017**, 52, 3697.
- [189] Y. N. Zhou, J. Ma, E. Hu, X. Yu, L. Gu, K. W. Nam, L. Chen, Z. Wang, X. Q. Yang, *Nat. Commun.* **2014**, 5, 5381.
- [190] Y. Kim, S. Muhammad, H. Kim, Y. H. Cho, H. Kim, J. M. Kim, W. S. Yoon, *ChemSusChem* **2015**, 8, 2378.
- [191] L. Feng, Z. Chen, R. Chen, S. J. Dillon, *J. Power Sources* **2018**, 400, 198.
- [192] J. Sastre, X. Chen, A. Aribia, A. N. Tiwari, Y. E. Romanyuk, *ACS Appl. Mater. Interfaces* **2020**, 12, 36196.
- [193] Y. Lu, L. Yu, X. W. Lou, *Chem* **2018**, 4, 972.
- [194] K. J. Griffith, K. M. Wiaderek, G. Cibin, L. E. Marbella, C. P. Grey, *Nature* **2018**, 559, 556.
- [195] G. N. Zhu, Y. G. Wang, Y. Y. Xia, *Energy Environ. Sci.* **2012**, 5, 6652.
- [196] D. P. Abraham, E. M. Reynolds, E. Sammann, A. N. Jansen, D. W. Dees, *Electrochim. Acta* **2005**, 51, 502.
- [197] Y. B. He, M. Liu, Z. D. Huang, B. Zhang, Y. Yu, B. H. Li, F. Y. Kang, J. K. Kim, *J. Power Sources* **2013**, 239, 269.
- [198] R. Dedryvere, D. Foix, S. Franger, S. Patoux, L. Daniel, D. Gonbeau, *J. Phys. Chem. C* **2010**, 114, 10999.
- [199] M. S. Song, R. H. Kim, S. W. Baek, K. S. Lee, K. Park, A. Benayad, *J. Mater. Chem. A* **2014**, 2, 631.
- [200] S. Wang, K. Yang, F. Gao, D. Wang, C. Shen, *RSC Adv.* **2016**, 6, 77105.
- [201] W. K. Pang, V. K. Peterson, N. Sharma, J. J. Shiu, S. H. Wu, *Chem. Mater.* **2014**, 26, 2318.
- [202] M. G. Verde, L. Baggetto, N. Balke, G. M. Veith, J. K. Seo, Z. Wang, Y. S. Meng, *ACS Nano* **2016**, 10, 4312.
- [203] J. P. Pineda, C. Lee, B. Kim, K. Lee, *Microsc. Today* **2020**, 28, 48.
- [204] T. Stephenson, Z. Li, B. Olsen, D. Mitlin, *Energy Environ. Sci.* **2014**, 7, 209.
- [205] Z. Li, K. Jiang, F. Khan, A. Goswami, J. Liu, A. Passian, T. Thundat, *Sci. Adv.* **2019**, 5, eaav2820.
- [206] S. D. Lacey, J. Wan, A. W. Cresce, S. M. Russell, J. Dai, W. Bao, K. Xu, L. Hu, *Nano Lett.* **2015**, 15, 1018.
- [207] J. Wan, Y. Hao, Y. Shi, Y. X. Song, H. J. Yan, J. Zheng, R. Wen, L. J. Wan, *Nat. Commun.* **2019**, 10, 3265.
- [208] M. R. Lukatskaya, O. Mashtalir, C. E. Ren, Y. Dall'Agnese, P. Rozier, P. L. Taberna, M. Naguib, P. Simon, M. W. Barsoum, Y. Gogotsi, *Science* **2013**, 341, 1502.
- [209] J. Come, J. M. Black, M. R. Lukatskaya, M. Naguib, M. Beidaghi, A. J. Rondinone, S. V. Kalinin, D. J. Wesolowski, Y. Gogotsi, N. Balke, *Nano Energy* **2015**, 17, 27.
- [210] Z. Ali, T. Zhang, M. Asif, L. Zhao, Y. Yu, Y. Hou, *Mater. Today* **2020**, 35, 131.
- [211] M. Azhagurajan, T. Kajita, T. Itoh, Y. G. Kim, K. Itaya, *J. Am. Chem. Soc.* **2016**, 138, 3355.
- [212] J. Wan, W. Bao, Y. Liu, J. Dai, F. Shen, L. Zhou, X. Cai, D. Urban, Y. Li, K. Jungjohann, M. S. Fuhrer, L. Hu, *Adv. Energy Mater.* **2015**, 5, 1401742.
- [213] H. M. K. Sari, X. Li, *Adv. Energy Mater.* **2019**, 9, 1901597.
- [214] A. Manthiram, *Nat. Commun.* **2020**, 11, 1550.
- [215] R. Vidu, F. T. Quinlan, P. Stroeve, *Ind. Eng. Chem. Res.* **2002**, 41, 6546.
- [216] S. Ramdon, B. Bhushan, S. C. Nagpure, *J. Power Sources* **2014**, 249, 373.
- [217] D. E. Demirocak, B. Bhushan, *J. Colloid Interface Sci.* **2014**, 423, 151.
- [218] T. Doi, M. Inaba, H. Tsuchiya, S. K. Jeong, Y. Iriyama, T. Abe, Z. Ogumi, *J. Power Sources* **2008**, 180, 539.
- [219] S. Ramdon, B. Bhushan, *J. Power Sources* **2014**, 246, 219.
- [220] J. Wu, W. Cai, G. Shang, *Nanoscale Res. Lett.* **2016**, 11, 233.
- [221] R. Vidu, P. Stroeve, *Ind. Eng. Chem. Res.* **2004**, 43, 3314.
- [222] Z. Liu, Z. Bi, Y. Shang, Y. Liang, P. Yang, X. Li, C. Zhang, G. Shang, *Langmuir* **2020**, 36, 4689.
- [223] M. D. Radin, S. Hy, M. Sina, C. Fang, H. Liu, J. Vinckeviciute, M. Zhang, M. S. Whittingham, Y. S. Meng, A. V. Ven, *Adv. Energy Mater.* **2017**, 7, 1602888.
- [224] H. Sakai, Y. Taniguchi, K. Uosaki, T. Masuda, *J. Power Sources* **2019**, 413, 29.
- [225] X. Zhu, C. S. Ong, X. Xu, B. Hu, J. Shang, H. Yang, S. Katlakunta, Y. Liu, X. Chen, L. Pan, J. Ding, R. W. Li, *Sci. Rep.* **2013**, 3, 1084.
- [226] W. Lu, J. Zhang, J. Xu, X. Wu, L. Chen, *ACS Appl. Mater. Interfaces* **2017**, 9, 19313.
- [227] R. R. Liu, X. Deng, X. R. Liu, H. J. Yan, A. M. Cao, D. Wang, *Chem. Commun.* **2014**, 50, 15756.
- [228] Y. Xia, J. Zheng, C. Wang, M. Gu, *Nano Energy* **2018**, 49, 434.
- [229] H. J. Guo, H. X. Wang, Y. J. Guo, G. X. Liu, J. Wan, Y. X. Song, X. A. Yang, F. F. Jia, F. Y. Wang, Y. G. Guo, R. Wen, L. J. Wan, *J. Am. Chem. Soc.* **2020**, 142, 20752.
- [230] Y. Bi, J. Tao, Y. Wu, L. Li, Y. Xu, E. Hu, B. Wu, J. Hu, C. Wang, J. G. Zhang, Y. Qi, J. Xiao, *Science* **2020**, 370, 1313.
- [231] J. H. Kim, S. J. Kim, T. Yuk, J. Kim, C. S. Yoon, Y. K. Sun, *ACS Energy Lett.* **2018**, 3, 3002.
- [232] S. Y. Park, W. J. Baek, S. Y. Lee, S. Y. Lee, J. A. Seo, Y. S. Kang, M. Koh, S. H. Kim, *Nano Energy* **2018**, 49, 1.
- [233] M. Koltypin, V. Pol, A. Gedanken, D. Aurbach, *J. Electrochem. Soc.* **2007**, 154, A605.
- [234] J. Swiatowska-Mrowiecka, V. Maurice, L. Klein, P. Marcus, *Electrochem. Commun.* **2007**, 9, 2448.
- [235] B. Fleutot, H. Martinez, B. Pecquenard, J. B. Ledeuil, A. Levasseur, D. Gonbeau, *J. Power Sources* **2008**, 180, 836.
- [236] Y. S. Cohen, D. Aurbach, *Electrochem. Commun.* **2004**, 6, 536.
- [237] P. C. Tsai, B. Wen, M. Wolfman, M. J. Choe, M. S. Pan, L. Su, K. Thornton, J. Cabana, Y. M. Chiang, *Energy Environ. Sci.* **2018**, 11, 860.
- [238] S. M. Bak, Z. Shadike, R. Lin, X. Yu, X. Q. Yang, *NPG Asia Mater* **2018**, 10, 563.
- [239] T. M. M. Heenan, C. Tan, J. Hack, D. J. L. Brett, P. R. Shearing, *Mater. Today* **2019**, 31, 69.
- [240] T. M. M. Heenan, A. V. Llewellyn, A. S. Leach, M. D. R. Kok, C. Tan, R. Jervis, D. J. L. Brett, P. R. Shearing, *Adv. Sci.* **2020**, 7, 2000362.
- [241] T. M. M. Heenan, A. Wade, C. Tan, J. E. Parker, D. Matras, A. S. Leach, J. B. Robinson, A. Llewellyn, A. Dimitrijevic, R. Jervis, P. D. Quinn, D. J. L. Brett, P. R. Shearing, *Adv. Energy Mater.* **2020**, 10, 2002655.
- [242] S. R. Daemi, C. Tan, A. Vamvakeros, T. M. M. Heenan, D. P. Finegan, M. D. Michiel, A. M. Beale, J. Cookson, E. Petrucco, J. S. Weaving, S. Jacques, R. Jervis, D. J. L. Brett, P. R. Shearing, *Phys. Chem. Chem. Phys.* **2020**, 22, 17814.

- [243] A. K. C. Estandarte, J. Diao, A. V. Llewellyn, A. Jnawali, T. M. M. Heenan, S. R. Daemi, J. J. Bailey, S. Cipiccia, D. Batey, X. Shi, C. Rau, D. J. L. Brett, R. Jarvis, I. K. Robinson, P. R. Shearing, *ACS Nano* **2021**, *15*, 1321.
- [244] K. Marker, C. Xu, C. P. Grey, *J. Am. Chem. Soc.* **2020**, *142*, 17447.
- [245] K. Marker, P. J. Reeves, C. Xu, K. J. Griffith, C. P. Grey, *Chem. Mater.* **2019**, *31*, 2545.
- [246] C. Xu, K. Marker, J. Lee, A. Mahadevegowda, P. J. Reeves, S. J. Day, M. F. Groh, S. P. Emge, C. Ducati, B. L. Mehdi, C. C. Tang, C. P. Grey, *Nat. Mater.* **2021**, *20*, 84.
- [247] T. Liu, H. Hu, X. Ding, H. Yuan, C. Jin, J. Nai, Y. Liu, Y. Wang, Y. Wan, X. Tao, *Energy Storage Mater.* **2020**, *30*, 346.
- [248] M. Agostini, D. J. Lee, B. Scrosati, Y. K. Sun, J. Hassoun, *J. Power Sources* **2014**, *265*, 14.
- [249] S. Y. Lang, Y. Shi, Y. G. Guo, D. Wang, R. Wen, L. J. Wan, *Angew. Chem., Int. Ed.* **2016**, *55*, 15835.
- [250] S. Y. Lang, Y. Shi, Y. G. Guo, R. Wen, L. J. Wan, *Angew. Chem., Int. Ed.* **2017**, *56*, 14433.
- [251] R. Elazari, G. Salitra, Y. Talyosef, J. Grinblat, C. Scordilis-Kelley, A. Xiao, J. Affinito, D. Aurbach, *J. Electrochem. Soc.* **2010**, *157*, A1131.
- [252] K. Mahankali, N. K. Thangavel, L. M. R. Arava, *Nano Lett.* **2019**, *19*, 5229.
- [253] J. Tan, D. Liu, X. Xu, L. Mai, *Nanoscale* **2017**, *9*, 19001.
- [254] M. I. Nandasiri, L. E. Camacho-Forero, A. M. Schwarz, V. Shutthanandan, S. Thevuthasan, P. B. Balbuena, K. T. Mueller, V. Murugesan, *Chem. Mater.* **2017**, *29*, 4728.
- [255] M. Cuisinier, P. E. Cabelguen, S. Evers, G. He, M. Kolbeck, A. Garsuch, T. Bolin, M. Balasubramanian, L. F. Nazar, *J. Phys. Chem. Lett.* **2013**, *4*, 3227.
- [256] E. C. Miller, R. M. Kasse, K. N. Heath, B. R. Perdue, M. F. Toney, *J. Electrochem. Soc.* **2018**, *165*, A6043.
- [257] S. Walus, C. Barchasz, J. F. Colin, J. F. Martin, E. Elkaim, J. C. Lepretre, F. Alloin, *Chem. Commun.* **2013**, *49*, 7899.
- [258] J. Nelson, S. Misra, Y. Yang, A. Jackson, Y. Liu, H. Wang, H. Dai, J. C. Andrews, Y. Cui, M. F. Toney, *J. Am. Chem. Soc.* **2012**, *134*, 6337.
- [259] X. Yu, H. Pan, Y. Zhou, P. Northrup, J. Xiao, S. Bak, M. Liu, K. W. Nam, D. Qu, J. Liu, T. Wu, X. Q. Yang, *Adv. Energy Mater.* **2015**, *5*, 1500072.
- [260] Z. Ma, X. Yuan, L. Li, Z. F. Ma, D. P. Wilkinson, L. Zhang, J. Zhang, *Energy Environ. Sci.* **2015**, *8*, 2144.
- [261] A. Kumar, F. Ciucci, A. N. Morozovska, S. V. Kalinin, S. Jesse, *Nat. Chem.* **2011**, *3*, 707.
- [262] Y. Ansari, K. Virwani, S. Yahyazadeh, L. E. Thompson, E. Lofano, A. Fong, R. D. Miller, Y. H. La, *Adv. Energy Mater.* **2018**, *8*, 1802603.
- [263] R. Wen, M. Hong, H. R. Byon, *J. Am. Chem. Soc.* **2013**, *135*, 10870.
- [264] K. Virwani, Y. Ansari, K. Nguyen, F. J. A. Moreno-Ortiz, J. Kim, M. J. Giammona, H. C. Kim, Y. H. La, *Beilstein J. Nanotechnol.* **2019**, *10*, 930.
- [265] R. Wen, H. R. Byon, *Chem. Commun.* **2014**, *50*, 2628.
- [266] C. Liu, S. Ye, *J. Phys. Chem. C* **2016**, *120*, 25246.
- [267] Z. Z. Shen, C. Zhou, R. Wen, L. J. Wan, *J. Am. Chem. Soc.* **2020**, *142*, 16007.
- [268] M. Galinski, A. Lewandowski, I. Stepniak, *Electrochim. Acta* **2006**, *51*, 5567.
- [269] J. M. Black, M. B. Okatan, G. Feng, P. T. Cummings, S. V. Kalinin, N. Balke, *Nano Energy* **2015**, *15*, 737.
- [270] J. Zheng, M. Gu, H. Chen, P. Meduri, M. H. Engelhard, J. G. Zhang, J. Liu, J. Xiao, *J. Mater. Chem. A* **2013**, *1*, 8464.
- [271] X. Hu, C. Chen, J. Yan, B. Mao, *J. Power Sources* **2015**, *293*, 187.
- [272] J. S. Keist, C. A. Orme, P. K. Wright, J. W. Evans, *Electrochim. Acta* **2015**, *152*, 161.
- [273] J. M. Black, D. Walters, A. Labuda, G. Feng, P. C. Hillesheim, S. Dai, P. T. Cumming, S. V. Kalinin, R. Proksch, N. Balke, *Nano Lett.* **2013**, *13*, 5954.
- [274] A. Elbourne, S. McDonald, K. Voihovsky, F. Endres, G. G. Warr, R. Atkin, *ACS Nano* **2015**, *9*, 7608.
- [275] S. Zhou, K. S. Panse, M. H. Motevaselian, N. R. Aluru, Y. Zhang, *ACS Nano* **2020**, *14*, 17515.
- [276] S. Begic, H. Li, R. Atkin, A. F. Hollenkamp, P. C. Howlett, *Phys. Chem. Chem. Phys.* **2016**, *18*, 29337.
- [277] D. A. Rakov, F. Chen, S. A. Ferdousi, H. Li, T. Pathirana, A. N. Simonov, P. C. Howlett, R. Atkin, M. Forsyth, *Nat. Mater.* **2020**, *19*, 1096.
- [278] Y. Shi, H. Yan, R. Wen, L. Wan, *ACS Appl. Mater. Interfaces* **2017**, *9*, 22063.
- [279] X. B. Cheng, C. Z. Zhao, Y. X. Yao, H. Liu, Q. Zhang, *Chem* **2019**, *5*, 74.
- [280] Y. G. Lee, S. Fujiki, C. Jung, N. Suzuki, N. Yashiro, R. Omoda, D. S. Ko, T. Shiratsuchi, T. Sugimoto, S. Ryu, J. H. Ku, T. Watanabe, Y. Park, Y. Aihara, D. Im, I. T. Han, *Nat. Energy* **2020**, *5*, 299.
- [281] Y. X. Song, Y. Shi, J. Wan, B. Liu, L. J. Wan, R. Wen, *Adv. Energy Mater.* **2020**, *10*, 2000465.
- [282] Z. Zhang, R. G. Antonio, K. L. Choy, *J. Power Sources* **2019**, *435*, 226736.
- [283] Z. Zhang, A. R. Gonzalez, K. L. Choy, *ACS Appl. Energy Mater.* **2019**, *2*, 7438.
- [284] R. Garcia-Mendez, J. G. Smith, J. C. Neufeind, D. J. Siegel, J. Sakamoto, *Adv. Energy Mater.* **2020**, *10*, 2000335.
- [285] F. Han, A. S. Westover, J. Yue, X. Fan, F. Wang, M. Chi, D. N. Leonard, N. J. Dudney, H. Wang, C. Wang, *Nat. Energy* **2019**, *4*, 187.
- [286] J. Kasemchainan, S. Zekoll, D. S. Jolly, Z. Ning, G. O. Hartley, J. Marrow, P. G. Bruce, *Nat. Mater.* **2019**, *18*, 1105.
- [287] Q. Liu, D. Zhou, D. Shanmukaraj, P. Li, F. Kang, B. Li, M. Armand, G. Wang, *ACS Energy Lett.* **2020**, *5*, 1456.
- [288] M. Yan, J. Y. Liang, T. T. Zuo, Y. X. Yin, S. Xin, S. J. Tan, Y. G. Guo, L. J. Wan, *Adv. Funct. Mater.* **2020**, *30*, 1908047.
- [289] S. Kim, C. Jung, H. Kim, K. E. Thomas-Alyea, G. Yoon, B. Kim, M. E. Badding, Z. Song, J. Chang, J. Kim, D. Im, K. Kang, *Adv. Energy Mater.* **2020**, *10*, 1903993.
- [290] J. Wan, Y. X. Song, W. P. Chen, H. J. Guo, Y. Shi, Y. J. Guo, J. L. Shi, Y. G. Guo, F. F. Jia, F. Y. Wang, R. Wen, L. J. Wan, *J. Am. Chem. Soc.* **2020**, *143*, 839.
- [291] Z. Lu, Z. Yang, C. Li, K. Wang, J. Han, P. Tong, G. Li, B. S. Vishnugopi, P. P. Mukherjee, C. Yang, W. Li, *Adv. Energy Mater.* **2021**, *11*, 2003811.
- [292] S. R. Catarelli, D. Lonsdale, L. Cheng, J. Syzdek, M. Doeff, *Front. Energy Res.* **2016**, *4*, 14.
- [293] J. S. Kim, H. Kim, M. Badding, Z. Song, K. Kim, Y. Kim, D. J. Yun, D. Lee, J. Chang, S. Kim, D. Im, S. Park, S. H. Kim, S. Heo, *J. Mater. Chem. A* **2020**, *8*, 16892.
- [294] C. S. Jiang, N. Dunlap, Y. Li, H. Guthrey, P. Liu, S. H. Lee, M. M. Al-Jassim, *Adv. Energy Mater.* **2020**, *10*, 2000219.
- [295] J. Zhu, J. Feng, L. Lu, K. Zeng, *J. Power Sources* **2012**, *197*, 224.
- [296] J. Yue, M. Yan, Y. X. Yin, Y. G. Guo, *Adv. Funct. Mater.* **2018**, *28*, 1707533.
- [297] D. H. S. Tan, A. Banerjee, Z. Chen, Y. S. Meng, *Nat. Nanotechnol.* **2020**, *15*, 170.
- [298] L. Xu, S. Tang, Y. Cheng, K. Wang, J. Liang, C. Liu, Y. C. Cao, F. Wei, L. Mai, *Joule* **2018**, *2*, 1991.
- [299] S. Choi, M. Jeon, J. Ahn, W. D. Jung, S. M. Choi, J. S. Kim, J. Lim, Y. J. Jang, H. G. Jung, J. H. Lee, B. I. Sang, H. Kim, *ACS Appl. Mater. Interfaces* **2018**, *10*, 23740.
- [300] J. Z. Lee, T. A. Wynn, M. A. Schroeder, J. Alvarado, X. Wang, K. Xu, Y. S. Meng, *ACS Energy Lett.* **2019**, *4*, 489.
- [301] Z. Wang, D. Santhanagopalan, W. Zhang, F. Wang, H. L. Xin, K. He, J. Li, N. Dudney, Y. S. Meng, *Nano Lett.* **2016**, *16*, 3760.
- [302] E. Ventosa, P. Wilde, A. H. Zinn, M. Trautmann, A. Ludwig, W. Schuhmann, *Chem. Commun.* **2016**, *52*, 6825.

- [303] G. Zampardi, E. Ventosa, F. L. Mantia, W. Schuhmann, *Chem. Commun.* **2013**, 49, 9347.
- [304] X. Zeng, D. Liu, S. Wang, S. Liu, X. Cai, L. Zhang, R. Zhao, B. Li, F. Kang, *ACS Appl. Mater. Interfaces* **2020**, 12, 37047.
- [305] Z. T. Gossage, J. Hui, Y. Zeng, H. Flores-Zuleta, J. Rodriguez-Lopez, *Chem. Sci.* **2019**, 10, 10749.
- [306] A. L. Lipson, R. S. Ginder, M. C. Hersam, *Adv. Mater.* **2011**, 23, 5613.
- [307] Y. Takahashi, A. Kumatani, H. Munakata, H. Inomata, K. Ito, K. Ino, H. Shiku, P. R. Unwin, Y. E. Korchev, K. Kanamura, T. Matsue, *Nat. Commun.* **2014**, 5, 5450.
- [308] S. Yang, B. Yan, T. Li, J. Zhu, L. Lu, K. Zeng, *Phys. Chem. Chem. Phys.* **2015**, 17, 22235.
- [309] S. Guo, S. Jesse, S. Kalnaus, N. Balke, C. Daniel, S. V. Kalinin, *J. Electrochem. Soc.* **2011**, 158, A982.
- [310] N. Balke, S. Jesse, A. N. Morozovska, E. Eliseev, D. W. Chung, Y. Kim, L. Adamczyk, R. E. Garcia, N. Dudney, S. V. Kalinin, *Nanotechnol.* **2010**, 5, 749.
- [311] J. Zhu, L. Lu, K. Zeng, *ACS Nano* **2013**, 7, 1666.
- [312] S. C. Nagpure, B. Bhushan, S. S. Babu, *J. Power Sources* **2011**, 196, 1508.
- [313] X. Zhu, R. I. Revilla, A. Hubin, *J. Phys. Chem. C* **2018**, 122, 28556.
- [314] J. S. Harrison, D. A. Waldow, P. A. Cox, R. Giridharagopal, M. Adams, V. Richmond, S. Modahl, M. Longstaff, R. Zhuravlev, D. S. Ginger, *ACS Nano* **2019**, 13, 536.
- [315] P. Schwager, H. Bglter, I. Plettenberg, G. Wittstock, *Energy Technol.* **2016**, 4, 1472.
- [316] X. Chen, J. Lai, Y. Shen, Q. Chen, L. Chen, *Adv. Mater.* **2018**, 30, 1802490.
- [317] X. Liu, D. Wang, L. Wan, *Sci. Bull.* **2015**, 60, 839.
- [318] E. Ventosa, W. Schuhmann, *Phys. Chem. Chem. Phys.* **2015**, 17, 28441.
- [319] N. Ebejer, A. G. Güell, S. C. S. Lai, K. McKelvey, M. E. Snowden, P. R. Unwin, *Annu. Rev. Anal. Chem.* **2013**, 6, 329.
- [320] M. E. Snowden, A. G. Güell Stanley, C. S. Lai, K. McKelvey, N. Ebejer, M. A. O'Connell, A. W. Colburn, P. R. Unwin, *Anal. Chem.* **2012**, 84, 2483.
- [321] S. Kalinin, N. Balke, S. Jesse, A. Tselev, A. Kumar, T. M. Arruda, S. Guo, R. Proksch, *Mater. Today* **2011**, 14, 548.
- [322] N. Balke, S. Jesse, Y. Kim, L. Adamczyk, A. Tselev, I. N. Ivanov, N. J. Dudney, S. V. Kalinin, *Nano Lett.* **2010**, 10, 3420.
- [323] N. Schön, R. Schierholz, S. Jesse, S. Yu, R. A. Eichel, N. Balke, F. Hausen, *Small Methods* **2021**, 5, 2001279.
- [324] Q. Sun, L. He, F. Zheng, Z. Wang, S. J. A. Oh, J. Sun, K. Zhu, L. Lu, K. Zeng, *J. Power Sources* **2020**, 471, 228468.
- [325] S. Duan, H. Jin, J. Yu, E. N. Esfahani, B. Yang, J. Liu, Y. Ren, Y. Chen, L. Lu, X. Tian, S. Hou, J. Li, *Nano Energy* **2018**, 51, 19.
- [326] H. Masuda, K. Matsushita, D. Ito, D. Fujita, N. Ishida, *Commun. Chem.* **2019**, 2, 140.
- [327] A. Mascaro, Z. Wang, P. Hovington, Y. Miyahara, A. Paoella, V. Garipey, Z. Feng, T. Enright, C. Aiken, K. Zaghbi, K. H. Bevan, P. Grutter, *Nano Lett.* **2017**, 17, 4489.
- [328] H. Masuda, N. Ishida, Y. Ogata, D. Ito, D. Fujita, *Nanoscale* **2017**, 9, 893.
- [329] M. Pasta, D. Armstrong, Z. L. Brown, J. Bu, M. R. Castell, P. Chen, A. Cocks, S. A. Corr, E. J. Cussen, E. Darnbrough, V. Deshpande, C. Doerrer, M. S. Dyer, H. El-Shinawi, N. Fleck, P. Grant, G. L. Gregory, C. Grovenor, L. J. Hardwick, J. T. S. Irvine, H. J. Lee, G. Li, E. Liberti, I. McClelland, C. Monroe, P. D. Nellist, P. R. Shearing, E. Shoko, W. Song, D. S. Jolly, et al., *J. Phys. Energy* **2020**, 2, 032008.
- [330] Z. Liu, Z. Bi, Y. Shang, Y. Liang, P. Yang, X. Li, C. Zhang, G. Shang, *Rev. Sci. Instrum.* **2020**, 91, 103701.
- [331] O. D. Payton, L. Picco, T. B. Scott, *Int. Mater. Rev.* **2016**, 61, 473.
- [332] V. Stancovski, S. Badilescu, *J. Appl. Electrochem.* **2014**, 44, 23.
- [333] D. Alikin, B. Slautin, A. Abramov, D. Rosato, V. Shur, A. Tselev, A. Kholkin, *Materials* **2019**, 12, 1416.
- [334] Z. C. Zeng, S. C. Huang, D. Y. Wu, L. Y. Meng, M. H. Li, T. X. Huang, J. H. Zhong, X. Wang, Z. L. Yang, B. Ren, *J. Am. Chem. Soc.* **2015**, 137, 11928.
- [335] J. Nanda, G. Yang, T. Hou, D. N. Voylov, X. Li, R. E. Ruther, M. Naguib, K. Persson, G. M. Veith, A. P. Sokolov, *Joule* **2019**, 3, 2001.
- [336] A. Dazzi, C. B. Pater, *Chem. Rev.* **2017**, 117, 5146.
- [337] G. Zampardi, S. Klink, V. Kuznetsov, T. Erichsen, A. Maljusch, F. L. Mantia, W. Schuhmann, E. Ventosa, *ChemElectroChem* **2015**, 2, 1607.
- [338] T. S. Watkins, D. Sarbapalli, M. J. Coughlan, A. S. Danis, J. Zhang, L. Zhang, K. R. Zavadil, J. Rodriguez-Lopez, *J. Mater. Chem. A* **2020**, 8, 15734.
- [339] A. J. Bard, L. R. Faulkner, *Electrochemical Methods: Fundamentals and Applications*, Wiley, Hoboken, NJ **2001**.



Zhenyu Zhang is a research fellow funded by the Faraday Institution, working in the Electrochemical Innovation Lab at University College London. He obtained his Ph.D. from City University of Hong Kong in 2016. His current work involves the in situ analysis of degradation mechanisms of battery electrode and electrolyte materials. His research also covers the synthesis and characterization of nanomaterials, graphene, solid state electrolyte materials, and their energy conversion and storage applications.



Samia Said is a Ph.D. research student in the Electrochemical Innovations Lab at University College London. She studied Chemistry at the University of Manchester where she graduated from in 2017. In 2019 she then completed her M.Res. degree at Imperial College London in the multifunctional nanomaterials group. Her research interests are in the study of electrode/electrolyte interfaces of atomically thin 2D and 1D nanomaterials when applied as anode materials for sodium ion batteries, by using techniques such as in situ and operando electrochemical-atomic force microscopy.



Keenan Smith is a Ph.D. student in the Electrochemical Innovation Lab at University College London, having obtained his Chemistry M.Sc. at the University of Nottingham in 2018. His research utilizes advanced microscopy and scattering techniques to probe the nanoscale structure of novel materials, and their interfaces, in electrochemical energy devices to gain insight to their mechanism of operation.



Rhodri Jervis graduated from Balliol College, Oxford in Chemistry in 2008 and after a short time working for a medical research spinout in his home town of Swansea obtained his Ph.D. in fuel cell catalysis from University College London in 2015. After a post-doctoral research position in redox flow batteries he took up a position as lecturer in Chemical Engineering in UCL in 2018. He is currently the project lead for the Faraday Institution fast-start on Li ion battery degradation. His research interests focus on studying energy materials using a combination of electrochemical and X-ray techniques.



Christopher A. Howard is a professor of Materials Physics at UCL. His lab creates new materials that have desirable functional properties or that exhibit interesting emergent phenomena. Outputs range from nano-textured electrodes for batteries and fuel cell to new nanomaterials for solar cells to the discovery of exotic electronic groundstates. He studies these materials with a wide range of experimental techniques, pioneering the use of emerging methods from high-speed AFM to advanced neutron and X-ray scattering techniques at internationally leading facilities.



Paul R. Shearing is a Royal Academy of Engineering Chair in Emerging Technologies at University College London. His research interests cover a broad range of electrochemical engineering with a particular interest in the relationship between performance and microstructure for energy materials: an area in which he has published more than 250 papers (>6000 citations, $h = 43$). He is a pioneer of “4D Tomography” to study microstructure in electrochemical materials. He is a founding investigator of the Faraday Institution, and leads the STFC Global Challenge Network in Batteries and Electrochemical Energy Devices.



Dan J. L. Brett is a professor in Electrochemical Engineering in the Department of Chemical Engineering at UCL. He specializes in electrochemical engineering, including the modeling, testing, design, device fabrication, materials development, and techno-economic analysis. He has published over 350 peer reviewed papers in leading international journals ($h = 50$), and holds five patent families, based on which he is commercializing two spin-out companies. He is the UCL Director of the National Centre for Grid Scale Energy Storage and the UCL Director of the Centre for Doctoral Training in Fuel Cells and their Fuels.



Thomas S. Miller is a lecturer in Chemical Engineering at UCL and a member of the Electrochemical Innovation Lab (EIL), specializing in materials science and electrochemistry. In his work he has developed new and important nanomaterial processing methods and applied novel electrochemical techniques to projects in areas including energy storage/conversion, nanoparticle catalysis and sensing. In the field of batteries he is developing EC-AFM as a tool for the advanced characterization of both commercial and novel electrode materials. He is also creating and testing new electrode materials and designing diagnostic tools for on board fault finding, supported by the Faraday Institution.